NPS ARCHIVE
1962
CLARKE, L.

HEMISPHERIC SOLUTION OF THE OMEGA EQUATION INCLUDING TERRAIN AND SURFACE FRICTIONAL EFFECTS

LEO C. CLARKE
and
GEORGE E. LAWNICZAK, JR.

LIBRARY
U.S. NAVAL POSTGRADUATE SCHOOL
MONTEREY, CALIFORNIA

HEMISPHERIC SOLUTION OF THE OMEGA EQUATION INCLUDING TERRAIN AND SURFACE FRICTIONAL EFFECTS

* * * * *

Leo C. Clarke

and

George E. Lawniczak, Jr.

HEMISPHERIC SOLUTION OF THE OMEGA EQUATION

INCLUDING TERRAIN AND SURFACE FRICTIONAL EFFECTS

by

Leo C. Clarke
//
Commander, United States Naval Reserve

and

George E. Lawniczak, Jr.

Lieutenant, United States Navy

Submitted in partial fulfillment of
the requirements for the degree of

MASTER OF SCIENCE
IN
METEOROLOGY

United States Naval Postgraduate School
Monterey, California

1 9 6 2

NPS Archive
1962
Clarke, L

Thesis
C1216

LIBRARY
U.S. NAVAL POSTGRADUATE SCHOOL
MONTEREY, CALIFORNIA

HEMISPHERIC SOLUTION OF THE OMEGA EQUATION INCLUDING TERRAIN AND SURFACE FRICTIONAL EFFECTS

by

Leo C. Clarke

and

George E. Lawniczak, Jr.

This work is accepted as fulfilling
the thesis requirements for the degree of
MASTER OF SCIENCE
IN
METEOROLOGY
from the
United States Naval Postgraduate School

ABSTRACT

A quasi-geostrophic omega equation for large-scale vertical velocities in the atmosphere is solved at the earth's surface, 850 mb, 700 mb, 500 mb, and 300 mb for a grid of 1977 points per level covering the major portion of the Northern Hemisphere. The effects of terrain and surface frictional stress on the vertical velocity at the lower boundary are investigated in some detail and applied at the earth's surface. The three-dimensional integration of the resulting equations excludes areas "inside" the terrain. The mathematical model is programmed for the Control Data Corporation 1604 digital computer to utilize the operational output of machine-processed data and analyses produced by the Fleet Numerical Weather Facility (FNWF), Monterey, California. The program allows a wide variety of modes of operation and yields a solution for ω in five minutes.

An unusual weather situation in January, 1962 is investigated and the results, though tentative, show that the correlation between computed vertical velocities and the observed weather is excellent.

The writers wish to express their appreciation to Professor George J. Haltiner of the U. S. Naval Postgraduate School for his guidance, contributions and assistance in this investigation.

Appreciation is expressed for the aid and cooperation of personnel at FNWF, especially to Mr. Milton H. Reese, who designed and programmed the initial phases of the machine computations. Gratitude is expressed to Mrs. Lillian F. Paine for her patience in typing this thesis.

TABLE OF CONTENTS

Section	Title	Page
1.	Introduction	1
2.	Method of Solution	2
3.	The Lower Boundary Condition	11
4.	Omega at the Lower Boundary	16
5.	Some Features of the Computer Program	23
6.	Discussion of Results	26
7.	Vertical Velocity Computations for a Particular Synoptic Situation	27
	Appendix A (Extracts from hemispheric prints of omega and relative vorticity fields)	43
	Appendix B (Cross sections of omega fields plus temperature, relative vorticity and stability for 0000Z 22 January 1962)	105
	Appendix C (Hemispheric charts of D values and temperatures plus stability for 0000Z 22 January 1962)	117
	Appendix D (TIROS observations and corresponding omega fields)	158
	Bibliography	171
	Transparent Overlay	173

LIST OF ILLUSTRATIONS

Figure		Page
1.	Definition of pressure finite differences	6
2.	Extrapolation scheme for D_T	12
3.	Internal boundary relationships	15
4.	Orientation of surface stress	18
5.	Extrapolation scheme for $(D_T)_p$	21
6.	Omega at lower boundary	27
7.	Omega at 850 mb with $C_J = 0$	28
8.	Omega at 700 mb with $C_J = 0$	29
9.	Omega at 500 mb with $C_J = 0$	30
10.	Omega at 300 mb with $C_J = 0$	31
11.	Omega at lower boundary	32
12.	Omega at 850 mb with terrain "in;" omega at 850 mb with terrain "out"	33
13.	Omega at 700 mb with terrain "in;" omega at 700 mb with terrain "out"	34
14.	Omega at 500 mb with terrain "in;" omega at 500 mb with terrain "out"	35
15.	Omega at 300 mb with terrain "in;" omega at 300 mb with terrain "out"	36

LIST OF SYMBOLS

ω	The vertical velocity of air in pressure coordinates
$()_{LO}$	A subscript that specifies the value of a parameter at the lower boundary
ω_F	The frictionally induced ω at the top of the friction layer
θ	The potential temperature
$()_K$	The vertical component of the mesh ($K = 1, 2, \cdots$); K increases with increasing pressure
R	The universal gas constant
f	The coriolis parameter, $2\Omega \sin\phi$, where Ω is angular speed of earth and ϕ is the latitude
f_o	The value of the coriolis parameter at the pole
f_m	The mean value of the coriolis parameter
g	The upward component of the apparent gravitational acceleration
ζ	The relative vorticity
η	The absolute vorticity
∇^2	The horizontal Laplacian operator on a constant-pressure surface
∇	The del operator on a constant-pressure surface
$J(A,B)$	The horizontal Jacobian operator

$$J(A,B) = \frac{\partial A}{\partial x}\frac{\partial B}{\partial y} - \frac{\partial B}{\partial x}\frac{\partial A}{\partial y}$$

z	The height in centimeters
$()_T$	A subscript that specifies the value of a parameter at the terrain
c_p	The specific heat of dry air

S The specific temperature anomaly

$$S = \frac{\partial D}{\partial Z_P} = \frac{T - T_P}{T_P}$$

$()_{UL}$ Used as a subscript to specify difference of a parameter between two heights

Z_P The pressure altitude in centimeters

d The mesh dimension, 381 km

D The altimeter correction, $D = Z - Z_P$

τ The surface frictional stress

m The map factor for a polar stereographic map projection true at 60N

$()_L, ()_U$ A subscript that specifies the value of a parameter at a lower (L)/upper (U) height

$\hat{()}$ A caret specifies that the quantity has been scaled into a fractional quantity

σ The static stability, $\sigma = -\frac{T}{\theta}\frac{\partial \theta}{\partial p}$

p The atmospheric pressure in millibars

$\nabla, \nabla^2, \Delta, \mathfrak{F}$ Finite difference operators

1. Introduction

The value of vertical velocities in the atmosphere for understanding the basic weather phenomena associated with the large-scale features is gradually becoming more fully appreciated by synoptic forecasters [1]. The purpose of this investigation is to provide a means of computing these vertical velocity fields from routine weather charts and to examine the structure of these fields. Among the various methods for such determinations, the omega equation, derivable from the vorticity equation and the first law of thermodynamics, appears to afford the best means of computing large-scale vertical velocities from synoptic meteorological observations. Thus, the computer program developed for this omega equation is adaptable to operational use in a numerical forecasting center as well as for basic research.

The data used in this program are produced by the Fleet Numerical Weather Facility (FNWF), Monterey, California, essentially as follows [2]:

(a) Northern Hemisphere weather data are processed automatically by digital computer to yield reliable listings of surface and upper-air data.

(b) A Northern Hemisphere surface map is analyzed by digital computer and 1000-mb height and temperature charts are produced.

(c) The 850-mb, 700-mb, 500-mb and 300-mb height and temperature charts are then constructed with hydrostatic consistency by building upward from the 1000-mb level. Winds and off-time reports are also included.

(d) These surface and upper-air charts cover the entire Northern Hemisphere to the equator, and are produced at 0000 GCT and 1200 GCT daily. Further details are available at the Fleet Numerical Weather Facility.

2. Method of Solution

On the basis of the available data described above, it was decided to arrange the computational form of the omega equation so that only the data at a given constant-pressure level would be needed to calculate the parameters required in the iterative scheme for that level. This necessitated the use of unequally spaced pressure intervals in computing vertical derivatives, but gave the model some flexibility if additional levels became available or were changed.

The omega equation is derived from the vorticity equation (1), and the thermal equation (2) for adiabatic conditions by eliminating the local time derivatives jointly between the two equations.

$$\frac{g}{f}\nabla^2\frac{\partial z}{\partial t} + V\cdot\nabla\eta + \omega\frac{\partial \eta}{\partial p} = \eta\frac{\partial \omega}{\partial p} + \frac{\partial \omega}{\partial y}\frac{\partial u}{\partial p} - \frac{\partial \omega}{\partial x}\frac{\partial v}{\partial p}, \qquad (1)$$

$$\frac{\partial T}{\partial t} + V\cdot\nabla T - \omega\sigma = 0 \quad ; \quad \sigma = -\frac{T}{\theta}\frac{\partial \theta}{\partial p}, \qquad (2)$$

where the various symbols are defined in Table of Symbols, page v. The geostrophic approximation for vorticity has been made in the first term of equation (1). Operating on (1) with $\left(\frac{\partial}{\partial p}\right)$ and on (2) with $\left(-\nabla^2\right)$ and adding results in a form of the omega equation

$$\nabla^2(\sigma\omega) + \frac{pf\eta}{R}\frac{\partial^2\omega}{\partial p^2} - \nabla^2(V\cdot\nabla T) - \frac{pf}{R}\frac{\partial}{\partial p}(V\cdot\nabla\eta) - \frac{pf\omega}{R}\frac{\partial^2\eta}{\partial p^2} + \frac{pf}{R}\frac{\partial}{\partial p}\left(\frac{\partial \omega}{\partial y}\frac{\partial u}{\partial p} - \frac{\partial \omega}{\partial x}\frac{\partial v}{\partial p}\right) = 0 \; . \qquad (3)$$

The terms involving the vertical advection of vorticity and the twisting terms are usually of opposite sign and, moreover, small in comparison with the others remaining, and will be neglected as a first approximation. Of the terms which arise from the horizontal derivatives of σ,

$$\nabla^2(\sigma\omega) = \sigma\nabla^2\omega + \omega\nabla^2\sigma + 2\nabla\sigma\cdot\nabla\omega \quad , \tag{4}$$

the last two on the right are also considered to be small in comparison with the first and will be neglected. The neglected terms may be incorporated along the lines used in Stuart [3], to afford a solution to the more complete equation (3). It is to be noted that σ will be allowed to vary in the horizontal as well as with pressure in this scheme. To evaluate partially the effect of the variable σ, the computer program has been designed to utilize alternately horizontal and vertical means of the static stability as well.

Neglecting the last two terms in (4) and substituting in (3) gives the reduced omega equation (5)

$$\sigma\nabla^2\omega + \frac{pf_m^2}{R}\frac{\partial^2\omega}{\partial p^2} - \nabla^2(V\cdot\nabla T) - \frac{pf}{R}\frac{\partial}{\partial p}(V\cdot\nabla\eta) = 0 \tag{5}$$

where, in the second term, $f\eta$ has been replaced by f_m^2 to meet certain consistency requirements as described in [4] and [5]. Again, to evaluate the effect of this term, the computer program has both versions $f\eta$ and f_m^2 incorporated.

The third and fourth terms of (5) can be expanded using the geostrophic vorticity, $\zeta = \frac{g}{f}\nabla^2 Z$,

the hydrostatic equation, and the equation of state:

$$\left[\nabla^2(V\cdot\nabla T) - \frac{pf}{R}\frac{\partial}{\partial p}(V\cdot\nabla\eta)\right] =$$

$$\frac{g}{f}\left[-\nabla^2 J(Z,T) - \frac{f}{g}J(T,\eta) + J(Z,\nabla^2 T)\right].$$

Substituting this expression into (5) and rearranging gives the computational form of the reduced omega equation:

$$\nabla^2\omega + \frac{pf_m^2}{\sigma R}\frac{\partial^2\omega}{\partial p^2} = \frac{g}{f}\left[\nabla^2 J(Z,T) - J(Z,\nabla^2 T) - \frac{f}{g}J(T,\eta)\right] \quad (6)$$

The basic parameters involved above are Z and T. At a given level, the right side of (6) can be calculated from data at that level only. The last term on the right in (6) is generally considered to be of major importance and is used in the approximation made by Wiin-Nielsen [6].

The grid used is the Fleet Numerical Weather Facility Northern Hemisphere octagon of 1977 points centered on the pole and extending to about latitude 10N.

The omega equation (6) is to be solved at the four levels of 850 mb, 700 mb, 500 mb and 300 mb, with the lower boundary being the surface of the earth. The upper boundary is 100 mb where it is assumed that $\omega \equiv 0$, and the lateral boundaries are near 10N where it is also assumed that $\omega \equiv 0$.

To solve (6) numerically, the following finite-difference approximations, based on the adjoining five-point array, were used.

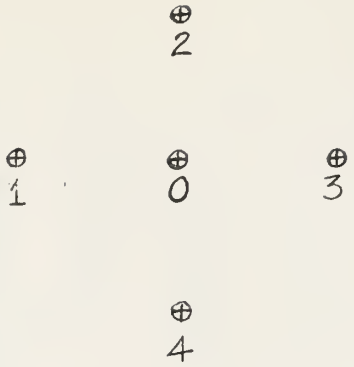

For arbitrary quantities A and B;

$$\Delta_x = A_3 - A_1 \ , \quad \Delta_y A = A_2 - A_4 \ , \quad \Delta_R A = \left[(\Delta_x A)^2 \ \ (\Delta_y A)^2 \right]^{\frac{1}{2}} ,$$

$$\Delta_x^2 A = A_3 + A_1 - 2A_0 \ , \quad \Delta_y^2 A = A_2 + A_4 - 2A_0 \ , \tag{7}$$

$$\nabla^2 A = \Delta_x^2 A + \Delta_y^2 A \ , \quad \nabla^2 A = \frac{m^2}{d^2} \nabla^2 A \ ,$$

$$\overline{J}(A,B) = (\Delta_x A)\cdot(\Delta_y B) - (\Delta_y A)\cdot(\Delta_x B) \ , \quad J(A,B) = \frac{m^2}{4d^2} \overline{J}(A,B) .$$

The portion of the term involving $P \frac{\partial^2 \omega}{\partial p^2}$ is approximated [4] by a finite-difference analog for unequal intervals

$$P \frac{\partial^2 \omega_K}{\partial p^2} \doteq \frac{P}{\Delta_U P} \cdot \frac{2 \Delta_K^2 \omega}{\Delta_K P} \tag{8}$$

where $$\Delta_K^2 \omega = \omega_{K-1} - \frac{\Delta_K P}{\Delta_L P} \omega_K + \frac{\Delta_U P}{\Delta_L P} \omega_{K+1}$$

and $\Delta_U P$, $\Delta_L P$ and $\Delta_K P$ are defined in figure 1.

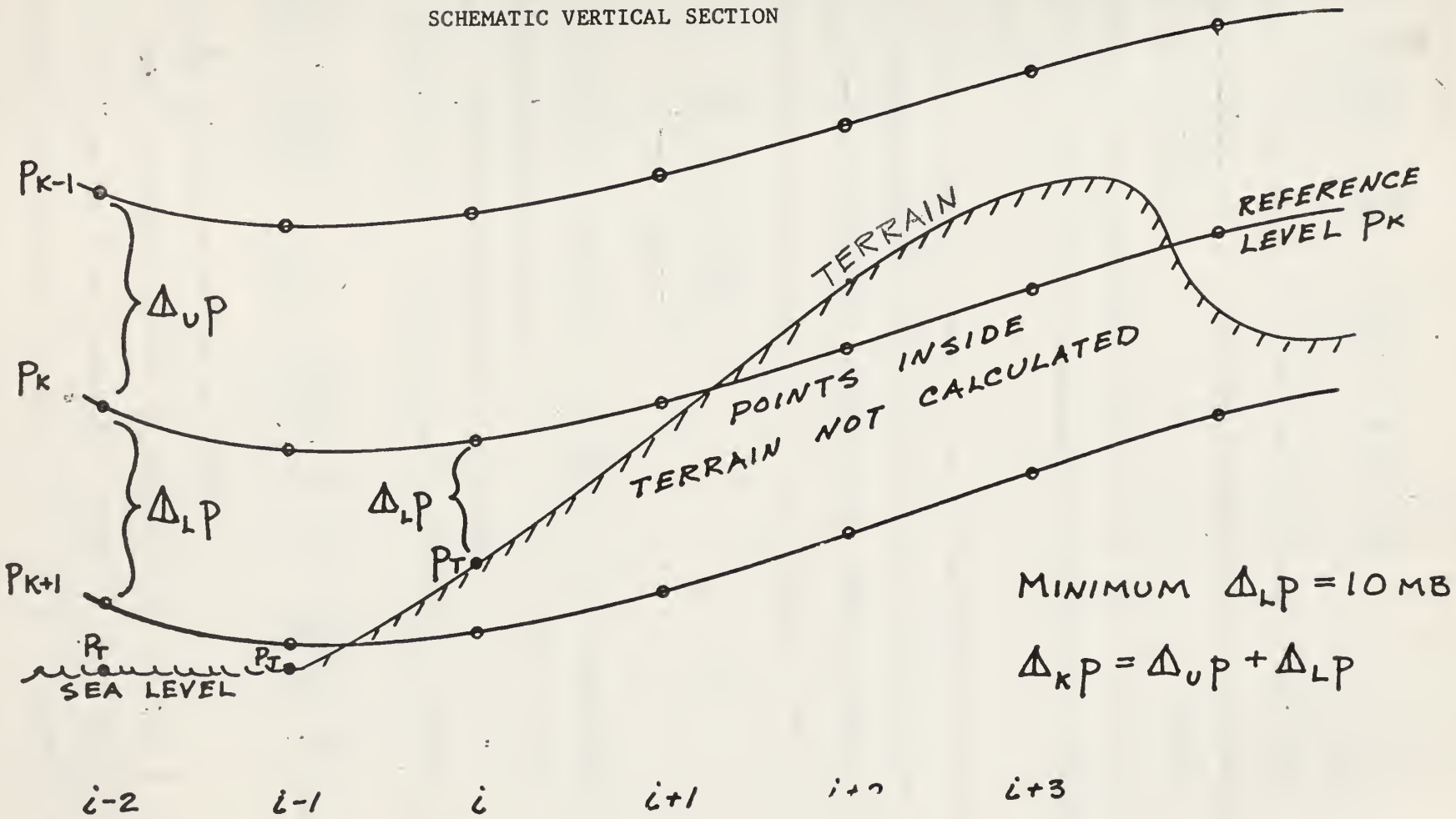

Figure 1. Definition of pressure finite differences.

The static stability

$$\sigma = -\frac{T}{\theta}\frac{\partial \theta}{\partial p} = \frac{RT}{pc_p} - \frac{\partial T}{\partial p} = \gamma_{p,D} - \gamma_p \qquad (9)$$

is equal to the difference between the dry adiabatic lapse rate $\gamma_{p,D} = RT/pc_p$ in pressure coordinates and the observed lapse rate $\gamma_p = \partial T/\partial p$. This form of the static stability parameter corresponds to that suggested by Gates [7] as "one of the more useful in modelling the large-scale disturbances in a troposphere of constant stability".

Since it is evident that the value of σ may approach zero or be negative, the magnitude of σ was controlled so that the second term of (6) remained positive and within certain bounds. This was done by requiring that the lapse rate not exceed 7/8 of the dry adiabatic lapse rate, namely,

$$\gamma_p \leq 7/8 \cdot \gamma_{p,D} \qquad \text{or}$$

$$\sigma \geq \gamma_{p,D} \cdot 2^{-3}. \qquad (9A)$$

Comparison of the true σ with $\gamma_{p,D} \cdot 2^{-3}$ for a few synoptic cases has shown that this limiting criterion is very rarely, if ever, required when the input data are vertically consistent.

The second term of is approximated by the finite difference analog [8]

$$\left(\frac{\partial T}{\partial p}\right)_K \doteq \frac{\Delta_p T_K}{\Delta_U p} = \frac{1}{\Delta_K p}\left[\frac{\Delta_U p}{\Delta_L p} \cdot \Delta_L T_K + \frac{\Delta_L p}{\Delta_U p} \cdot \Delta_U T_K\right] \qquad (10)$$

where Δ_L and Δ_U are defined in figure 1.

Sigma is expressed in units of degrees Kelvin per mb. In order to calculate sigma at 300 mb, temperature values at 100 mb are required. These data are not presently available from the Fleet Numerical Weather

Facility on a routine basis, and hence temperature values at 100 mb were approximated by either of the following schemes:

(a) The temperature at 100 mb was set equal to the 300-mb temperature. This approximates mid-latitude conditions and implies that a "tropopause" exists somewhere between the 300-mb and 100-mb levels, the specific pressure depending on the fitted parabola.

(b) A mean 100 mb temperature field is used based on a climatic summary. Since the synoptic case chosen for study was in January 1962, 5-year mean 100-mb temperatures for January (1949-1953) were used.

It is realized that neither of the above schemes is entirely satisfactory; however, the computer program is so arranged that synoptic analyses of 100-mb temperatures can be used when available on an operational basis.

In order to utilize established numerical sub-routines available at the FNWF as well as to minimize computational time, fixed-point fractional arithmetic was used exclusively in the computer program. Moreover, all parameters had to be scaled to have magnitudes less than one. The following standard FNWF scaling conventions were used:

$$
\begin{aligned}
&\omega = \hat{\omega} \cdot 2^{n} \ (\text{mb} \cdot \text{sec}^{-1}) && n = 8 \text{ at present} \\
&f = \hat{f} \cdot 2^{-9} \ (\text{sec}^{-1}) && \eta = \hat{\eta} \cdot 2^{-9} \ (\text{sec}^{-1}) \\
&D = \hat{D} \cdot 2^{17} \ (\text{cm}) && Z = \hat{Z} \cdot 2^{20} \ (\text{cm}) \\
&p = \hat{p} \cdot 2^{11} \ (\text{mb}) && \sigma = \hat{\sigma} \cdot 2^{3} \ (^{\circ}\text{K} \cdot \text{mb}^{-1}) \\
&m = \hat{m} \cdot 2^{1} && T = \hat{T} \cdot 2^{9} \ (^{\circ}\text{K or } ^{\circ}\text{C}) \ .
\end{aligned}
\tag{11}
$$

Substituting (7), (8), (9), (10), and (11) into (6) gives the

scaled difference equation that was programmed for the digital computer:

$$\nabla^2\hat{\omega}_K - \hat{B}_K \cdot 2^{12} \cdot \hat{\omega}_K = \frac{2^{-n} \cdot b \cdot \hat{m}^2}{\hat{\sigma}_K \cdot \sin\phi}\left[\nabla^2 J(\hat{D}_K, \hat{T}_K) - J(\hat{D}_K, \nabla^2 \hat{T}_K)\right.$$

$$\left. - \frac{\hat{c} \cdot \sin\phi}{\hat{m}^2} J(\hat{T}_K, \hat{\eta}_K)\right] - \hat{B}_K \cdot 2^{12}\left[\frac{\Delta_L \hat{p}}{\Delta_K \hat{p}} \cdot \hat{\omega}_{K-1} + \frac{\Delta_U \hat{p}}{\Delta_K \hat{p}} \cdot \hat{\omega}_{K+1}\right] \quad (12)$$

where $$B_K = \hat{B}_K \cdot 2^{12} = 2^{-12}\left[2^{-24} \frac{f_m^2 d^2}{R} \cdot \frac{\hat{p}_K}{\Delta_U \hat{p}} \cdot \frac{\sin\phi}{\Delta_L \hat{p} \cdot \hat{m}^2 \cdot \hat{\sigma}_K}\right].$$

Letting $C_J \equiv$ First term on right in (12),

$C_{\hat{\omega}} \equiv$ Second term on right in (12),

equation (12) becomes

$$\nabla^2\hat{\omega}_K - B_K \cdot \hat{\omega}_K = C_J - C_{\hat{\omega}} \equiv C_K, \quad K = 1, 2 \cdots \quad (13)$$

These equations were solved by an accelerated Liebmann relaxation iterative scheme where the $(v+1)$ iterate at the point (i, j) is given by

$$\hat{\omega}_K^{v+1} = \hat{\omega}_K^v + \frac{\lambda \cdot R^v}{4 + B_K} \quad (14)$$

Here the residual R at each step is:

$$R^v = \nabla^2\hat{\omega}_K^v - B_K \cdot \hat{\omega}_K^v - C_J + C_{\hat{\omega}^v} \quad (15)$$

The four pressure levels were successively scanned beginning at 850 mb and ending with the 300-mb level, this constituting one SCAN count

of 4(1977)= 7908 points in the 3-dimensional mesh.

Considering (13) as a system of Helmholtz equations, certain conditions regarding the coefficients must be fulfilled for convergence ('Arnason [9]) as follows.

(a) $B_K > 0$ (16)

(b) The sum of the coefficients of ω_{K-1} and ω_{K+1} in $C\hat{\omega}$ in (13) must be less than or equal to one, including round-off errors

$$B_K \left[\frac{\Delta_L \hat{P}}{\Delta_K \hat{P}} + \frac{\Delta_U \hat{P}}{\Delta_K \hat{P}} \right] \leq B_K \quad . \tag{17}$$

The first requirement (16) is easily met since $\sigma_K > 0$ (see (9A)). The second requirement is sensitive because of the great range of the coefficient B_K, which can vary from a very small positive value (arbitrarily set to 2^{-46}) to values of the order of 2000. Both of these requirements are incorporated into the program.

The convergence criterion ϵ is defined as

$$\omega_K^{\nu+1} - \omega_K^{\nu} < \epsilon$$

for all points of the mesh. The ϵ is chosen so that no meteorologically significant changes will occur in the omegas if iteration were continued. The smallest value of interest was taken as 10^{-4} mb sec^{-1} which is approximately equal to 0.1 cm sec^{-1} at 850 mb.

A number of different values of ϵ, ranging from 10^{-4} to (1/6400) 10^{-4} mb sec^{-1}, were tried to determine an optimum ϵ. The final operational value adopted was $\epsilon_{25} = \frac{1}{25} \cdot 10^{-4}$ mb sec^{-1} With this criterion, ϵ_{25}, convergence is reached, with the synoptic cases studied, in 14 to 15 SCANS as defined previously. For comparison purposes, convergence for $\epsilon_{100} = \frac{1}{100} \cdot 10^{-4}$ mb sec^{-1} is obtained in about 26 SCANS.

The over-relaxation coefficient λ used was determined experimentally by finding that λ for which convergence was reached in the least number of SCANS for a given ϵ . This optimum λ is very sharply defined and was found to be 1.414. A λ differing from this value by roughly 10% increased the SCAN count by about 25%, and a change in value of only 0.1% changed the SCAN count by one.

3. The Lower Boundary Condition

The lower boundary condition was of special interest in devising this model [10]. In most previous studies, the given or calculated lower boundary values of omega were arbitrarily assigned to the lowest constant-pressure level in the model, usually 1000 mb, and then the family of equations was integrated with no regard to the presence or absence of mountainous features. The intersection of any pressure surface with the terrain constitutes an internal boundary within the mesh and is treated as such in this model. It is noted that, in order to find the intersection of the terrain and a given pressure level, the pressure at the terrain P_T must be known.

The input data at the various pressure levels (K) consist of D_K values and temperature T_K in degrees C. The definition of D is

$$D = Z - Z_P \quad .$$

The D_T value at the height of the terrain Z_T is interpolated from the input data D_K by the principles of altimetry [11].

SCHEMATIC VERTICAL SECTION

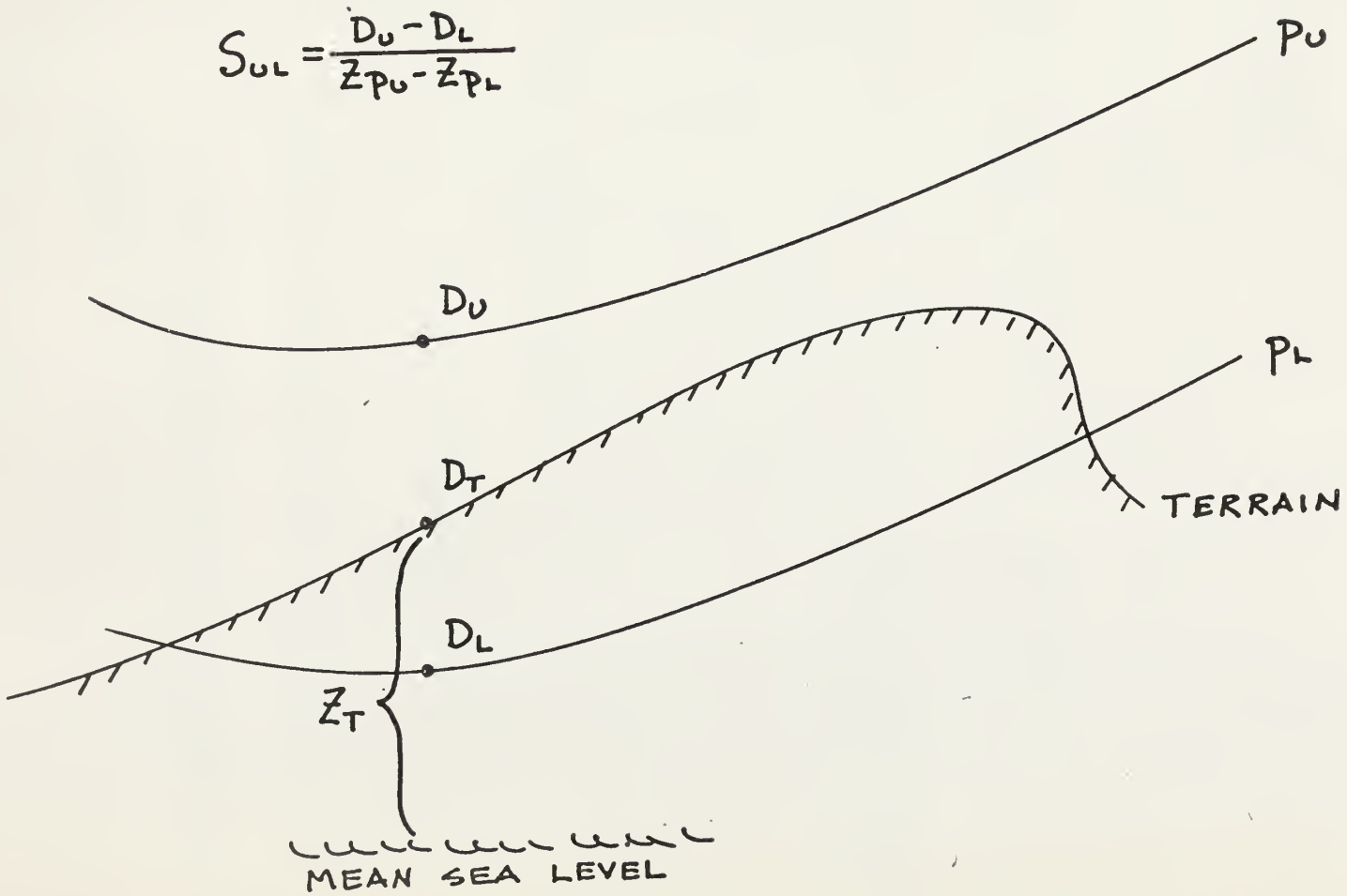

Figure 2. Extrapolation scheme for D_T

Let

$$\Delta_{UL} D \equiv D_U - D_L$$

$$\Delta_{UL} Z_P \equiv Z_{P_U} - Z_{P_L} \tag{18}$$

$$\Delta_{UT} Z_P \equiv Z_{P_U} - Z_{P_T}$$

$$\Delta_{UT} D \equiv D_U - D_T \quad \text{or} \quad D_T = D_U - \Delta_{UT} D \ .$$

To find $\Delta_{UT} D$, the specific temperature anomaly $S_{UL} = \Delta_{UL} D / \Delta_{UL} Z_P$ is calculated. This S_{UL} value is the mean for the column P_U to P_L. Applying it to the portion from P_U to P_T

$$\Delta_{UT} D = S_{UL} \cdot \Delta_{UT} Z_P \ .$$

Substituting in (18) gives

$$D_T = \frac{D_U - S_{UL}(Z_{P_U} - Z_T)}{1 + S_{UL}} \ . \tag{19}$$

Having interpolated D_T, the pressure altitude is then

$$Z_{P_T} = Z_T - D_T \ ,$$

and P_T can be obtained from Z_{P_T} since there is a one-to-one correspondence of values.

For the last step, an interpolating polynomial is developed that gives the terrain pressure with accuracy within one millibar.

The polynomial is

$$P_T = y(a + by^2) + u(c + du^2) \ , \tag{20}$$

where $a = 724.64$ $c = 597.37$
$b = 3.5562$ $d = 3.1272$

$$y = 1 - u$$

$$u = \frac{Z_{P_T} - 2.7 \cdot 10^5}{1.5 \cdot 10^5} .$$

The scaled polynomial is then

$$\hat{P}_T = 2^5 \left[\hat{y} \left(\hat{a} + \hat{b} \hat{y}^2 \right) + \hat{u} \left(\hat{c} + \hat{d} \hat{u}^2 \right) \right] ,$$

where $\hat{a} = 4.4229.10^{-2}$
$\hat{b} = 3.4729.10^{-3}$
$\hat{c} = 3.6461.10^{-2}$
$\hat{d} = 3.0539.10^{-3}$

$$u = \hat{u} \cdot 2^2$$

$$y = \hat{y} \cdot 2^2$$

$$\hat{u} = \frac{\hat{Z}_{P_T} - 0.25749}{0.57220}$$

$$y = 2^{-2} - \hat{u} .$$

The pressure at the terrain is calculated on a synoptic basis and is used in devising a marker field which controls the iterative scheme so that all points of the mesh which "lie" within the terrain are not relaxed and constitute an internal boundary. At the surface of the terrain a value of ω_{LO} is computed as described later. This ω_{LO} value is assigned to the same grid point at all greater pressure levels, i.e., those within the terrain. This substitution is illustrated schematically in figure 3. Note that under this scheme, the Laplacian of ω at (i) involves the uses of $(\omega_{LO})_{i+1}$, which generally more closely approximates the value of ω_A than if zero were used.

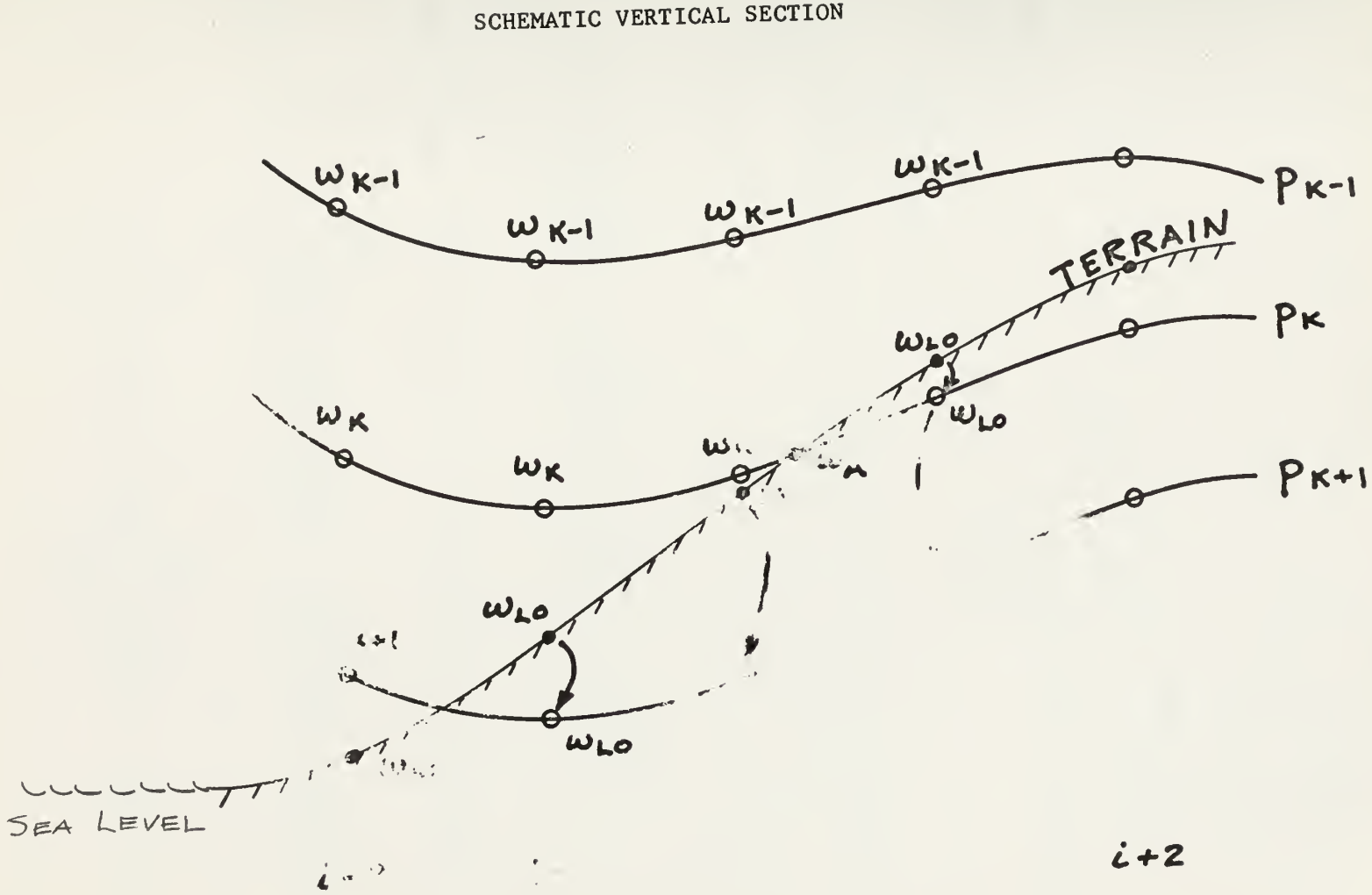

Figure 3. Internal boundary relationships.

4. Omega at the Lower Boundary

The pressure at the terrain p_T is also used to calculate the omega at the lower boundary, ω_{LO}. The combined effect of the frictionally-induced vertical velocity and the vertical velocity due to the slope of terrain will be calculated for the volume of air bounded by the surface of the earth at pressure p_T and at the top by a pressure p_{LO} where the surface frictional stress is assumed to vanish. The net inflow or convergence into this volume results in a vertical velocity ω_{LO} through the upper boundary. If the equation of continuity

$$-\frac{\partial \omega}{\partial p} = \nabla \cdot \mathbb{V} \tag{21}$$

is integrated through the friction layer, $p_T - p_{LO}$, utilizing the wind $\mathbb{V}$,

$$\mathbb{V} = -\frac{1}{f}\left[\frac{\partial \Phi}{\partial y} + g\frac{\partial \hat{\tau}_y}{\partial p}\right]\hat{i} + \frac{1}{f}\left[\frac{\partial \Phi}{\partial x} + g\frac{\partial \hat{\tau}_x}{\partial p}\right]\hat{j} \ , \tag{22}$$

where $\hat{\tau}_x$ and $\hat{\tau}_y$ are components of the stress, there results

$$\omega_{LO} - \omega_T = \int_{p_T}^{p_{LO}} \left\{ \frac{\partial}{\partial x}\left[\frac{1}{f}\frac{\partial \Phi}{\partial y} + g\frac{\partial \hat{\tau}_y}{\partial p}\right] - \frac{\partial}{\partial y}\left[\frac{1}{f}\frac{\partial \Phi}{\partial x} + g\frac{\partial \hat{\tau}_x}{\partial p}\right] \right\} dp$$

$$= \frac{1}{f}\int_{p_T}^{p_{LO}} (\mathbb{V}_g \cdot \nabla f)\, dp + \frac{g}{f}\int_{p_T}^{p_{LO}} \frac{\partial}{\partial p}\left[\frac{\partial \hat{\tau}_y}{\partial x} - \frac{\partial \hat{\tau}_x}{\partial y}\right] dp$$

$$= \frac{1}{f}\int_{P_T}^{P_{LO}} \beta v \, dp + \frac{g}{f}\left[\frac{\partial \tau_y}{\partial x} - \frac{\partial \tau_x}{\partial y}\right]_{P_{LO}} - \frac{g}{f}\left[\frac{\partial \tau_y}{\partial x} - \frac{\partial \tau_x}{\partial y}\right]_{P_T}$$

$$= -\frac{\beta}{f}\bar{v}_g\left(P_T - P_{LO}\right) + \frac{g}{f}\left[\frac{\partial \tau_{ox}}{\partial y} - \frac{\partial \tau_{oy}}{\partial x}\right], \qquad (23)$$

where τ_o is surface stress at P_T

and $\tau_x = \tau_y = 0$ at P_{LO}.

The first term on right in (23) is usually small in comparison with the other terms and is neglected. Setting $\omega_{LO} - \omega_T \equiv \omega_F$, the frictionally induced vertical velocity (23) may be written as

$$\omega_F = \frac{g}{f}\left[\frac{\partial \tau_{ox}}{\partial y} - \frac{\partial \tau_{oy}}{\partial x}\right] . \qquad (24)$$

If it is assumed (Lettau [12]) that the surface stress is opposite the direction of the wind, V_T , making an angle α with the isobars, (see figure 4), then

$$\tau_{ox} = \tau_o \cos\alpha \quad , \quad \tau_{oy} = \tau_o \sin\alpha \ .$$

The surface stress is further assumed to be proportional to the square of the wind at the top of friction layer in the manner of Lettau [11] and Cressman [10], i.e., $\tau_o = C_D \rho_{LO} V_{LO}^2$

and $$\tau_{ox} = C_D \rho_{LO} u_{LO} V_{LO} \quad , \quad \tau_{oy} = C_D \rho_{LO} v_{LO} V_{LO} \ . \qquad (25)$$

ON CONSTANT PRESSURE SURFACE

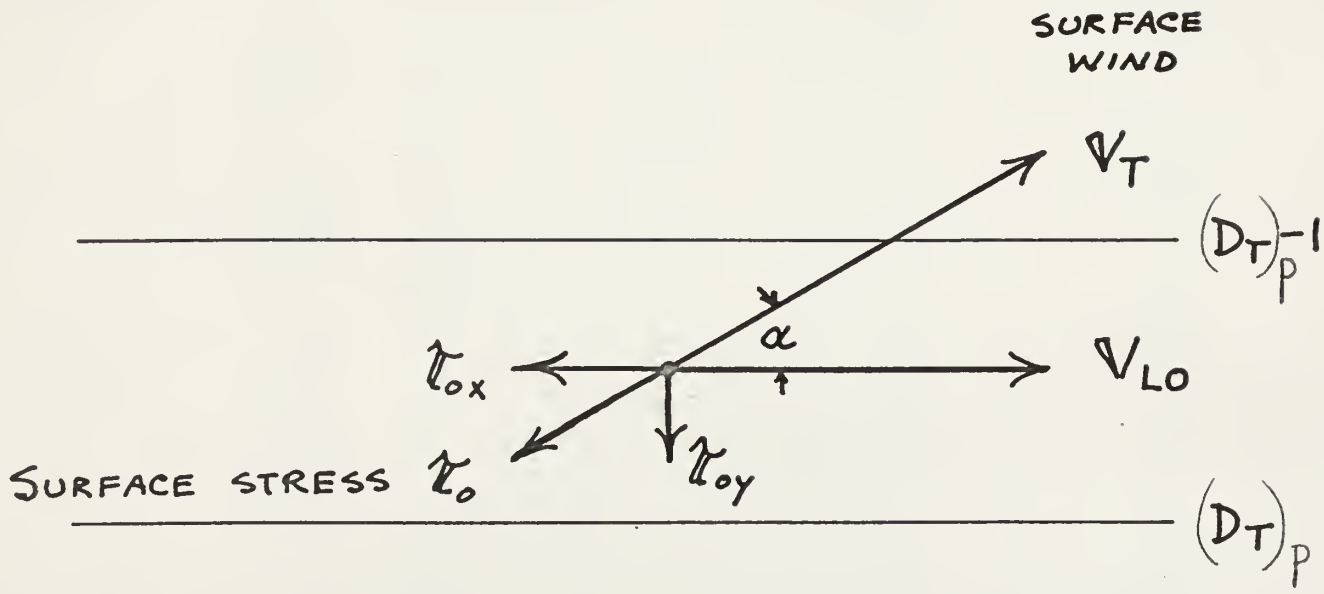

Figure 4. Orientation of surface stress.

Then from (24)

$$\omega_F = \frac{g\bar{\rho}_{LO}}{f}\left[\frac{\partial(C_D u_{LO} V_{LO})}{\partial y} - \frac{\partial(C_D v_{LO} V_{LO})}{\partial x}\right] ,$$

where the local variation of density has been neglected. Expanding this equation

$$\omega_F = \frac{g\bar{\rho}_{LO}}{f}\left[C_D V_{LO}\left(\frac{\partial u_{LO}}{\partial y} - \frac{\partial v_{LO}}{\partial x}\right) + u_{LO}\frac{\partial(C_D V_{LO})}{\partial y} - v_{LO}\frac{\partial(C_D V_{LO})}{\partial x}\right] . \quad (26)$$

The last two terms on the right in (26) were assumed small in comparison with the first and were neglected. The surface friction omega can then be written as

$$\omega_F = -\frac{g p_T}{f R \bar{T}_T} C_D V_{LO} \zeta_{LO} , \quad (27)$$

where the density has been replaced through the equation of state.

Next, the vertical velocities due to varying terrain height will be considered. The value of omega due to the terrain slope ω_T may be written in the form

$$\omega_T = \left(\frac{d\omega}{dp}\right)_T = \left(\frac{\partial p}{\partial t}\right)_T + V_{LO} \cdot \nabla p_T . \quad (28)$$

For a large 3-hourly tendency

$$\left(\frac{\partial p}{\partial t}\right)_T \doteq 5 \text{ mb per 3 hr}$$

and will be neglected. Then

$$\omega_T \doteq V_{LO} \cdot \nabla p_T , \quad (29)$$

and omega at the lower boundary is

$$\omega_{LO} = \omega_T + \omega_F = \mathbb{V}_{LO} \cdot \nabla p_T - \frac{g p_T}{f R T_T} C_D V_{LO} \zeta_{LO} \quad . \tag{30}$$

The geostrophic wind at the lower boundary $\mathbb{V}_{LO}$ is required in (30) in both terms. The geostrophic vorticity ζ_{LO} is also required and is based on $\mathbb{V}_{LO}$

$$\mathbb{V}_{LO} = \mathbb{K} \times \frac{g}{f} (\nabla_p D)_T \quad . \tag{31}$$

Here it is noted that $\nabla_p D$ must be determined at terrain pressure. Thus it is necessary to "reduce" or extrapolate the D_T values at points surrounding the central point. These extrapolated values will be called $(D_T)_p$. The extrapolation will be done on altimetry principles using the previously calculated S_{UL} values for the layer in which the terrain lies. For example, in figure 5, at point ($i+1$), the extrapolated value is

$$(D_T)_{p,i+1} = (D_T)_{i+1} + (S_{UL})_{i+1} \left[Z_{p,i} - Z_{p_T,i+1} \right] \quad . \tag{32}$$

It follows that the gradient of D in the x-direction may be written

$$(D_T)_{p,i+1} - (D_T)_{p,i-1} = \left[D_{T,i+1} - D_{T,i-1} \right] - Z_{p,i} \left[(S_{UL})_{i+1} - (S_{UL})_{i-1} \right] \tag{33}$$

$$+ (S_{UL})_{i-1} \cdot Z_{p_T,i-1} - (S_{UL})_{i+1} \cdot Z_{p_T,i+1} \quad .$$

Similar considerations hold for the y-component. Both equations (32) and (33) are used in making calculations of $\mathbb{V}_{LO}$ and ζ_{LO} for use in equation (30).

The T_T in equation (30) is also calculated by altimetry principles [9]. By definition, the specific temperature anomaly is

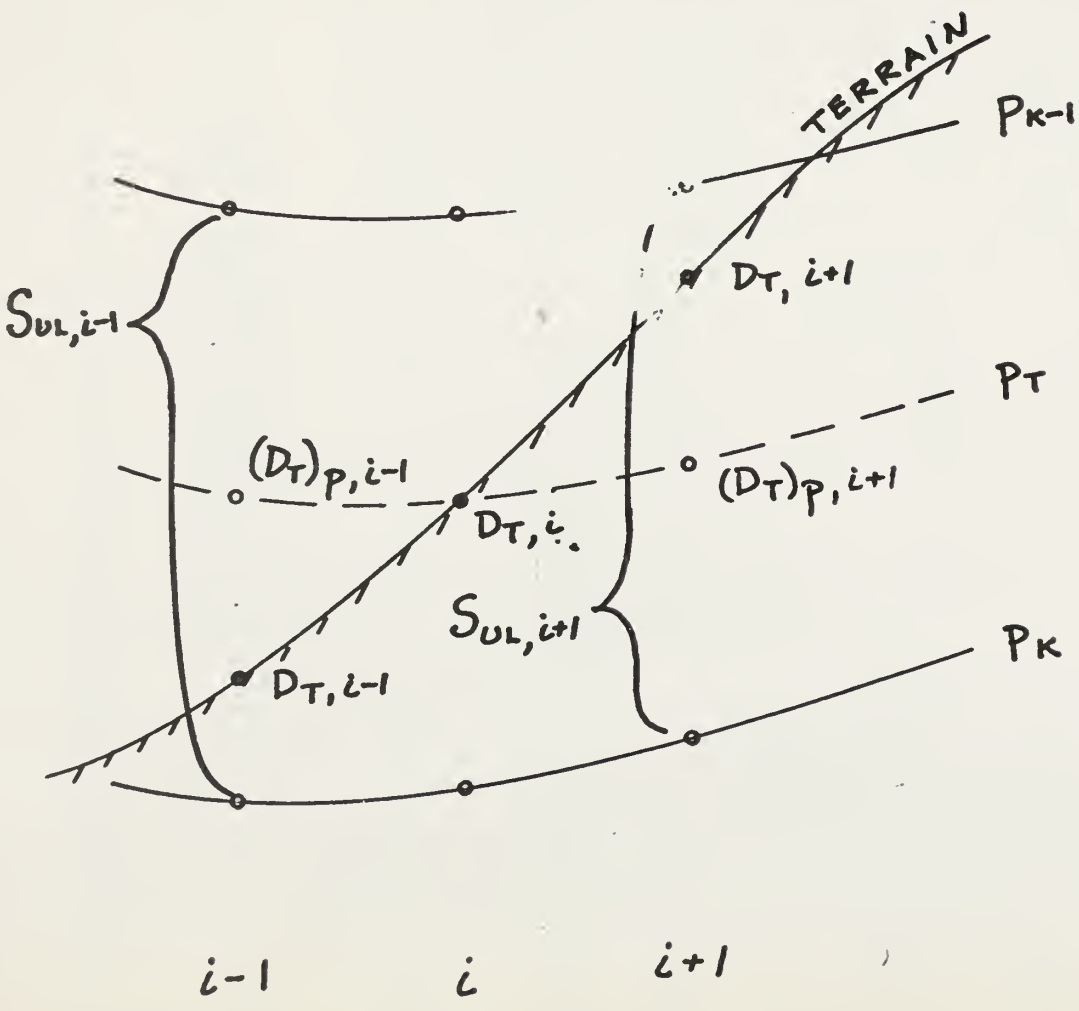

Figure 5. Extrapolation scheme for $(D_T)_p$

$$S = \frac{T - T_p}{T_p} \quad , \tag{34}$$

where T_p, the pressure temperature, is the standard-atmosphere temperature at a given pressure altitude and T is the temperature at a given point. Solving (34) for T and applying to this model gives

$$T_T = T_{p_T}(1 + S_{UL}) \quad . \tag{35}$$

The pressure temperature T_{p_T} is given by

$$T_{p_T} = T_{p_o} - a \cdot Z_{p_T} \tag{36}$$

where $T_{p_o} = 15C$ is the temperature at $Z_p = 0$

and $a = 6.5 \ 10^{-5}$C per cm.

Combining (35) and (36) yields

$$T_T = (T_{p_o} - a \cdot Z_{p_T})(1 - S_{UL}) \quad . \tag{37}$$

Substituting (31), (32), (36) and the geostrophic vorticity into (30) gives the computational forms for ω_T and ω_F

$$\omega_T = \frac{g}{f} J\left[(D_T)_p \, , \, P_T\right] \quad , \tag{38}$$

$$\omega_F = - \frac{g^3 \cdot P_T \cdot C_D \cdot \left|\mathbb{K} \times (\nabla_p D)_T\right| \cdot \nabla^2 (D_T)_p}{f^3 \cdot R\,(T_{p_o} - a \cdot Z_{p_T})(1 + S_{UL})} \quad . \tag{39}$$

Using the finite difference analogs (7) and the standard scaling conventions (11) gives

$$\hat{\omega}_T = \frac{2^{-n} c \hat{m}^2}{\sin\phi} J\left[(\hat{D}_T)_p \, , \, \hat{P}_T\right] \quad , \tag{40}$$

$$\hat{\omega}_F = -\frac{2^{3\ell-n} \cdot C_D \cdot g^3 \cdot \hat{m}^3 \cdot \hat{P}_T \cdot \Delta_R(\hat{D}_T)_P \cdot \nabla^2(\hat{D}_T)_P}{f^3 \cdot \sin^3\phi \cdot d^3 \cdot R \cdot (T_{P_0} - \hat{\alpha}\hat{Z}_{P_T})(1+S_{UL})} \quad . \tag{41}$$

The $\hat{\omega}_{LO}$ is then $\hat{\omega}_{LO} = \hat{\omega}_T + \hat{\omega}_F$.

The computational time to obtain $\hat{\omega}_{LO}$ is about 40 seconds.

The coefficient of drag C_D in (30) is the same as that defined by Cressman [13], and values of C_D were obtained from the Joint Numerical Prediction Unit, United States Weather Bureau, Suitland, Maryland.

The height of the terrain Z_T is an area-smoothed value, and for the synoptic cases presented the heights used were obtained from the FNWF. The terrain heights have certain deficiencies due to rather heavy smoothing. They are being replaced with values averaged over a 1-degree latitude/longitude area, as determined by Berkofsky and Bertoni [14].

5. Some Features of the Computer Program

The Control Data Corporation 1604 digital computer was used in this investigation. It has a core memory of 32,768 words of 48 bits each, with a typical add time of 7.2 microseconds.

The initial "guess" field for omega at the various pressure levels is obtained from the ω_{LO} value previously computed. It was expected that the influence of a particular ω_{LO} at the lower boundary would decrease nearly exponentically with height above the terrain, hence the initial guess field was computed by $\omega_K^{(0)} = \omega_{LO} \cdot 2^{-t}$,

where t = 1 for the first pressure level above the terrain, t = 2 for the second, etc. This procedure accelerates the convergence of the relaxation scheme appreciably, as compared to an initial guess field of zero.

Provision is made in the computer program to determine the influence

of the lower boundary on the omega fields in various ways.

(a) The terrain-induced vertical velocity ω_T and the frictionally-induced velocity ω_F may be calculated separately or jointly.

(b) ω_{LO} may be set equal to zero. Here the terrain is still present and the lower boundary follows the variable height of the surface of the earth.

(c) The computation scheme can be altered to test the effect of inserting the ω_{LO} values at an artificial lower boundary, calculated on the assumption that the height of the terrain is zero. The pressure at this lower boundary is not constant and corresponds to the sea-level pressure map. This simulates closely the approximations normally used [3], [10], [13], wherein the lower boundary values are arbitrarily assigned to the lowest constant-pressure level of the model. Thus, they are not only applied at an incorrect altitude, but ignore the presence of internal boundaries due to the intersection of pressure surfaces and terrain.

(d) The forcing function C_J of equation (13), which involves the D- and T-fields responsible for the large-scale vertical velocities, can be set equal to zero and a solution obtained with only the lower boundary values ω_{LO} present. This essentially shows the decay of the influence of the ω_{LO} with height, subject here only to the static stability variations in the atmosphere (see equation (6)).

Examples of the various possibilities (a) to (d) will be given in the next section.

Many modes of operation of the computer program are possible and allow a wide variety of side products to be obtained if desired. The more important of these are listed below.

D_k at 5 levels

T_k at 6 levels

σ_k at 4 levels

S_{UL}

P_T

T_T

ω_T

ω_F

ω_{LO}

φ_k at 4 levels

ω_k at 4 levels

All of these can be obtained in computer-analyzed form on machine-drawn and labelled charts. All the charts of this investigation were produced in this manner except cross sections.

It is to be noted that on the charts of ω_k wherever the terrain projects through a pressure level, the value $+111$ is printed at that grid point, and delineates the internal boundary.

The computer program has "smoothers" incorporated to control irregularities in higher-order finite differences of the input data. These smoothers are of the form

$$\tilde{\tilde{A}}_{ij} = A_{ij} + K\nabla^2 A_{ij} ,$$

where $\tilde{\tilde{A}}$ is the smoothed data,
A is the unsmooth data,
and K is the smoothing coefficient and is equal to 1/8.

This smoother is applied once to the $\nabla^2 \hat{D}_K$, $\nabla^2 \hat{T}_K$, and $\nabla^2 J(\hat{D}_K, \hat{T}_K)$ fields.

6. Discussion of Results

The static stability is a bulk value, since it is derived by fitting a parabola to temperatures from three pressure levels of hydrostatically-checked analyses. The computed σ_K vary as expected with regard to the relative stability characteristics of various air masses at lower levels and with respect to the proximity of the stratosphere at upper levels. The observed rapid variation of the static stability may not justify the neglect of the derivatives of σ_K in certain areas. These effects are to be included in future computations. Some typical charts are displayed in Appendix C, pages 136, 139, 142, and 145.

The influence of the lower boundary on the vertical velocity field was investigated, and some typical charts of the results are displayed in figures 6 to 10. Note that the decay of velocity with distance from the surface of the earth is very rapid, and even large values of ω_{L0} (at levels below 850 mb) do not exert a significant influence beyond the 500-mb level.

In many models, the vertical velocity at the lower boundary is artificially assigned to the lowest pressure level of the model. The present model was constrained to operate in this mode for a few tests, one of which is presented in figures 11 to 15. Inspection shows that, as expected, there is little disagreement in areas where the terrain is near zero height, but large discrepancies arise at those points in the vicinity of prominent terrain features. Areas where this disagreement is the largest are obviously the Cordilleras of North America and the Himalayan Plateau of Asia. The transparent overlay at the end of this report may be used on figures 6 through 10.

Figure 6. Omega at lower boundary.

Figure 7. Omega at 850 mb with $C_J = 0$

Figure 8. Omega at 700 mb with $C_J = 0$.

Figure 9. Omega at 500 mb with $C_J = 0$.

Figure 10. Omega at 300 mb with $C_J = 0$

Figure 11. Omega at lower boundary.

Figure 12. Omega at 850 mb with terrain "in."

Omega at 850 mb with terrain "out."

Figure 13. Omega at 700 mb with terrain "in."

Omega at 700 mb with terrain "out."

Figure 14. Omega at 500 mb with terrain "in."

Omega at 500 mb with terrain "out."

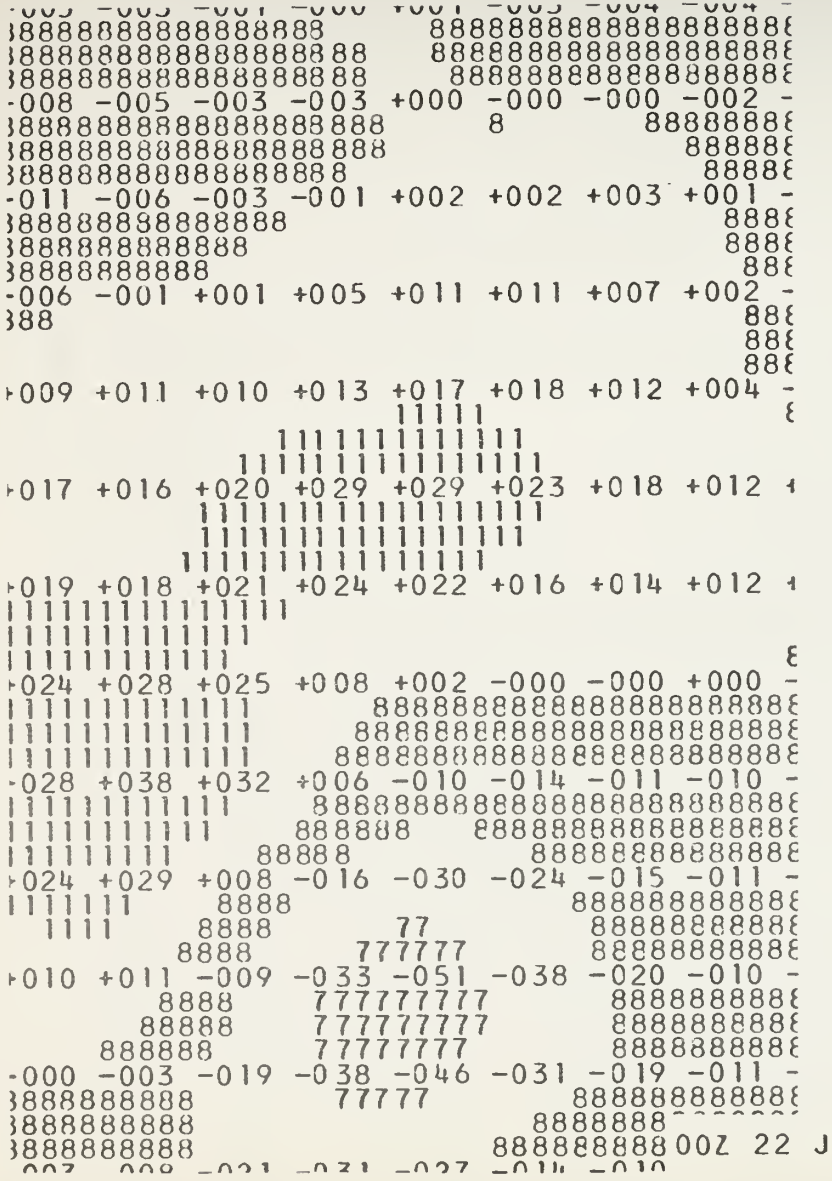

Figure 15. Omega at 300 mb with terrain "in."

Omega at 300 mb with terrain "out."

7. Vertical-Velocity Computations for a Particular Synoptic Situation

The California snow storm of January, 1962 was selected to provide data for vertical-motion analyses. It was considered that this storm might provide results which would show the development of a situation which was inadequately forecast. An extensive synoptic investigation of this storm has been made by Ikegami [15].

The required input data of D values and temperatures at 1000, 850, 750, 500 and 300 mb were obtained from FNWF. Times chosen for analyses were 1200Z 17 January, 1200Z 20 January, 0000Z 21 January, 1200Z 21 January, 0000Z 22 January, 1200Z 22 January, 1200Z 23 January, and 1200Z 26 January.

Appendix A contains extracted portions of hemispheric prints which measure 30 x 26 inches. The extracts are the same scale as the originals. Since various cross sections are provided, a line delineating the cross section path is indicated. Also, grid points three and four are underlined. The Monterey Bay area lies between these two points, as shown by the continental outlines drawn on the chart on page 44 of Appendix A. This extract gives the pressure at terrain height for 0000Z 22 January. If it is desired to use the transparent overlay on these charts, shift the overlay to the left one grid point for proper display.

As indicated earlier, wherever terrain projected through any pressure level, the value +111 was printed at that grid point. For the maps provided, only the 850-mb level is affected. Since a point within the terrain was not relaxed in computing the omega fields, the terrain value of omega was substituted at that grid location.

The printed values of omega multiplied by 10^{-4} give units of mb/sec. Vorticity values multiplied by 10^{-6} give units of sec^{-1}.

a. Analysis for 17 January

(See Appendix A, pages 45 to 54 ; Appendix B, page 106)

In general, California was under the influence of subsidence associated with a high located to the west. However, in the northwestern United States a wave developed on a stationary front oriented from northwest to southeast. This wave continued to develop and the associated cold front brought heavy rains into California.

Rain began in the Monterey area about 1500Z 19 January and continued through 1300Z 20 January. Frontal passage occurred about 1000Z 20 January. The pressure rise was small and no appreciable increase in pressure was noted for 48 hours, due to a surface trough which remained in the area.

Program outputs of the region where this development occurred depict ascending air at all levels. Further, relative vorticity analyses show a maximum located northwest of the centers of rising air.

Appendix C, page 119, shows the presence of a blocking high at the 500-mb level. The block's orientation and the downstream cold low became the controlling factors in the movement of the surface wave.

b. Analysis for 20 January

(See Appendix A, pages 54 to 59 ; Appendix B, page 107 .)

By 1200Z the front had passed Monterey, but intermittent showers continued to about 1800Z. The center of ascending air was located northeast of the Monterey area with higher vertical velocities at the upper levels. Strong subsidence to the northwest was apparently moving eastward and would soon dominate the local weather.

But, as seen in Appendix C, page 121, the previously-mentioned block was now fully developed. The downstream low became quasi-stationary and

the area of subsidence remained to the west.

c. Analysis for 21 January

(See Appendix A, pages 59 to 77; Appendix B, pages 108 to 110.)

The 500-mb chart for 0000Z (Appendix C, page 128) shows essentially the same situation as existed 12 hours earlier. The temperature of the cold low was near -40C. Moreover, this tongue of cold air extended down to the 1000-mb level. However, the ascending air was now located southeast of Monterey, and higher vertical velocities were found at lower levels.

The 1200Z analyses show that the center of maximum relative vorticity and ascending air were coincident at low levels, i.e., through 850 mb. Using the terrain boundary on the 850-mb chart, it appears that topography restrained the lower portion of the rising column, shearing it from the main cell.

Rain commenced locally at 0600Z 21 January. Snow pellets began falling about 1400Z and snow showers began at 1615Z. Throughout the period ending 1000Z 22 January, snow showers, snow pellets and rain were frequent.

d. Analysis for 22 January

(See Appendix A, pages 77 to 95; Appendix B, pages 110 to 115.)

The significant aspect at 0000Z was the change in direction of movement of the cell of rising air to the southwest. Vertical velocities decreased near points three and four at the 850-mb surface. Appendix C, pages 136, 139, and 142, shows the extent of low-level instability. However, to the west, subsidence was clearly increasing at all levels and now appeared to be moving to the east.

The 1200Z results show further movement and intensification of

subsidence as it proceeded into northern California. The ascending air continued moving southwestward. The surface low, after having reached a position in southeastern Nevada, moved southwest and weakened west of Lower California. At 1200Z 22 January, it was situated over the Los Angeles area.

e. Analysis for 23 January

(See Appendix A, pages 95 to 100; Appendix B, page 115)

These 1200Z charts, 24 hours later than the previous analyses, show points three and four were under the direct influence of descending motion, save for a small area of rising air due to terrain effects near point four. The velocity of the ascending air to the southeast generally decreased and the cell appeared to be weakening.

In Appendix C, pages 146 to 156, the shift of cold temperatures and the trough towards the southwest and the weakening of the block at 500 mb are depicted.

f. Analysis for 26 January

(See Appendix A, pages 100 to 105; Appendix B, page 116.)

The entire West Coast was under the influence of subsidence and little evidence remained of the column of rising air. Appendix C, page 157, shows the trough had resumed normal west-to-east movement.

g. Conclusions

The preceding analyses suggest that had this vertical velocity data been available, the forecast of fair and sunny conditions for 21 January would not have been issued. The vertical motion fields, together with temperature analyses, indicate the impending storm.

The omega fields were compared to the surface analyses as transmitted by facsimile, and indicate that the direction of vertical motion

might have been inferred from conventional map analyses alone. However, the magnitude of the velocities of ascending air in the surface trough could hardly have been appreciated from such maps.

Lack of time precluded computing vertical velocities for other synoptic situations. Also, as interesting and encouraging as these indications are, it should further be pointed out that the results displayed are for an area of abundant data. It remains to be seen how useful and accurate vertical-velocity computations are in areas of sparse upper-air data.

The outputs of this program can form the basis for other investigations in the field of numerical forecasting. Presently, the vertical velocities obtained here are being used to compute the transformation of potential energy to kinetic energy on a hemispheric scale.

With prognostic D and temperature fields, prognostic vertical motions can be computed. The addition of hemispheric dew-point analyses and prediction would permit forecasts of cloudiness and precipitation. The contribution of the release of latent heat to the stability parameter could then be included. The obvious application of the omega fields to a multi-level forecast model is another possibility.

On the hemispheric charts, numerical shading between plus and minus areas of vertical motion imparted an appearance of cloud patterns. Since facsimiles of TIROS IV cloud pictures were available, two samples were chosen for comparison.

Appendix D contains the TIROS pictures and the applicable omega fields. Page 159 is the 0501Z 17 May 1962 TIROS observation; an apparent vortex is indicated near 35N 163E. Here the vertical motion charts lag the observation by seven hours.

Page 165 is a 2220Z 29 May 1962 picture. A vortex is located near 42N 100W. The omega charts are for a period about two hours later.

The observations and representations are well correlated. Perhaps further study would enable the cloud type to be correlated with the vertical-velocity field with respect to sign, magnitude, and level.

APPENDIX A

EXTRACTS FROM HEMISPHERIC PRINTS OF OMEGA AND RELATIVE VORTICITY FIELDS

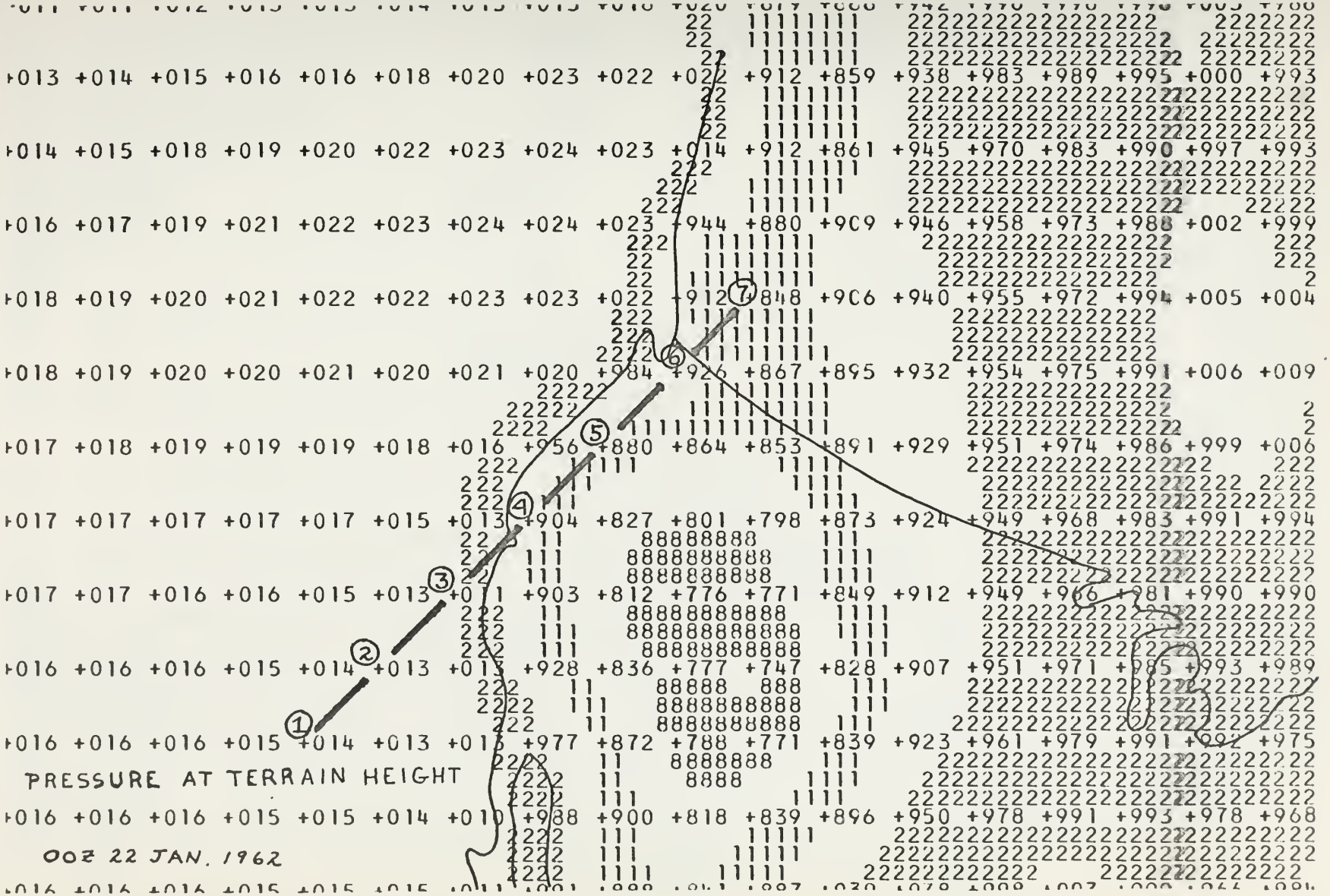
PRESSURE AT TERRAIN HEIGHT
00Z 22 JAN. 1962

12Z 17 JAN 82 OMEGALO

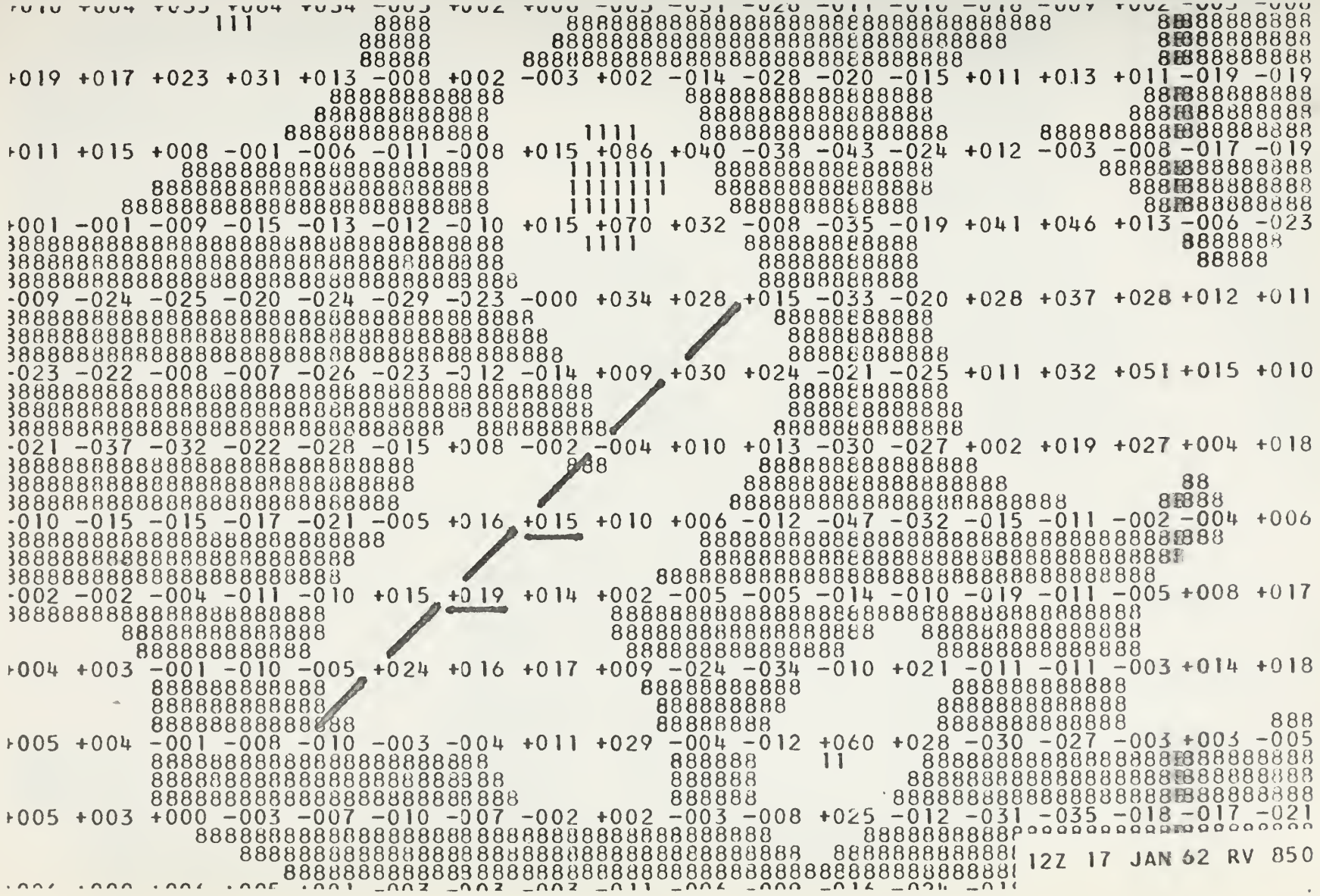
12Z 17 JAN 62 RV 850

12Z 17 JAN 62 OMG 850

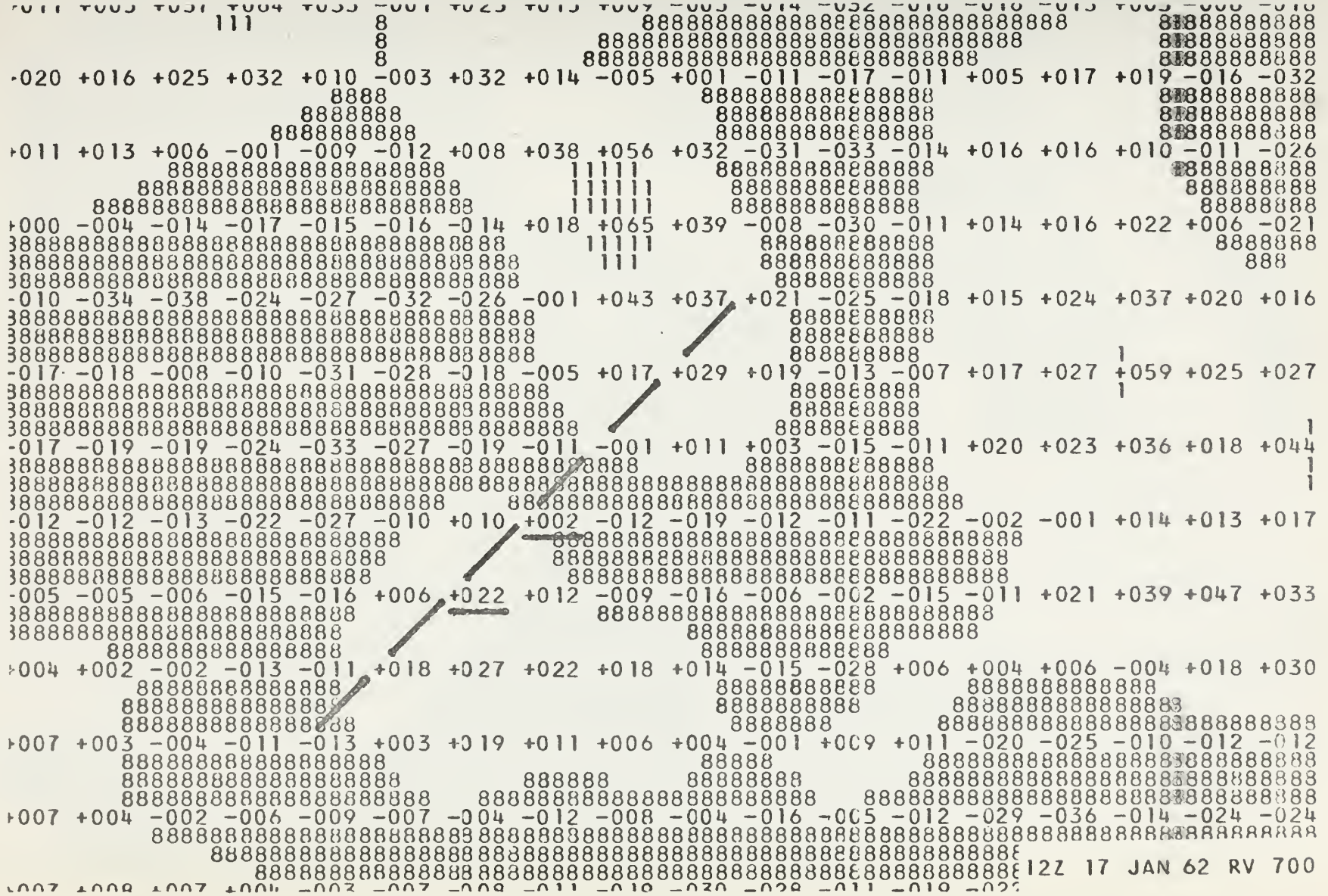
12Z 17 JAN 62 RV 700

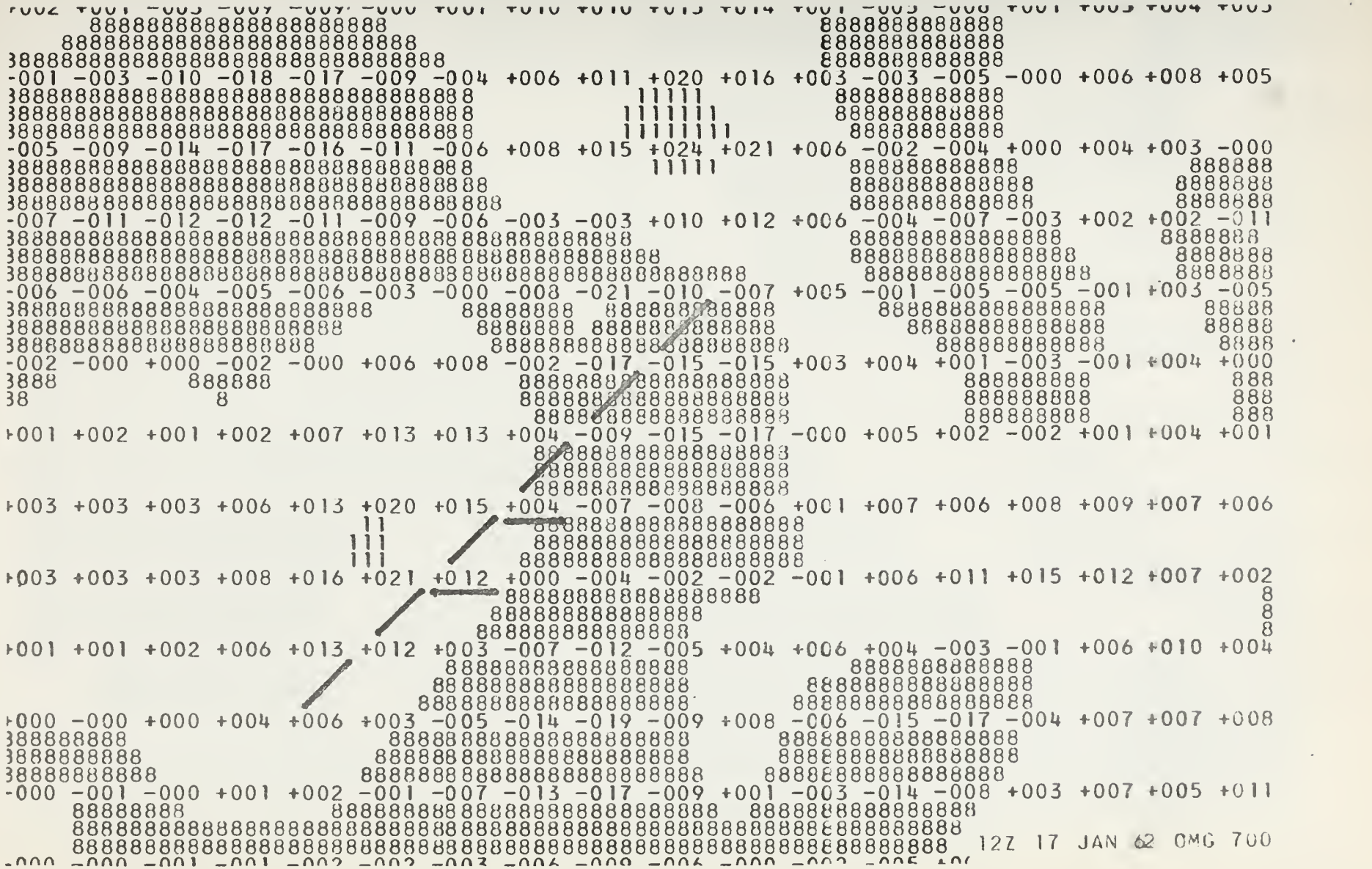
12Z 17 JAN 62 OMG 700

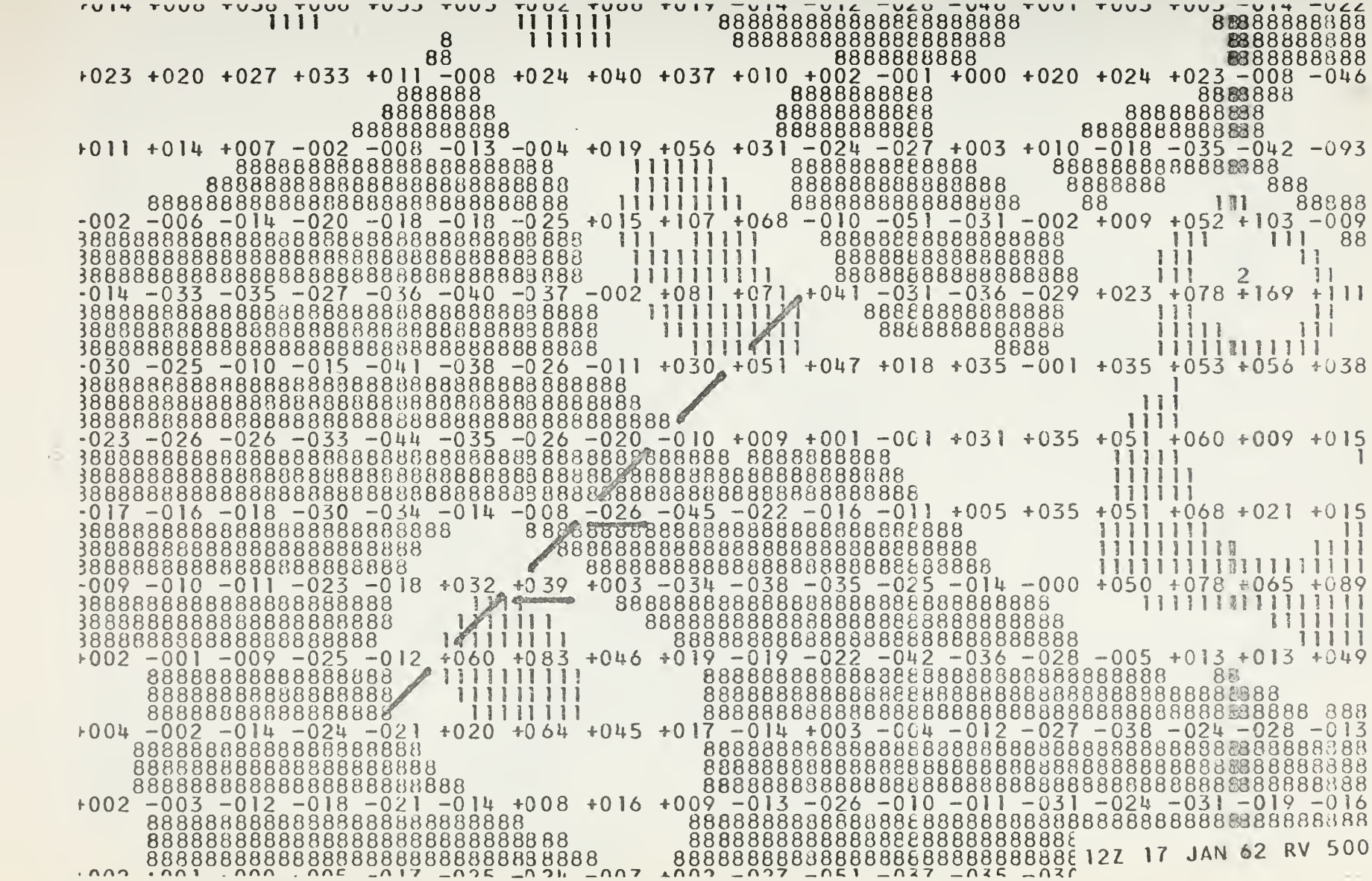
12Z 17 JAN 62 RV 500

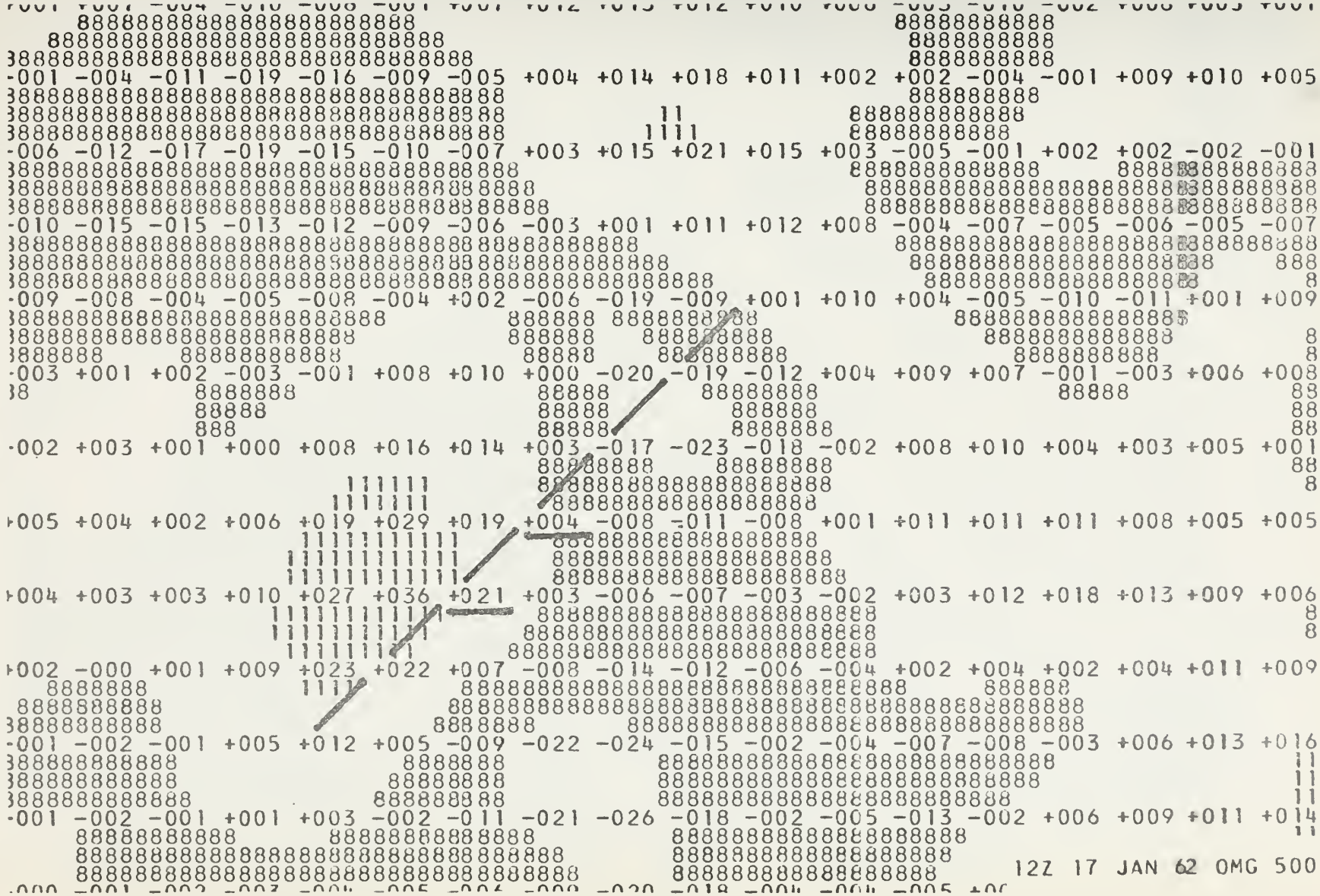
12Z 17 JAN 62 OMG 500

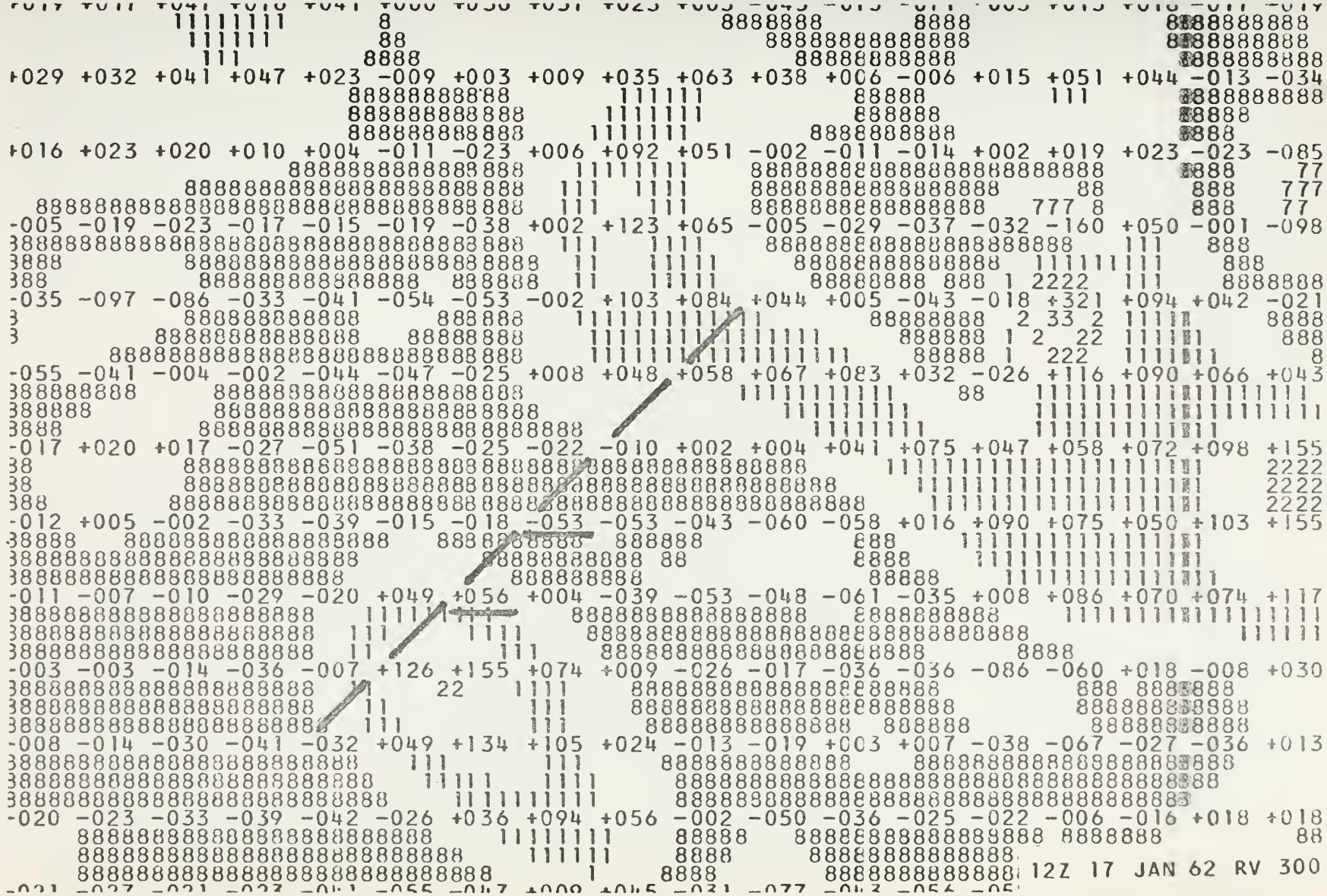
12Z 17 JAN 62 RV 300

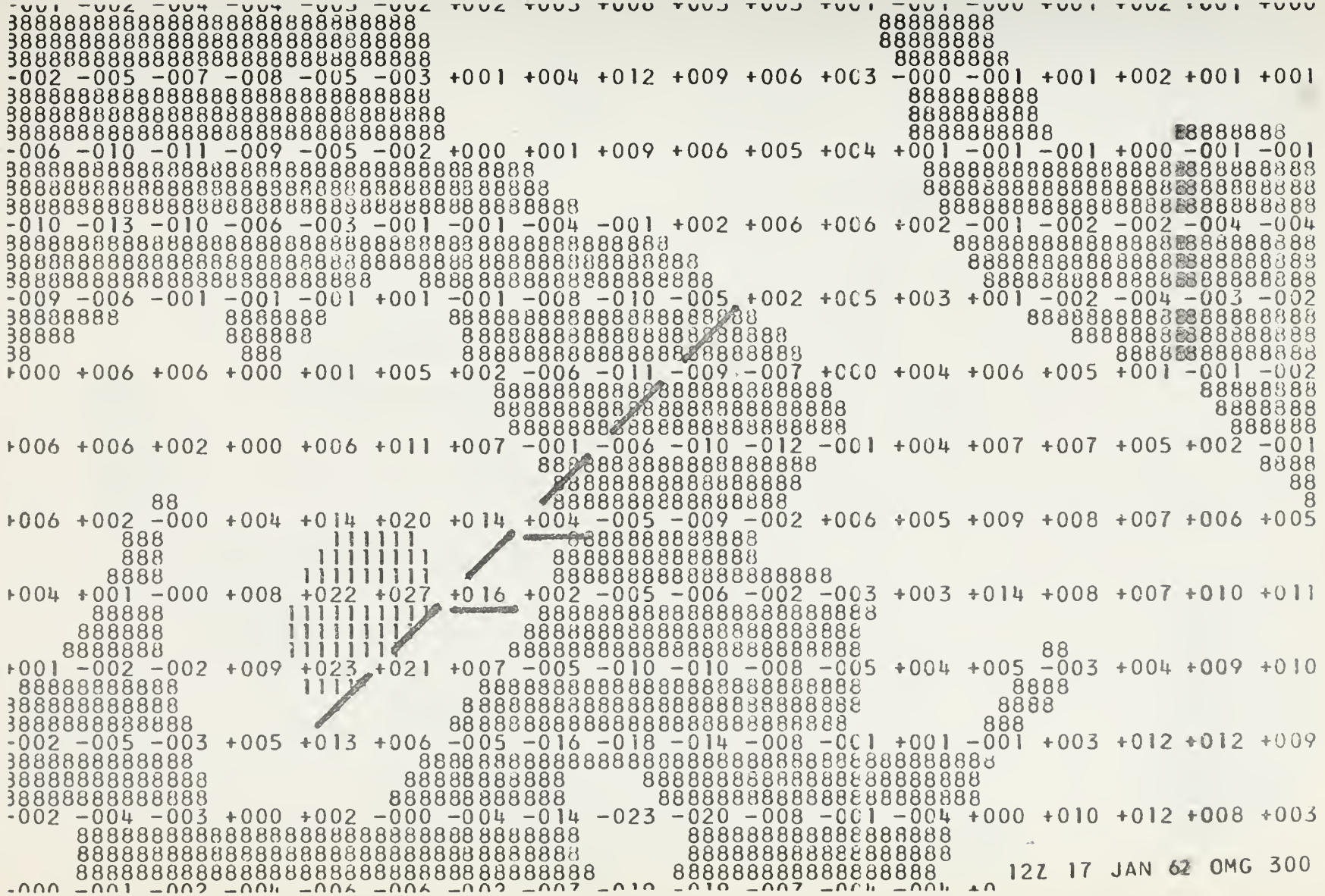
12Z 17 JAN 62 OMG 300

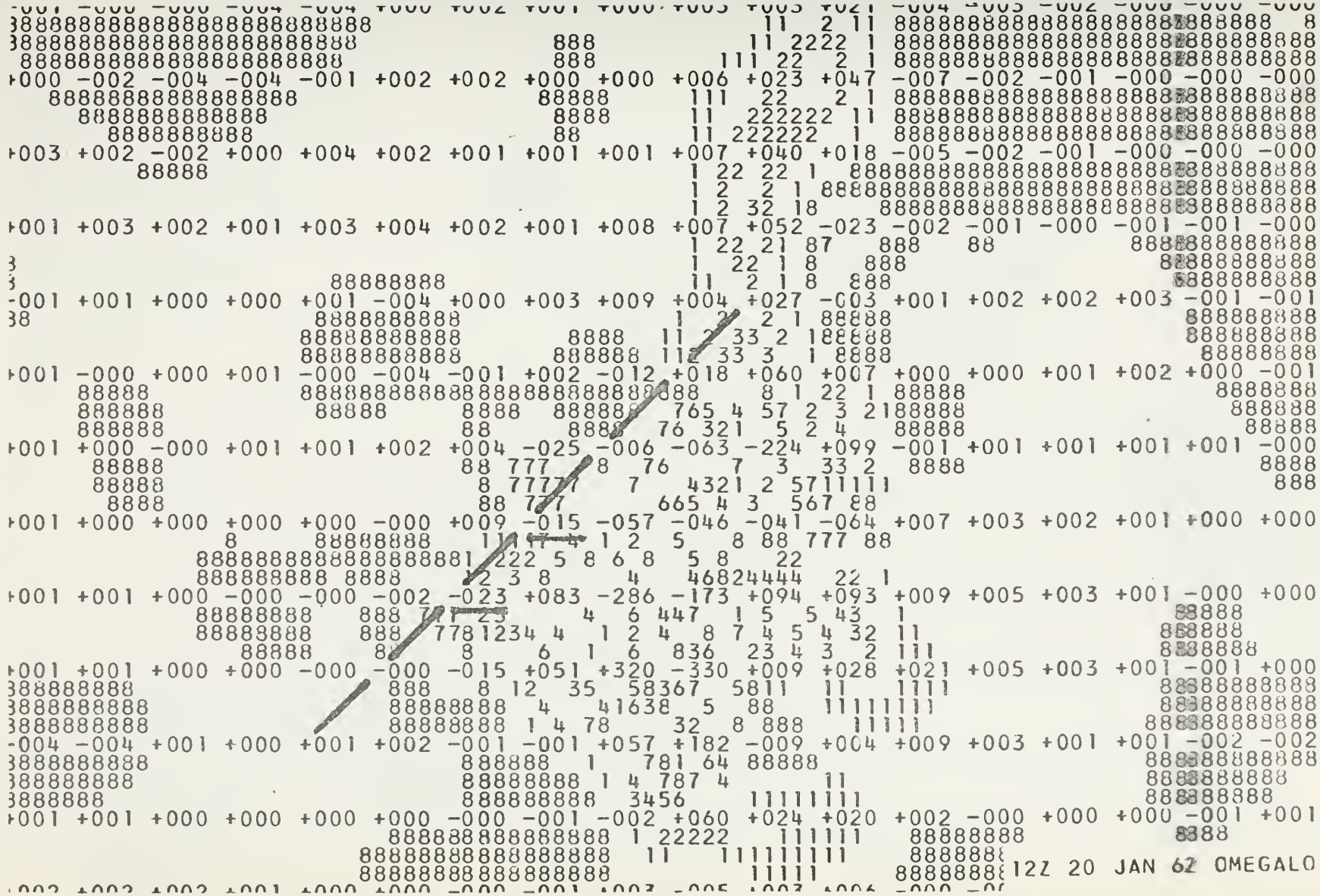
12Z 20 JAN 62 OMEGALO

12Z 20 JAN 62 OMG 850

12Z 20 JAN 62 OMG 700

12Z 20 JAN 62 OMG 500

12Z 20 JAN 62 OMG 300

00Z 21 JAN 62 OMEGALO

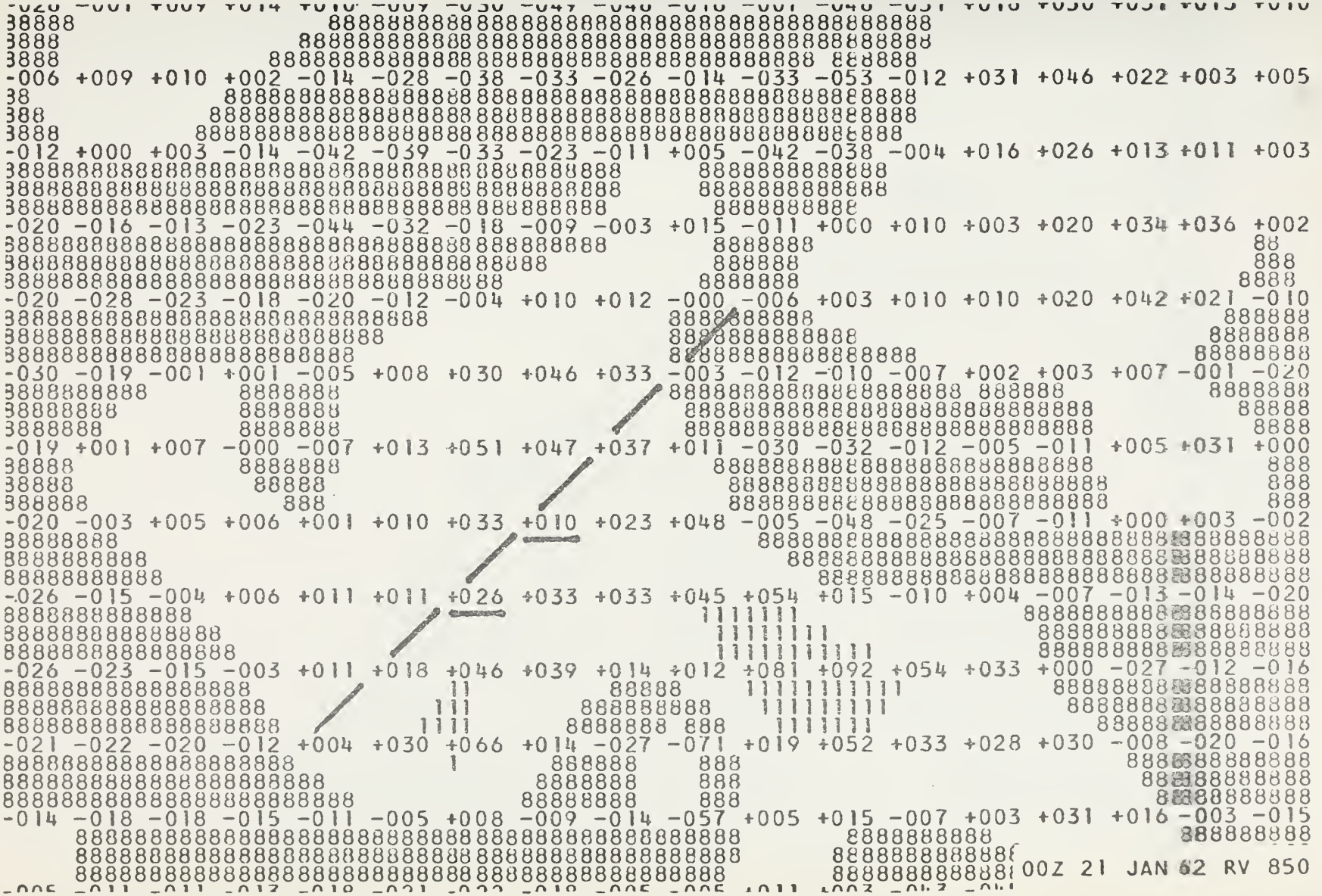
00Z 21 JAN 62 RV 850

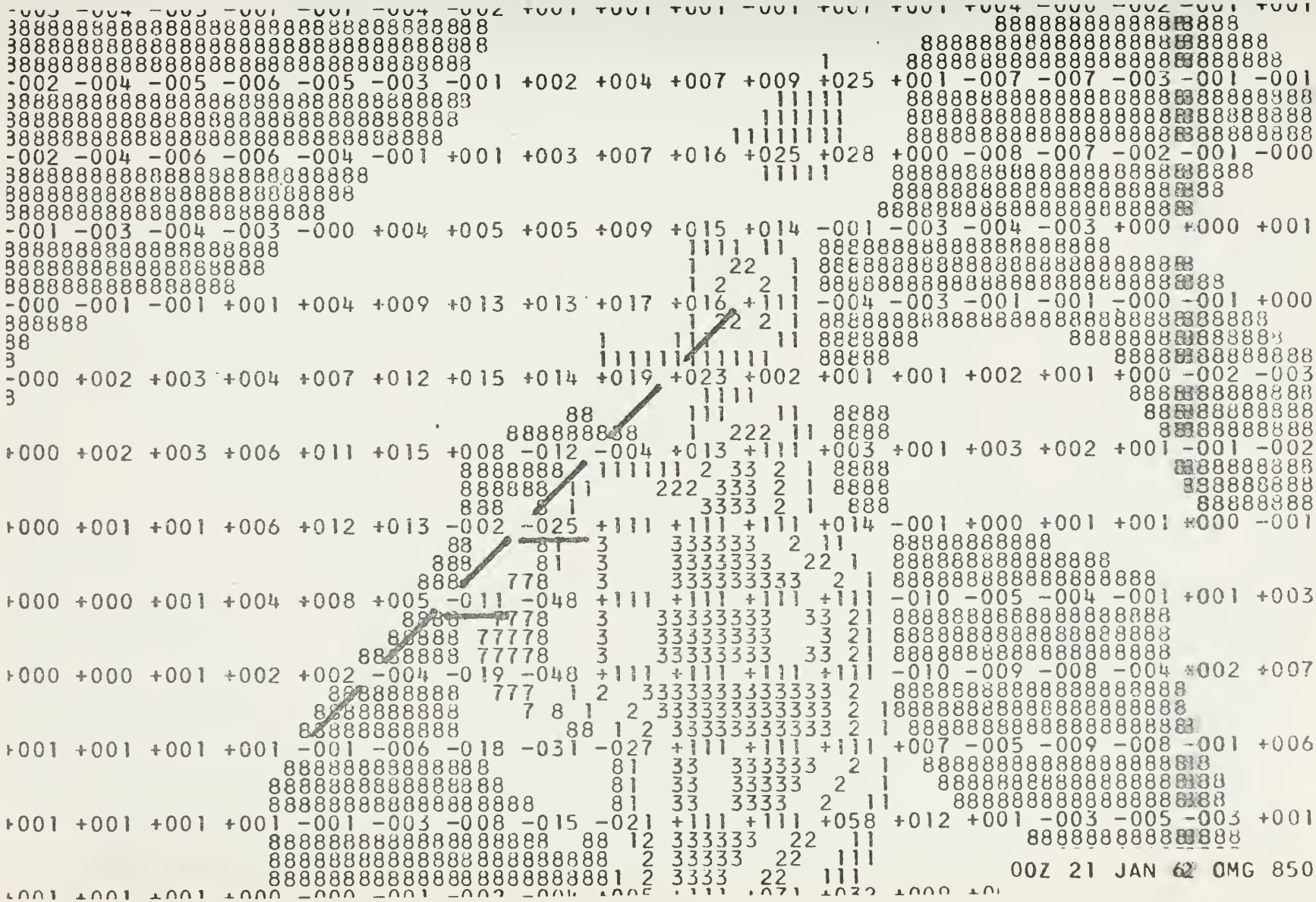
00Z 21 JAN 62 OMG 850

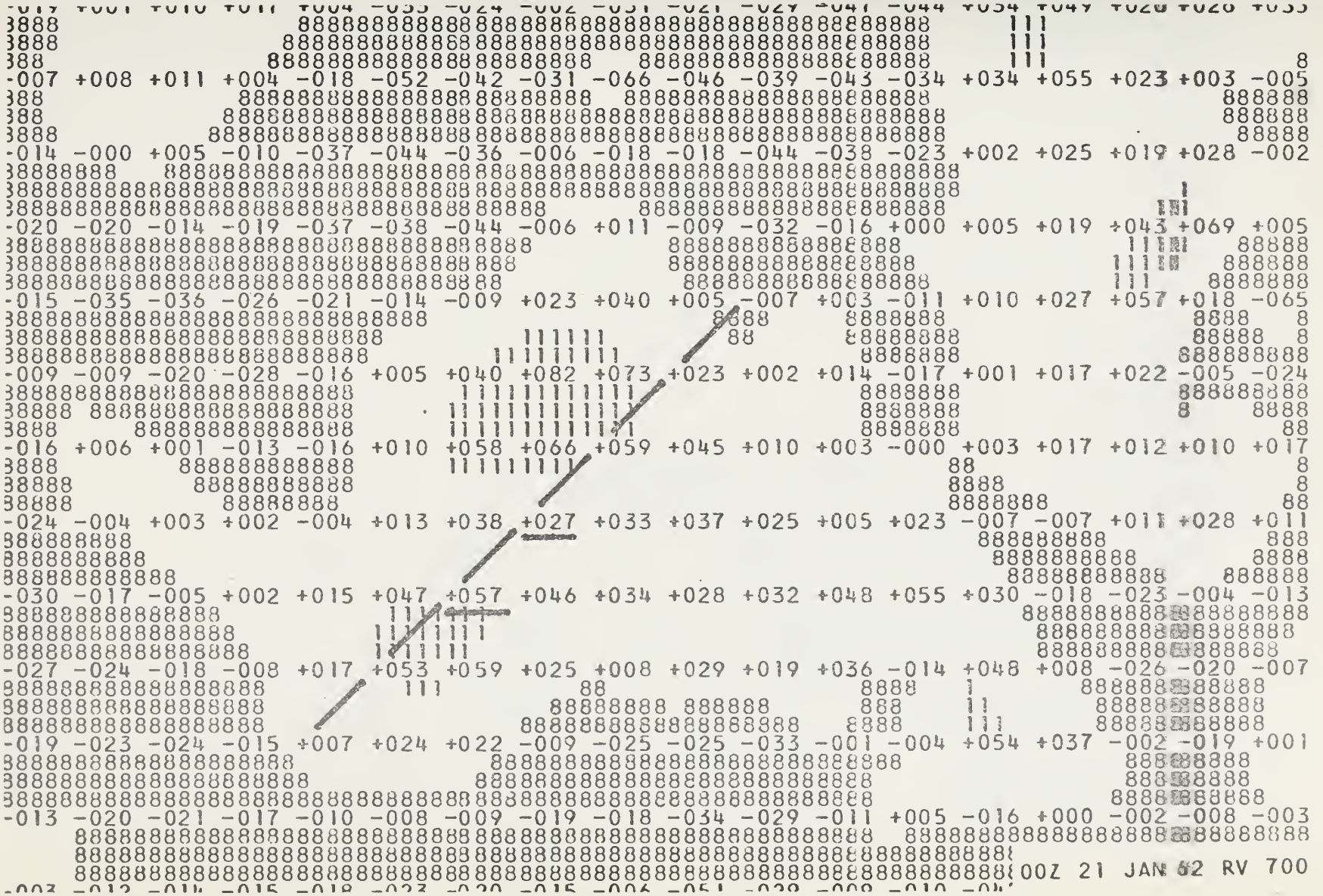
00Z 21 JAN 62 RV 700

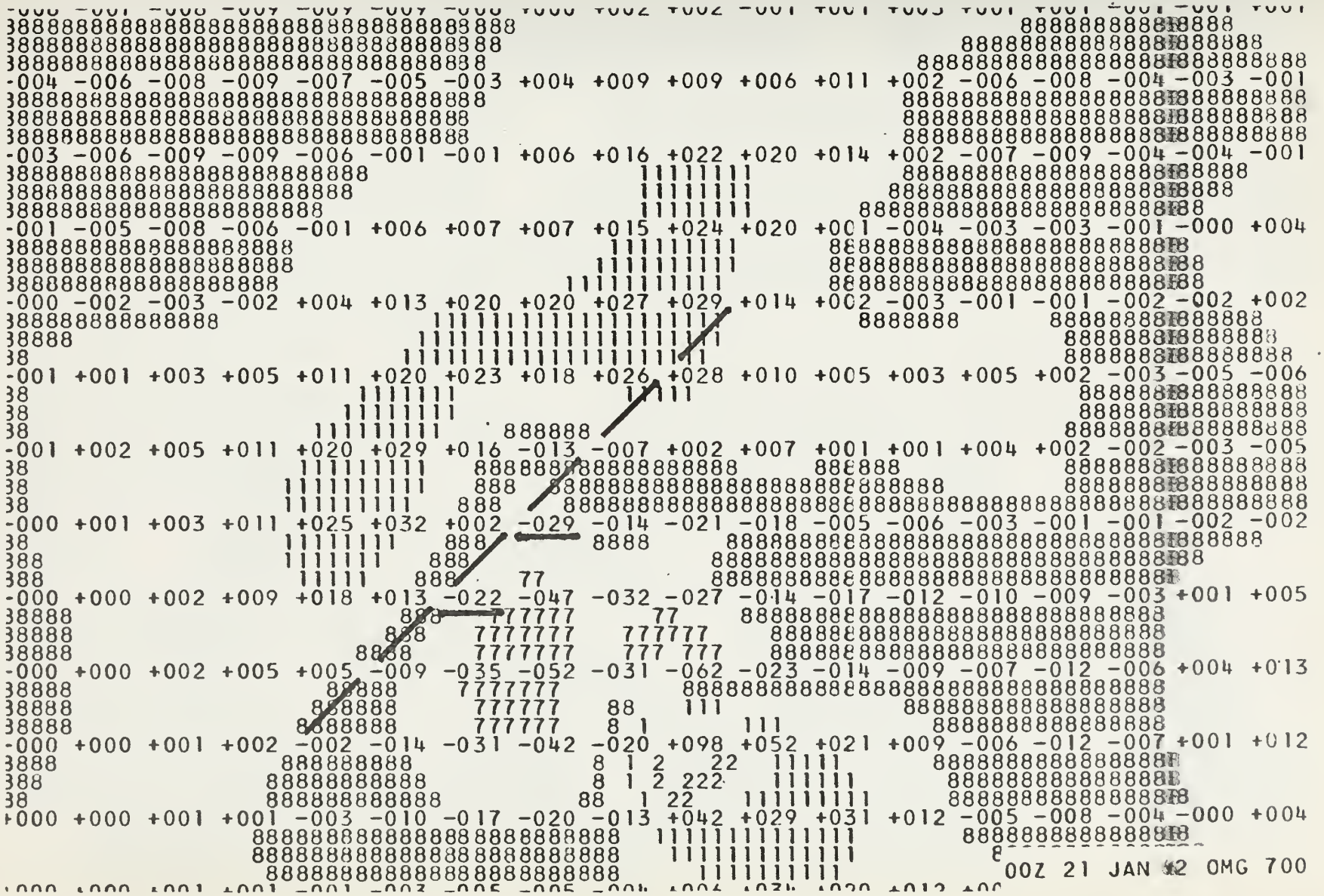
00Z 21 JAN 82 OMG 700

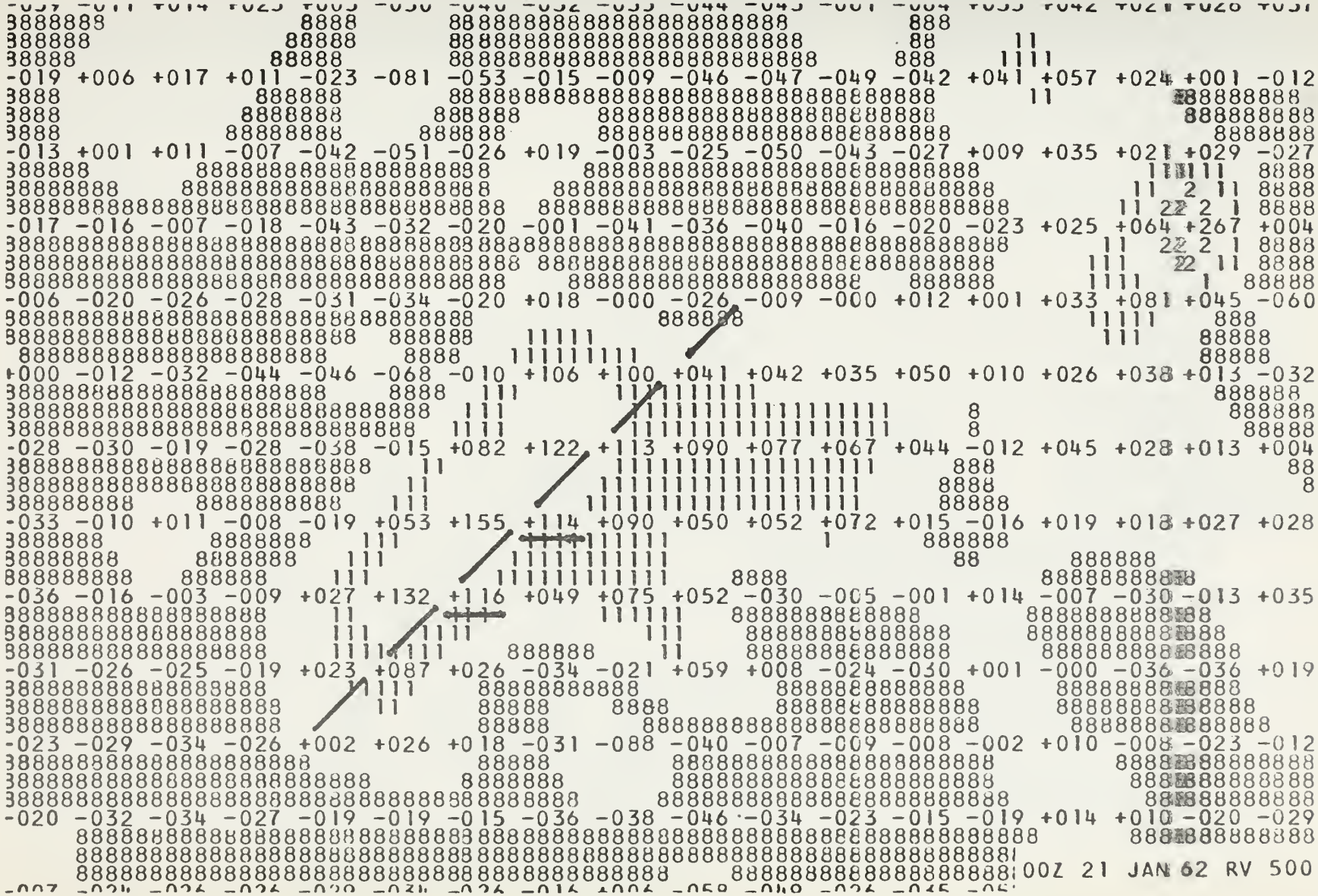
00Z 21 JAN 62 RV 500

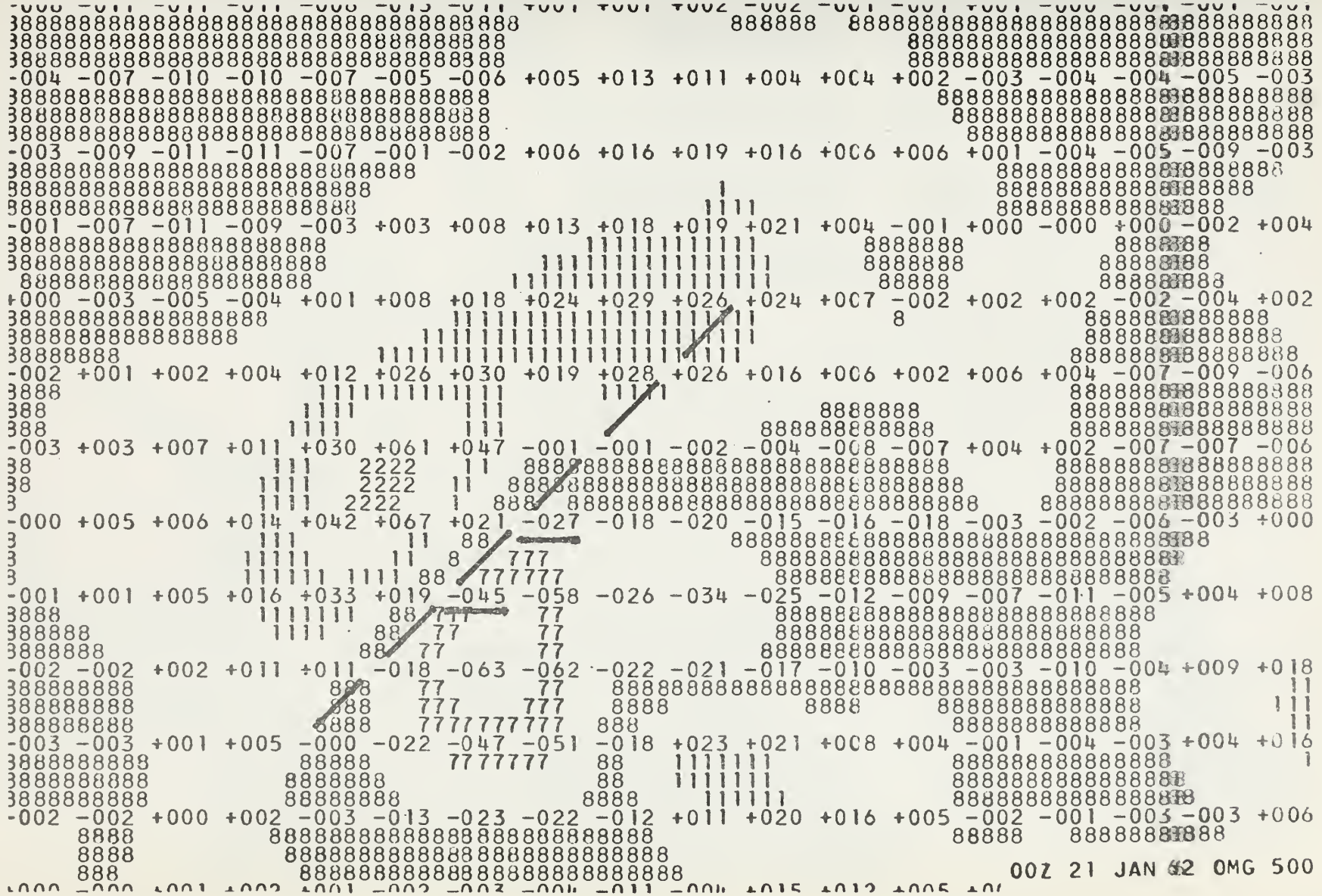
00Z 21 JAN 82 OMG 500

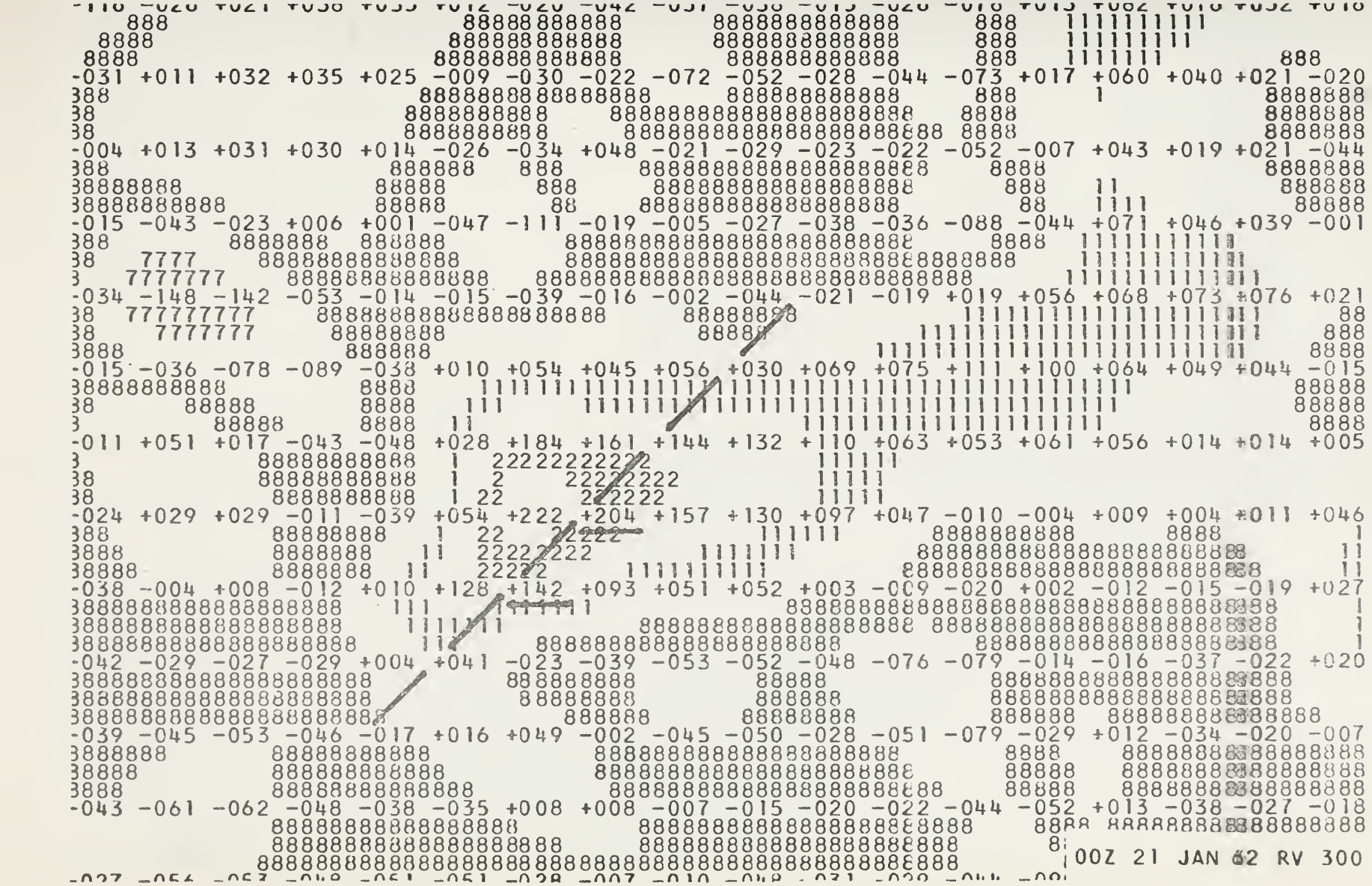
00Z 21 JAN 62 RV 300

00Z 21 JAN 82 OMG 300

12Z 21 JAN 62 OMEGALO

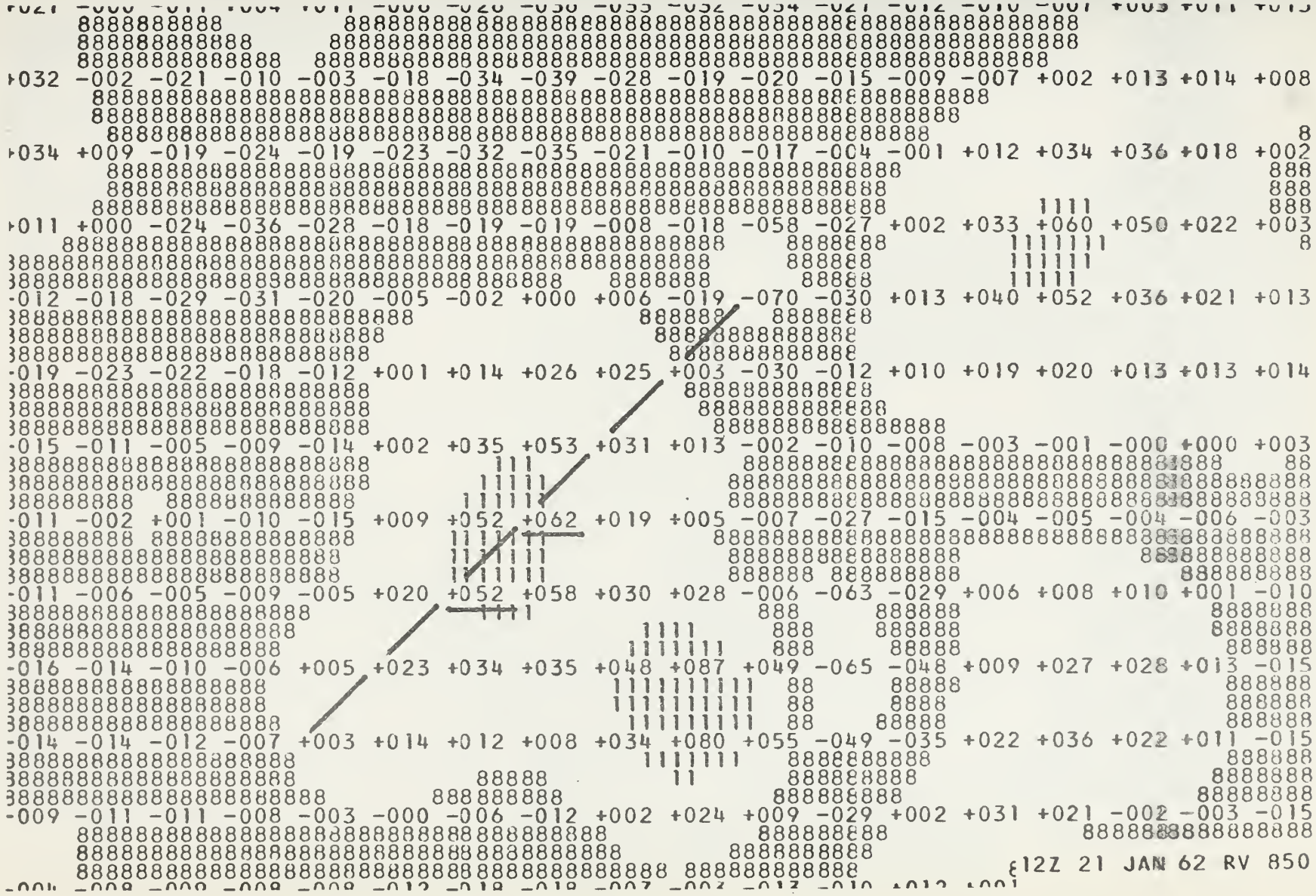
12Z 21 JAN 62 RV 850

12Z 21 JAN 82 OMG 850

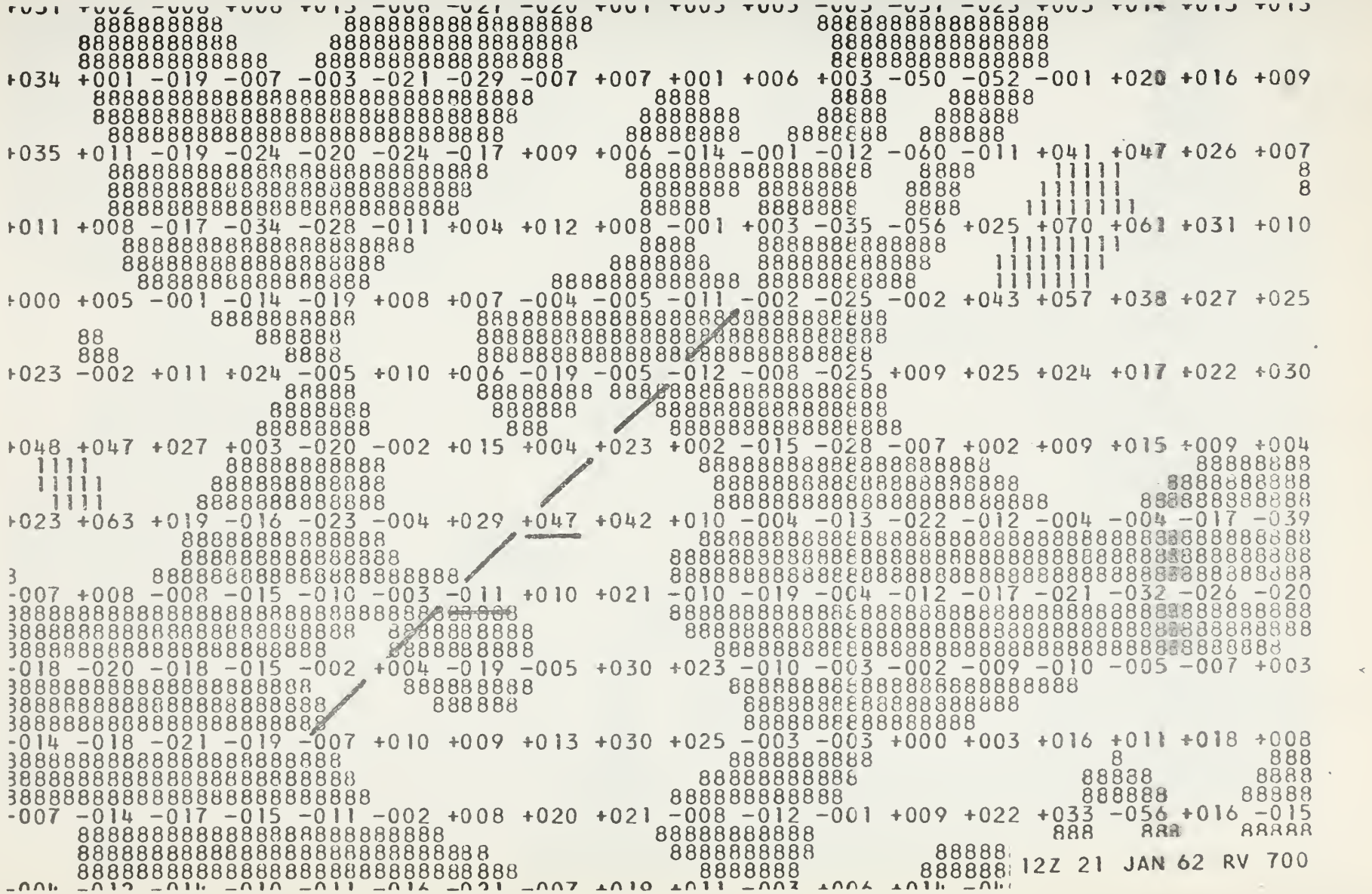
12Z 21 JAN 62 RV 700

12Z 21 JAN 62 OMG 700

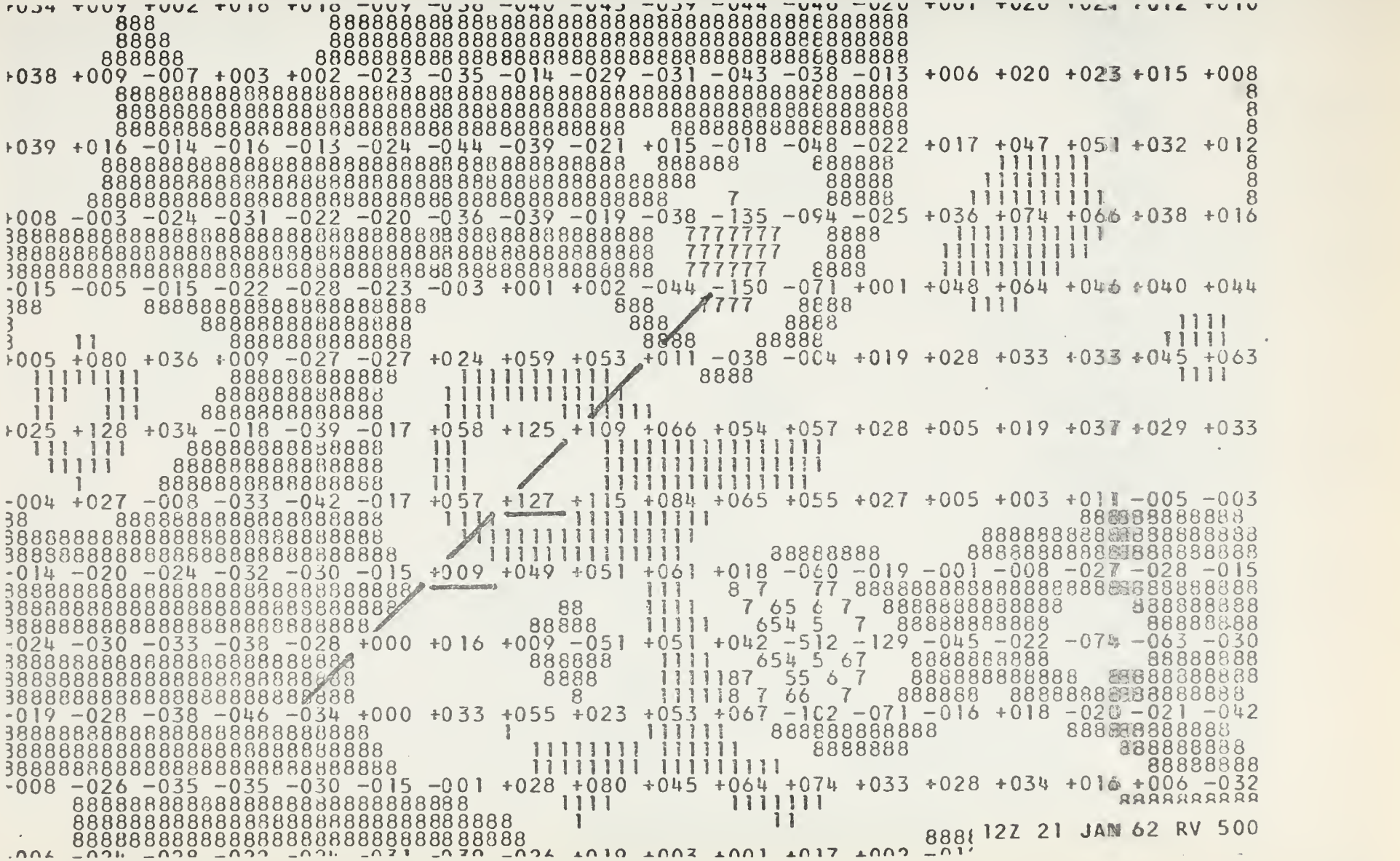
12Z 21 JAN 62 RV 500

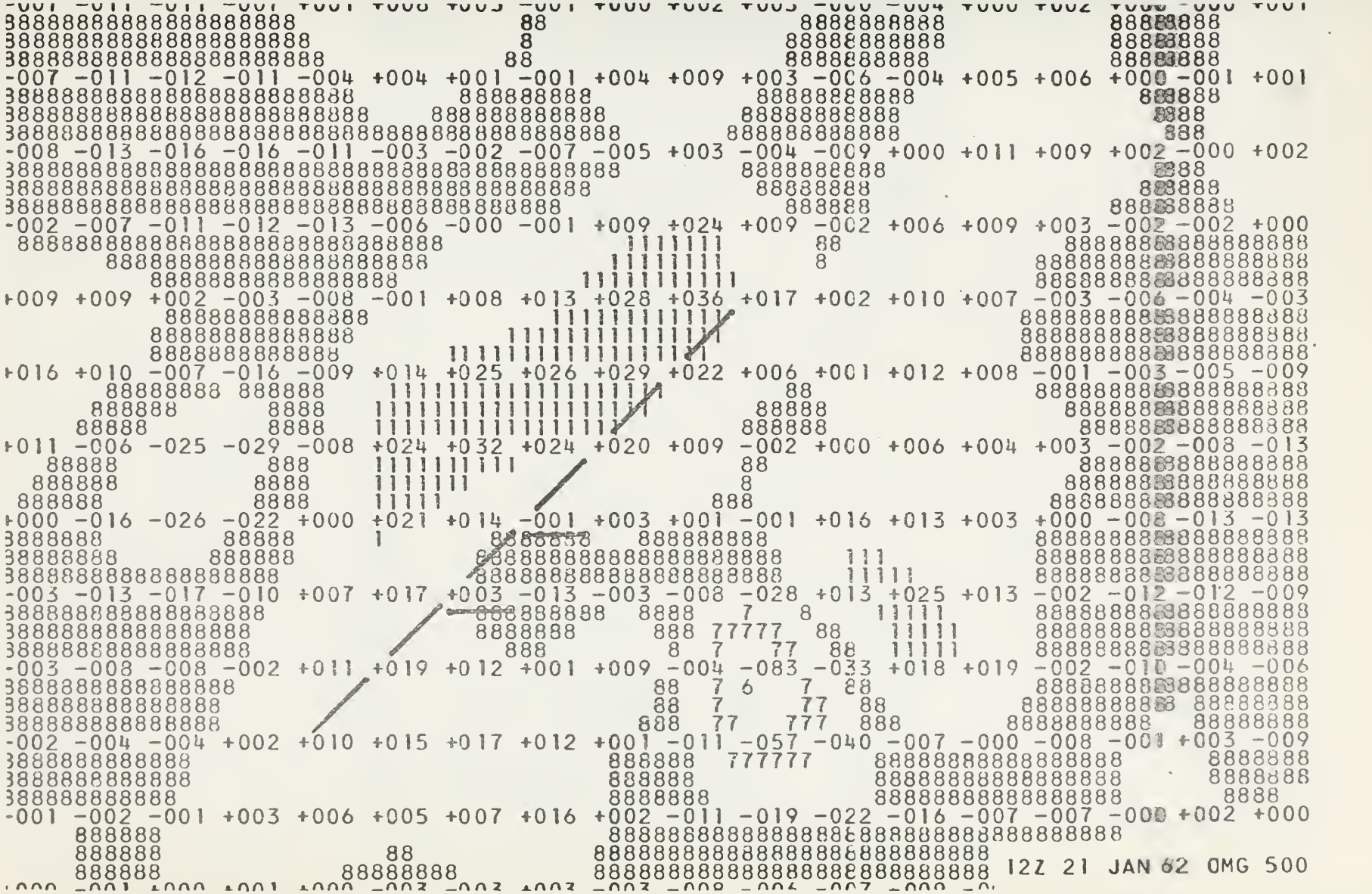
12Z 21 JAN 62 OMG 500

12Z 21 JAN 62 RV 300

12Z 21 JAN 82 OMG 300

00Z 22 JAN 62 OMEGALO

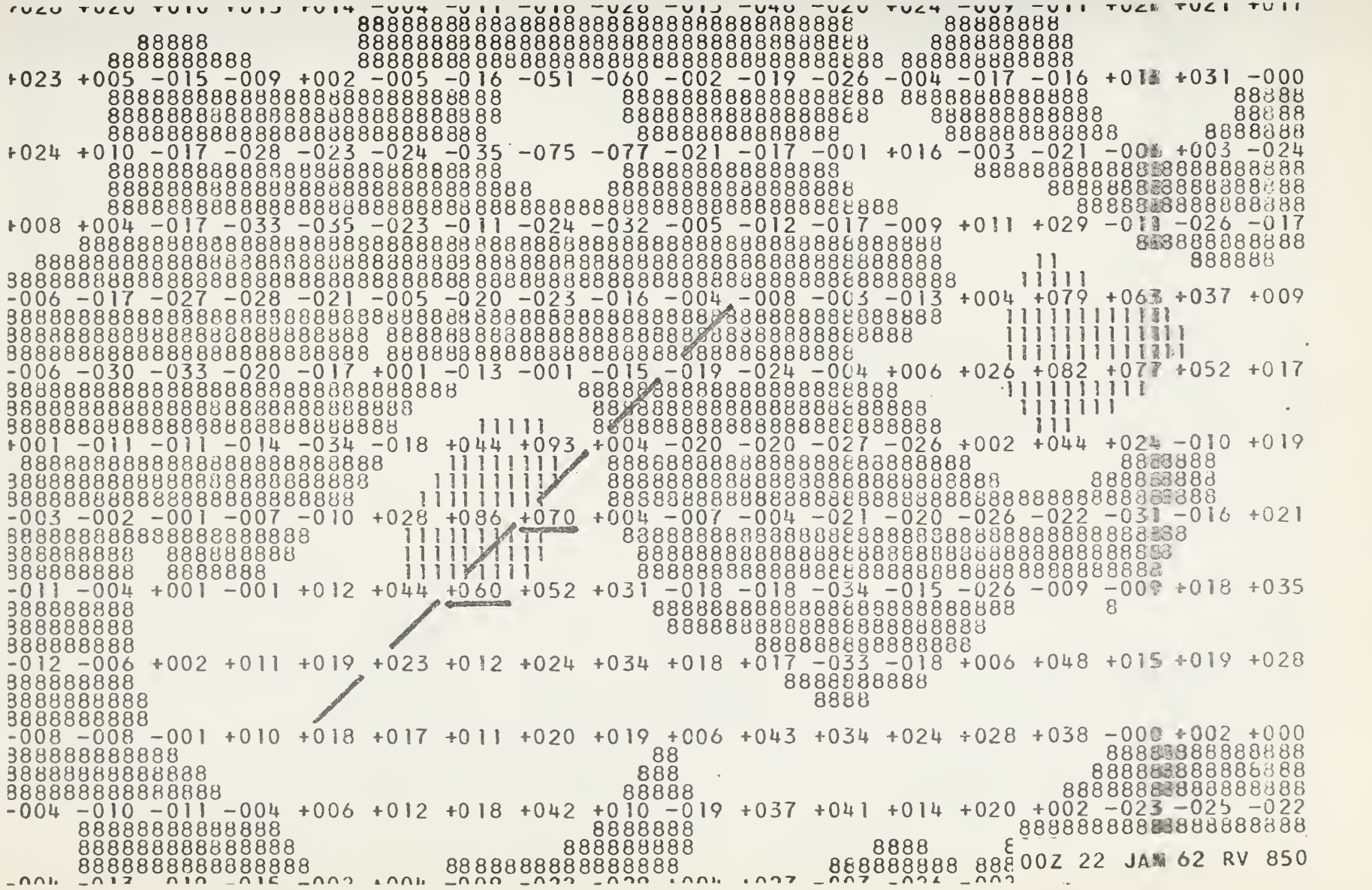
+023 +005 -015 -009 +002 -005 -016 -051 -060 -002 -019 -026 -004 -017 -016 +031 -000
+024 +010 -017 -028 -023 -024 -035 -075 -077 -021 -017 -001 +016 -003 -021 +003 -024
+008 +004 -017 -033 -035 -023 -011 -024 -032 -005 -012 -017 -009 +011 +029 -026 -017
-006 -017 -027 -028 -021 -005 -020 -023 -016 -004 -008 -003 -013 +004 +079 +063 +037 +009
-006 -030 -033 -020 -017 +001 -013 -001 -015 -019 -024 -004 +006 +026 +082 +077 +052 +017
+001 -011 -011 -014 -034 -018 +044 +093 +004 -020 -020 -027 -026 +002 +044 +024 -010 +019
-003 -002 -001 -007 -010 +028 +086 +070 +004 -007 -004 -021 -020 -026 -022 -031 -016 +021
-011 -004 +001 -001 +012 +044 +060 +052 +031 -018 -018 -034 -015 -026 -009 -009 +018 +035
-012 -006 +002 +011 +019 +023 +012 +024 +034 +018 +017 -033 -018 +006 +048 +015 +019 +028
-008 -008 -001 +010 +018 +017 +011 +020 +019 +006 +043 +034 +024 +028 +038 -000 +002 +000
-004 -010 -011 -004 +006 +012 +018 +042 +010 -019 +037 +041 +014 +020 +002 -023 -025 -022
00Z 22 JAN 62 RV 850

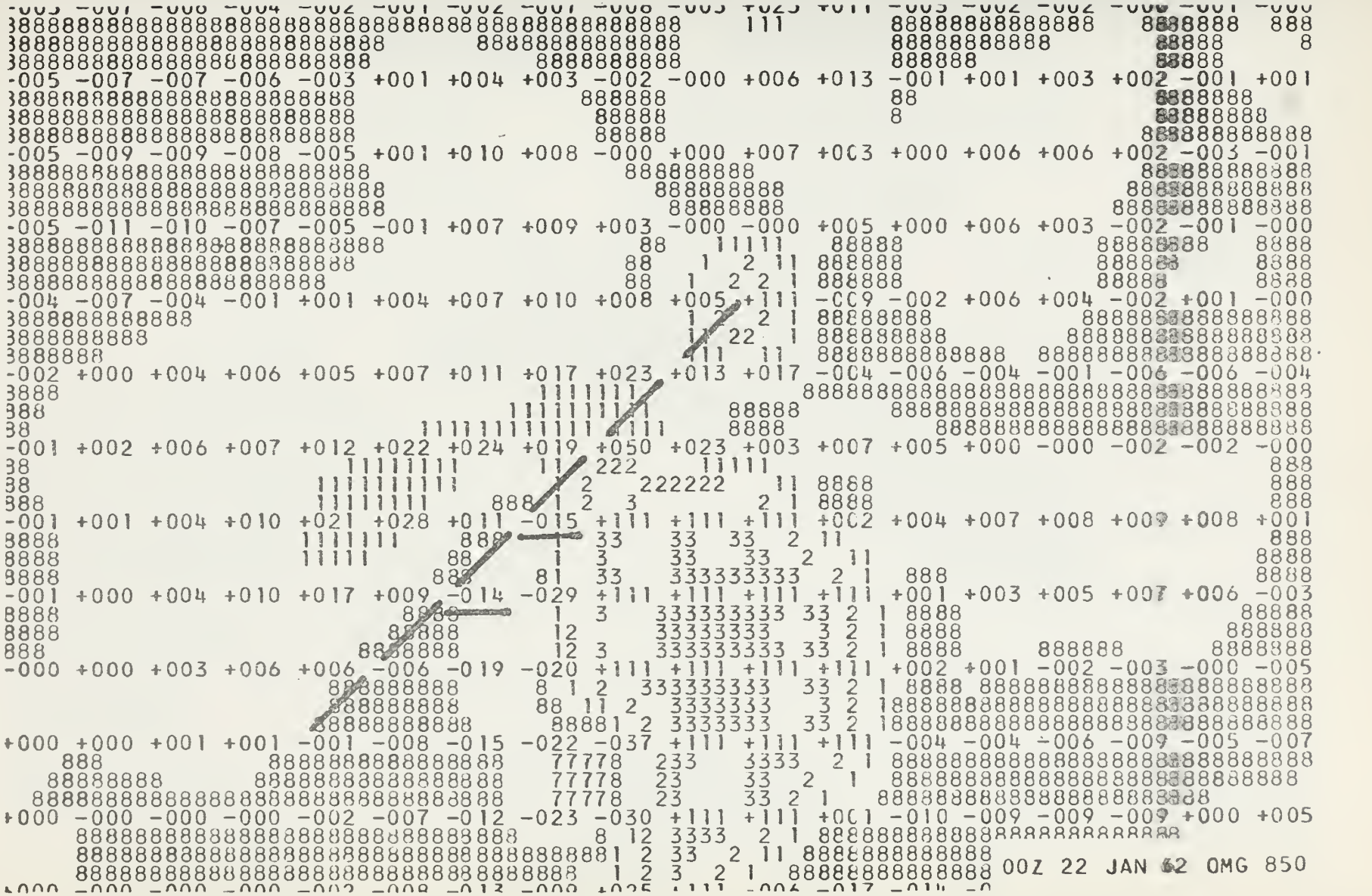
00Z 22 JAN 82 OMG 850

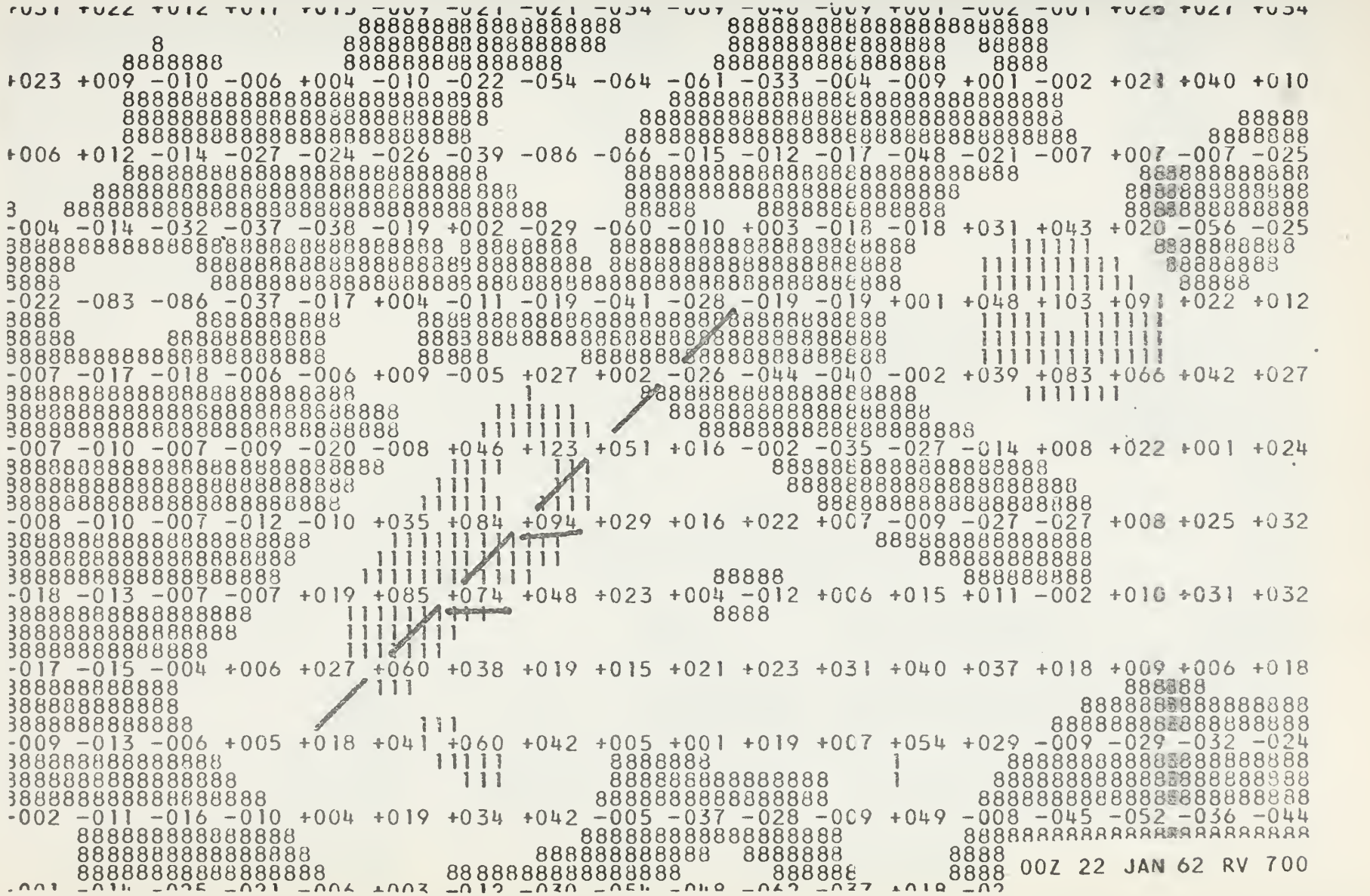
00Z 22 JAN 62 RV 700

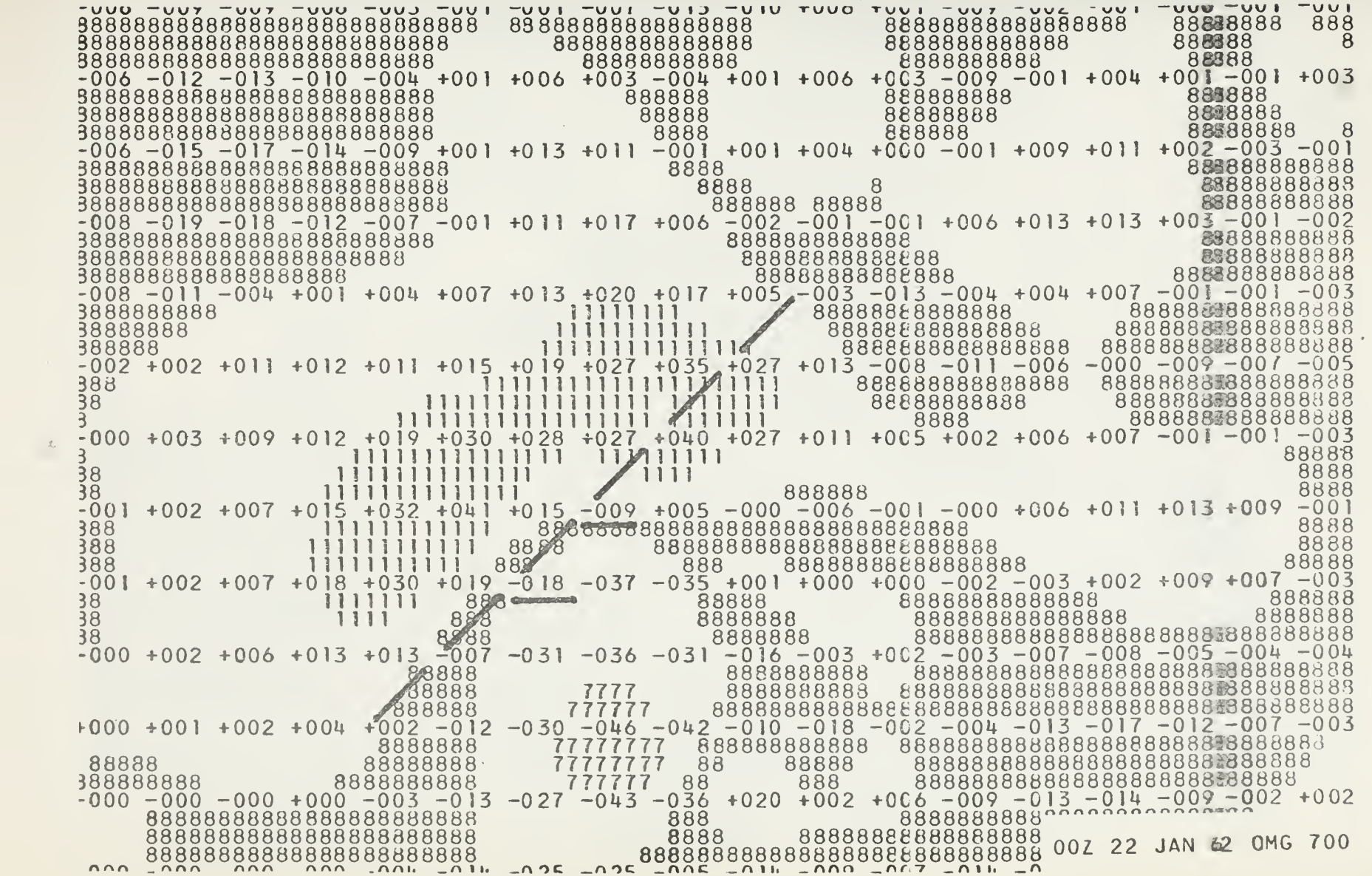
00Z 22 JAN 62 OMG 700

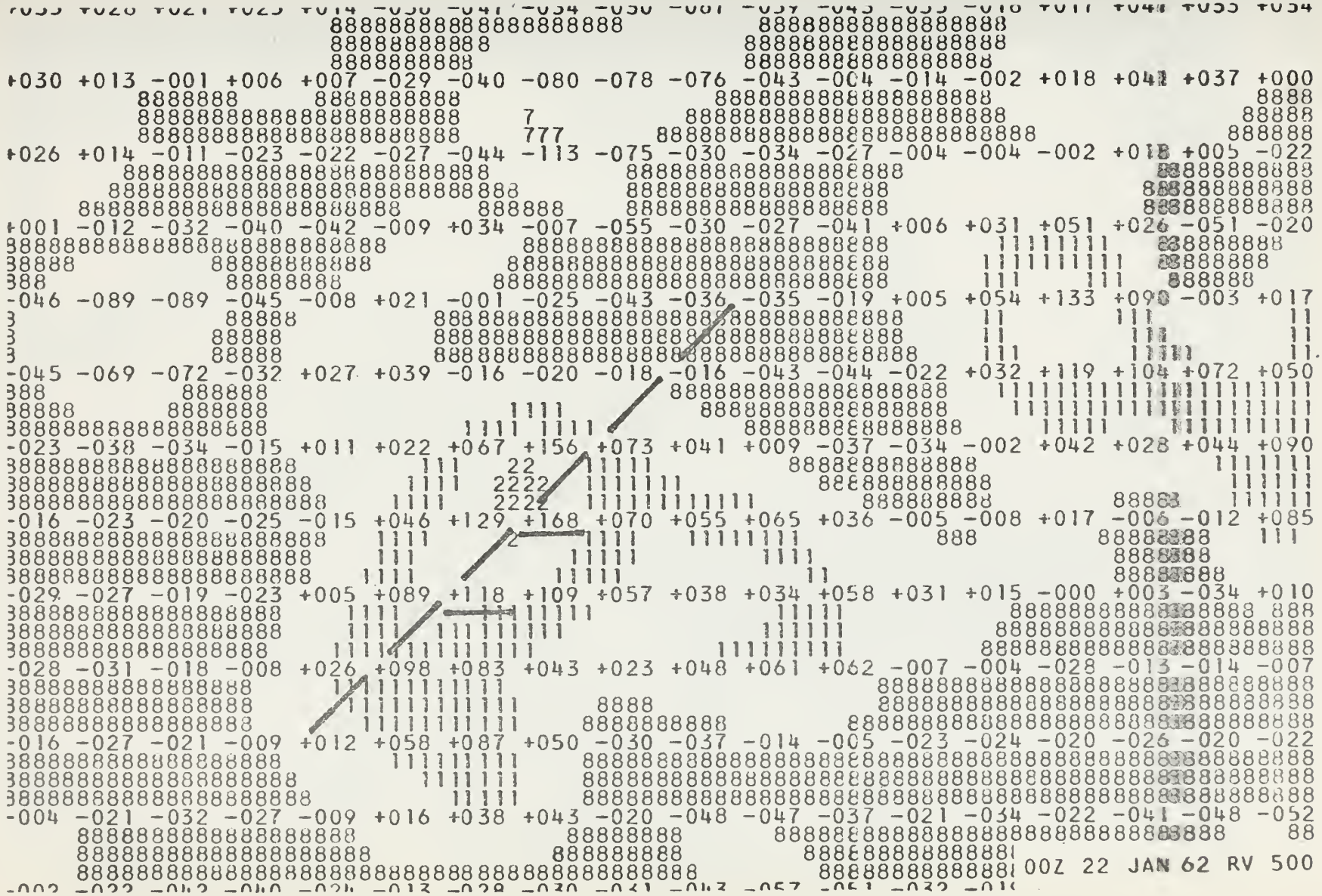
00Z 22 JAN 62 RV 500

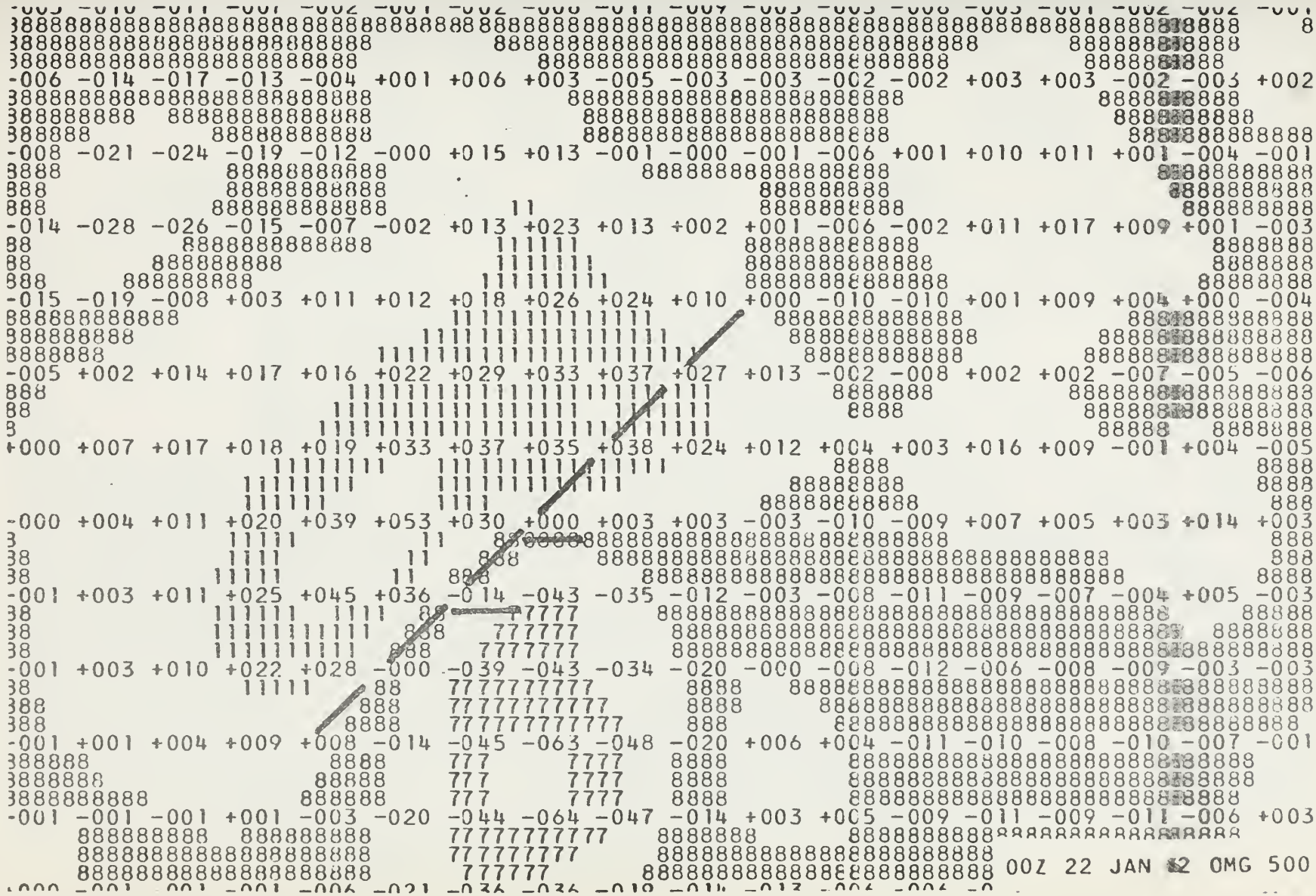
00Z 22 JAN 82 OMG 500

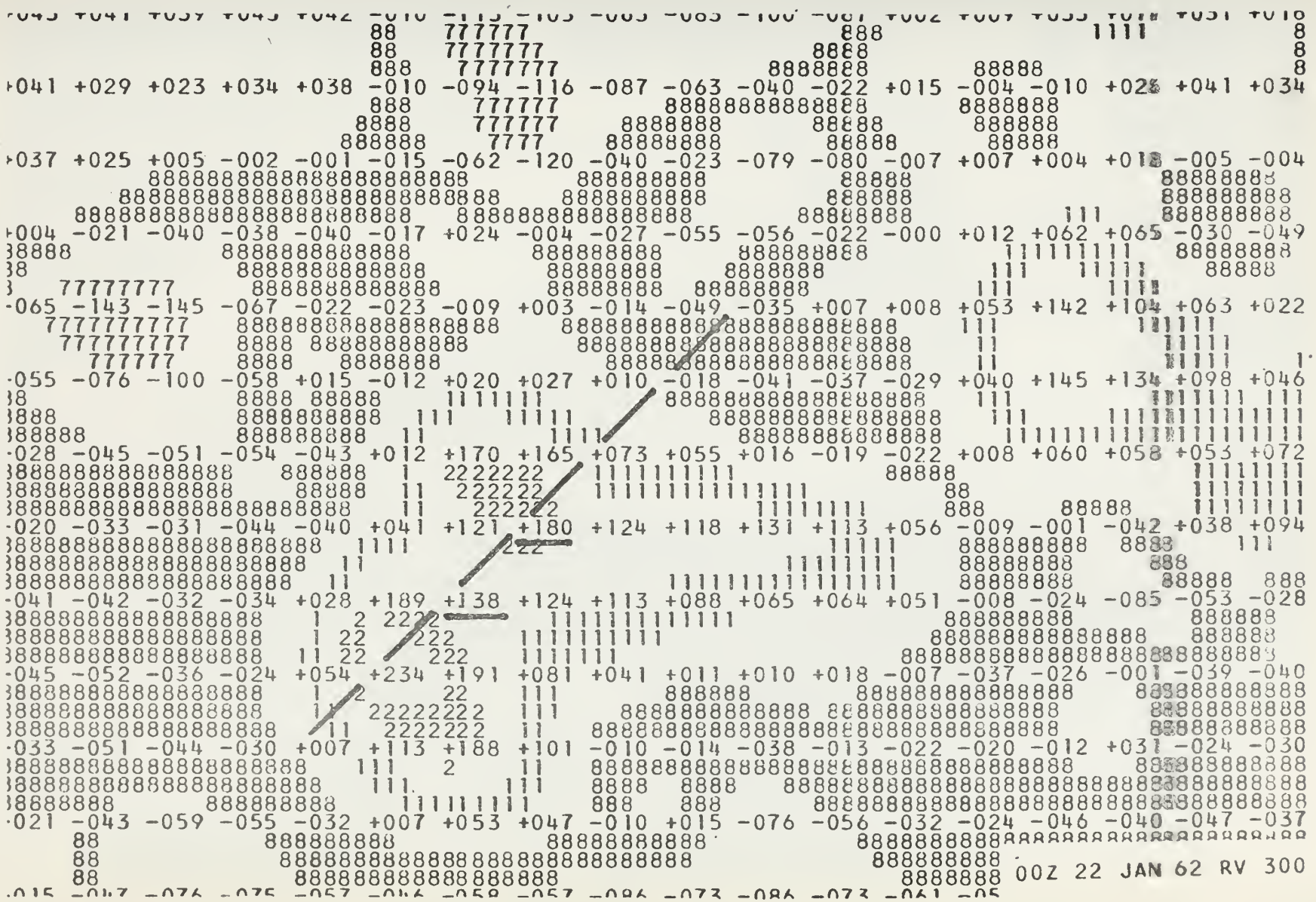
00Z 22 JAN 62 RV 300

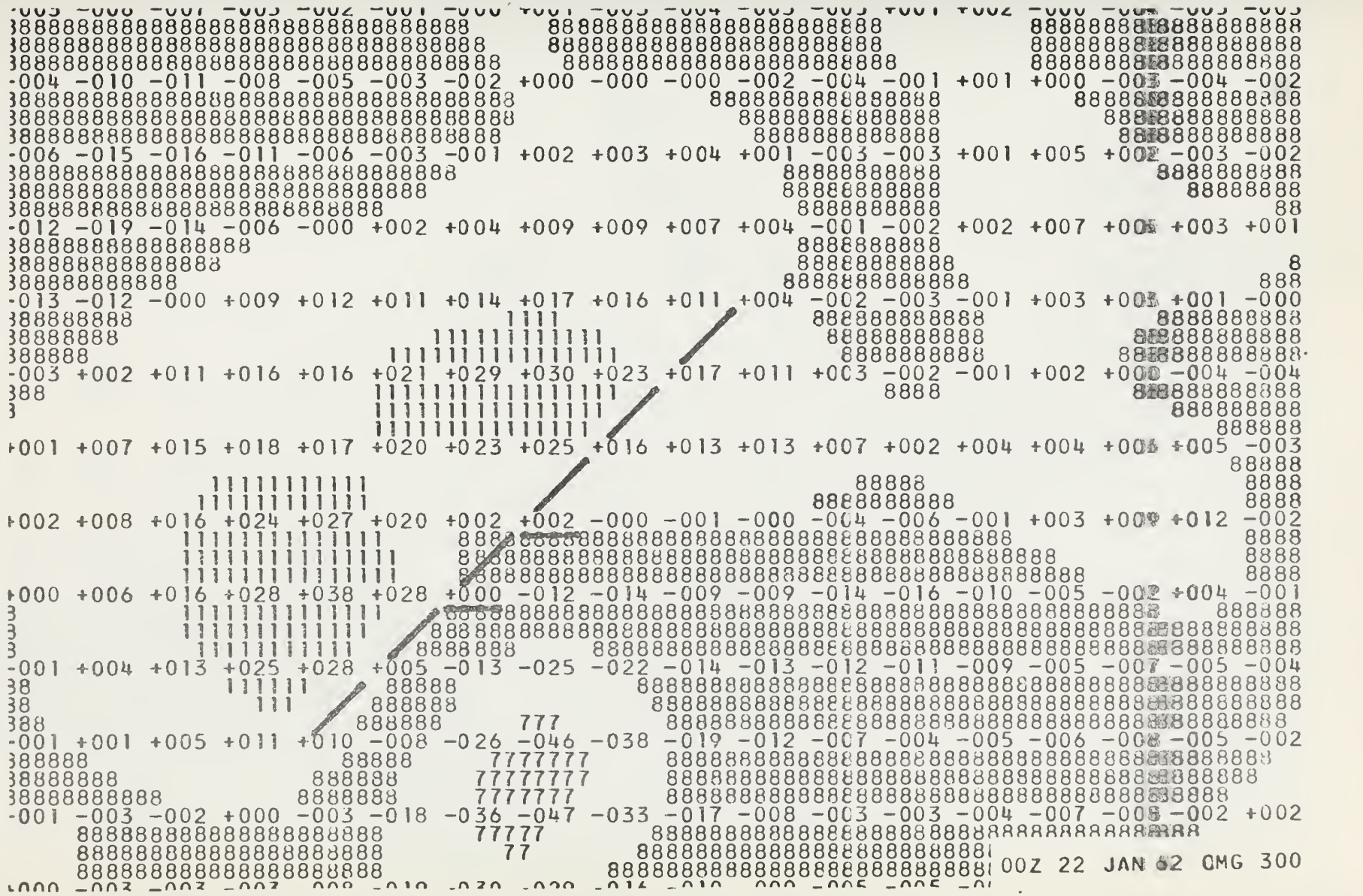
00Z 22 JAN 82 OMG 300

12Z 22 JAN 62 OMEGALO

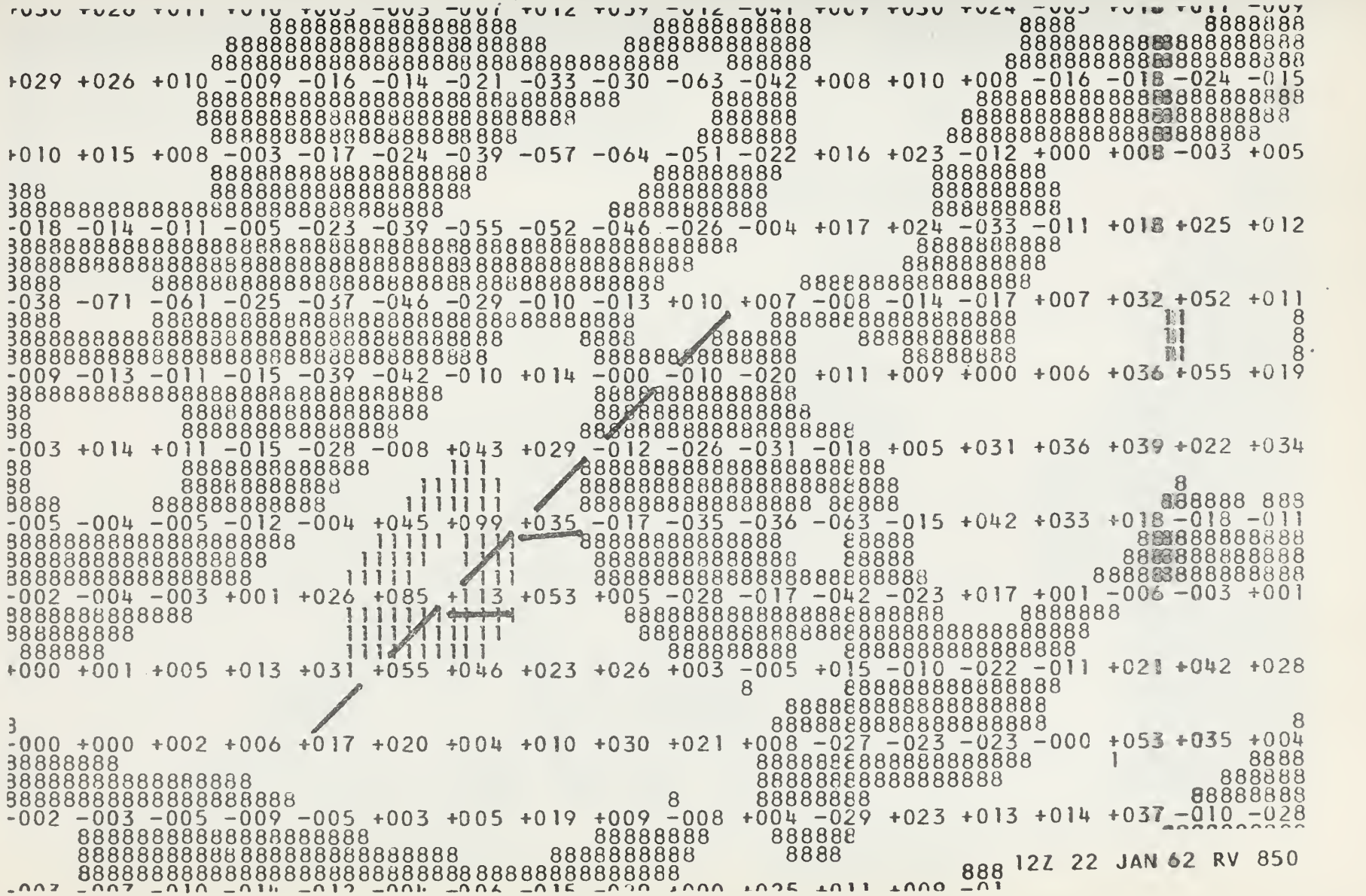
12Z 22 JAN 62 RV 850

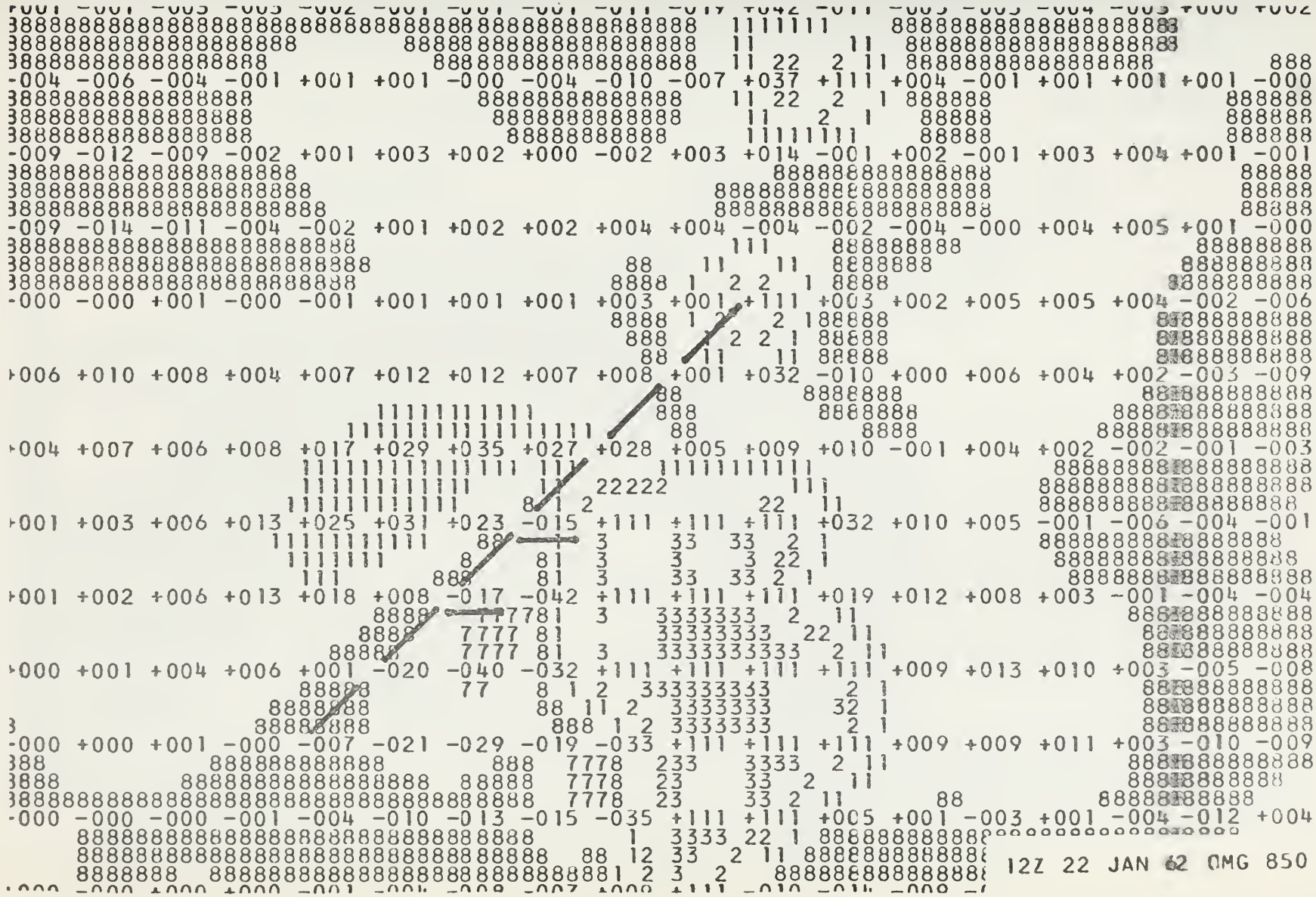
12Z 22 JAN 62 OMG 850

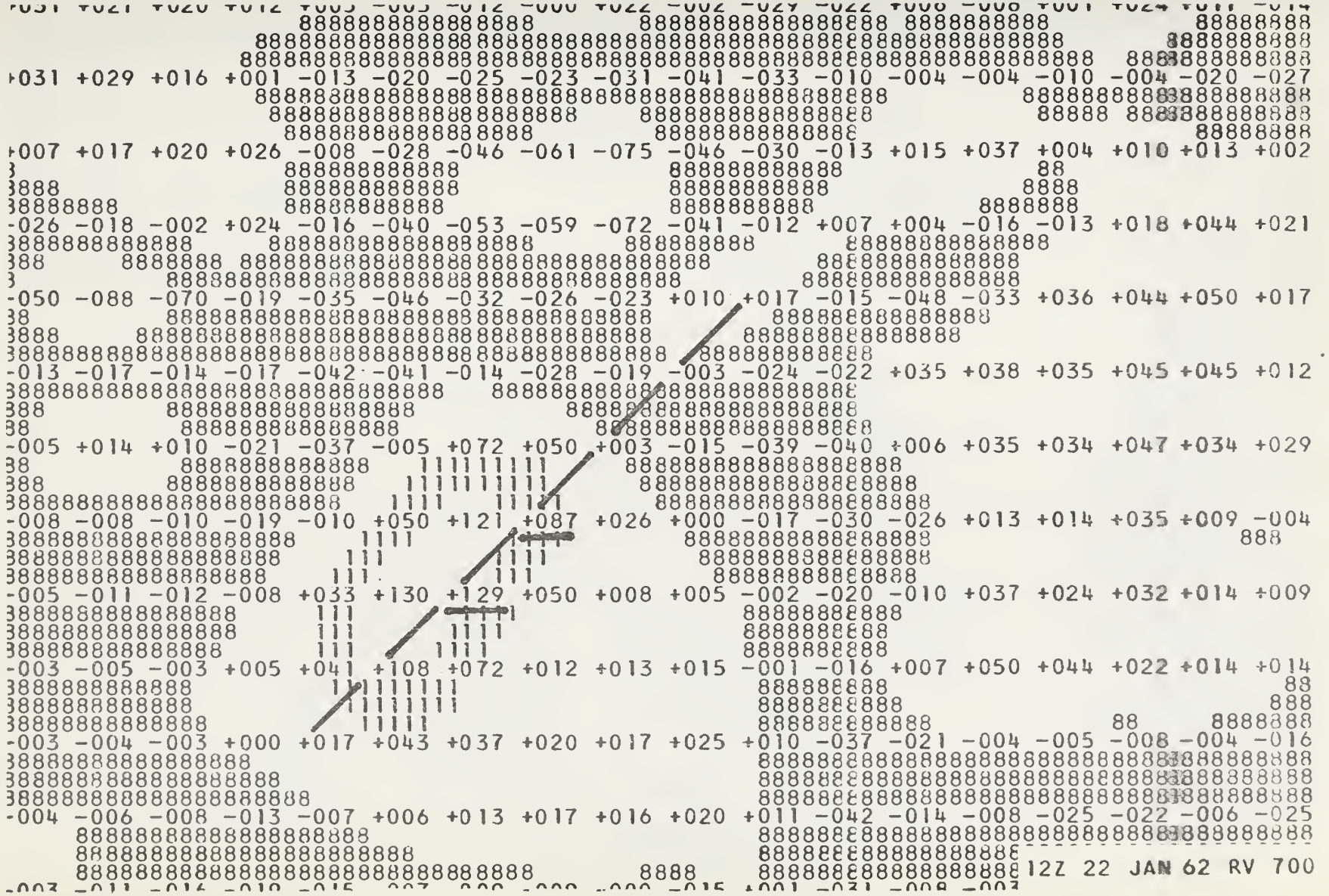
12Z 22 JAN 62 RV 700

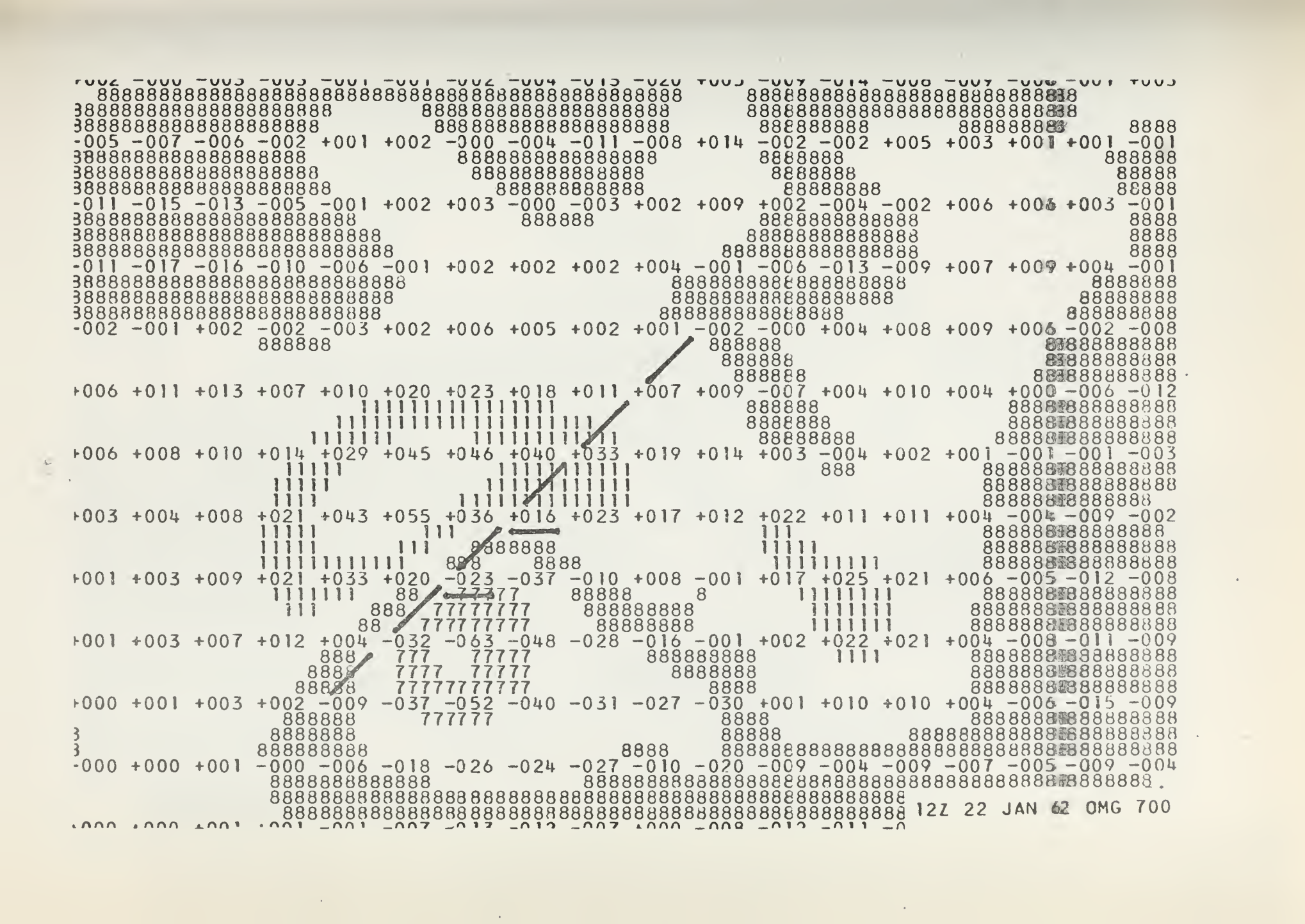
12Z 22 JAN 62 OMG 700

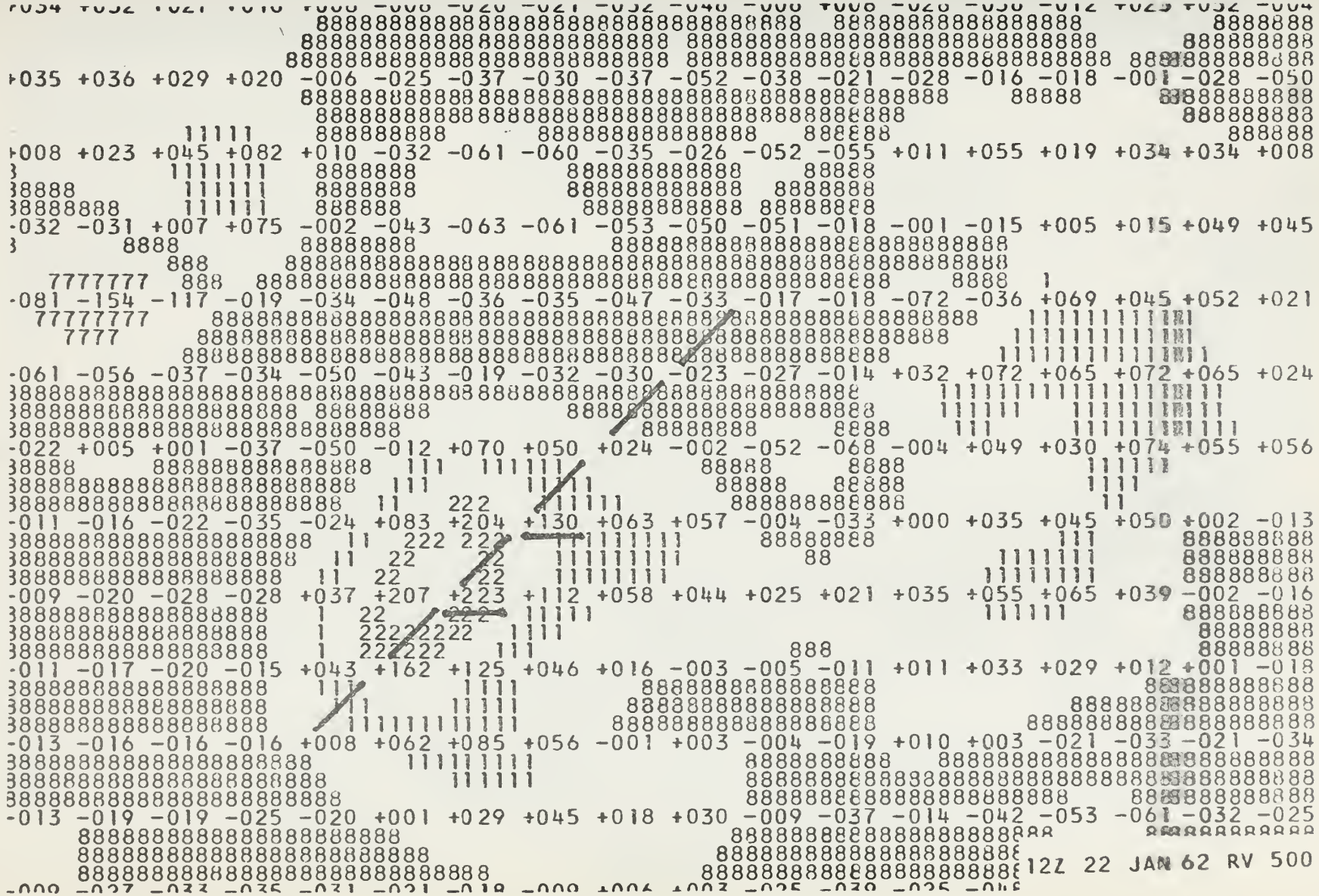
12Z 22 JAN 62 RV 500

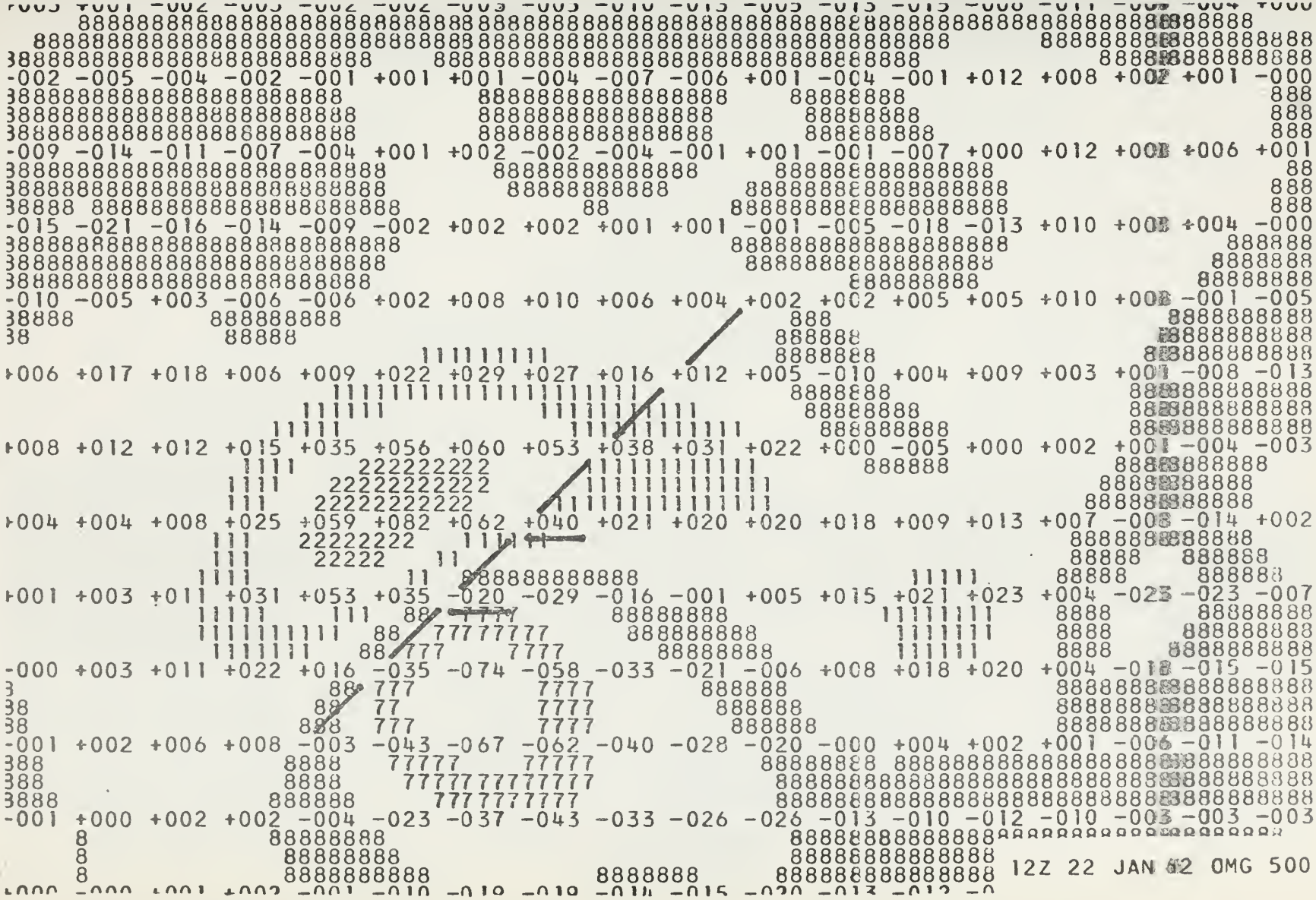
12Z 22 JAN 82 OMG 500

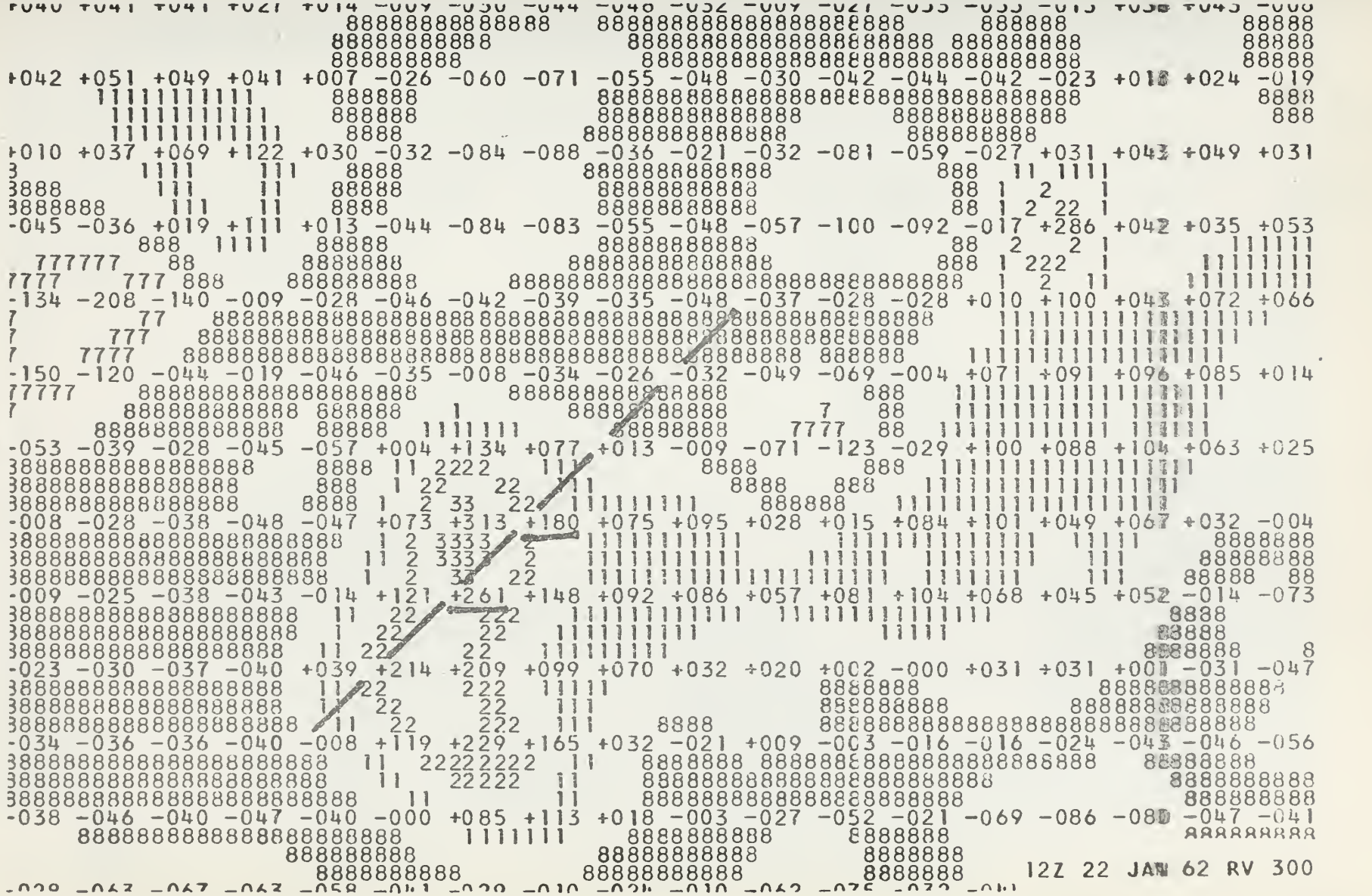
12Z 22 JAN 62 RV 300

00Z 21 JAN 62 T 500

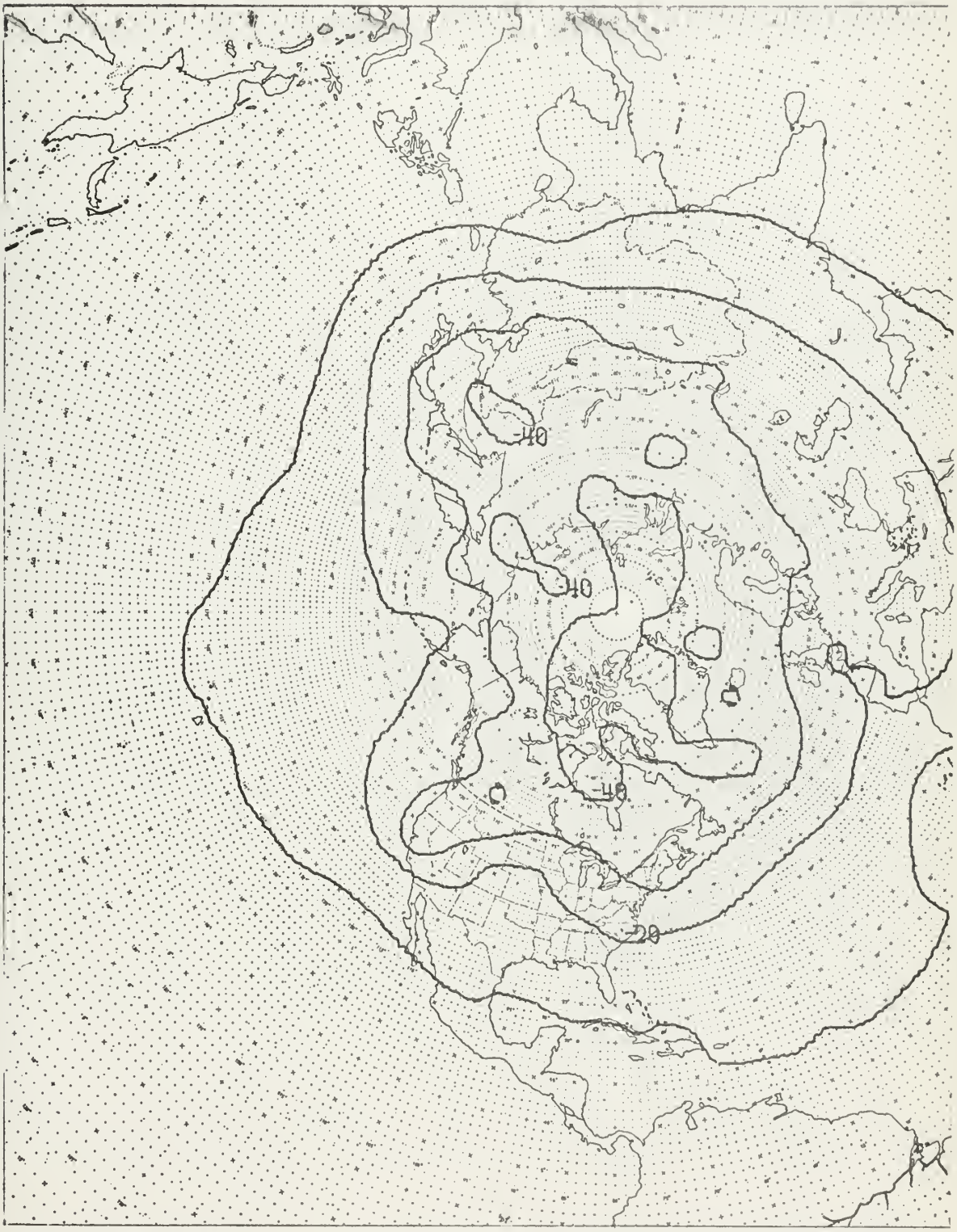

SCALE: 1:120,000,000

FLEET NUMERICAL WEATHER FACILITY, MONTEREY, CALIFORNIA

00Z 21 JAN 62 D 300

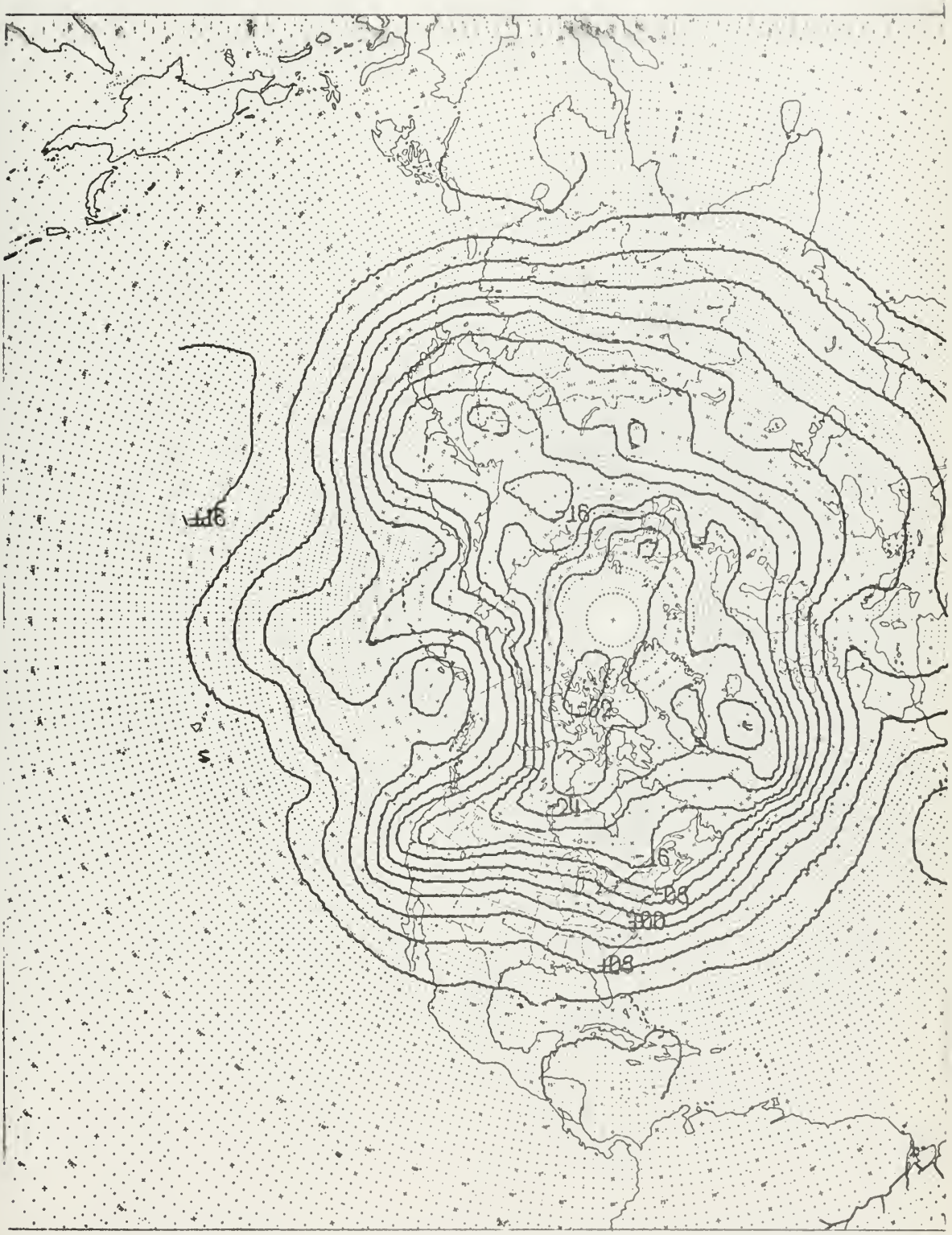

SCALE: 1:120,000,000

FLEET NUMERICAL WEATHER FACILITY, MONTEREY, CALIFORNIA

00Z 21 JAN 62 T 300

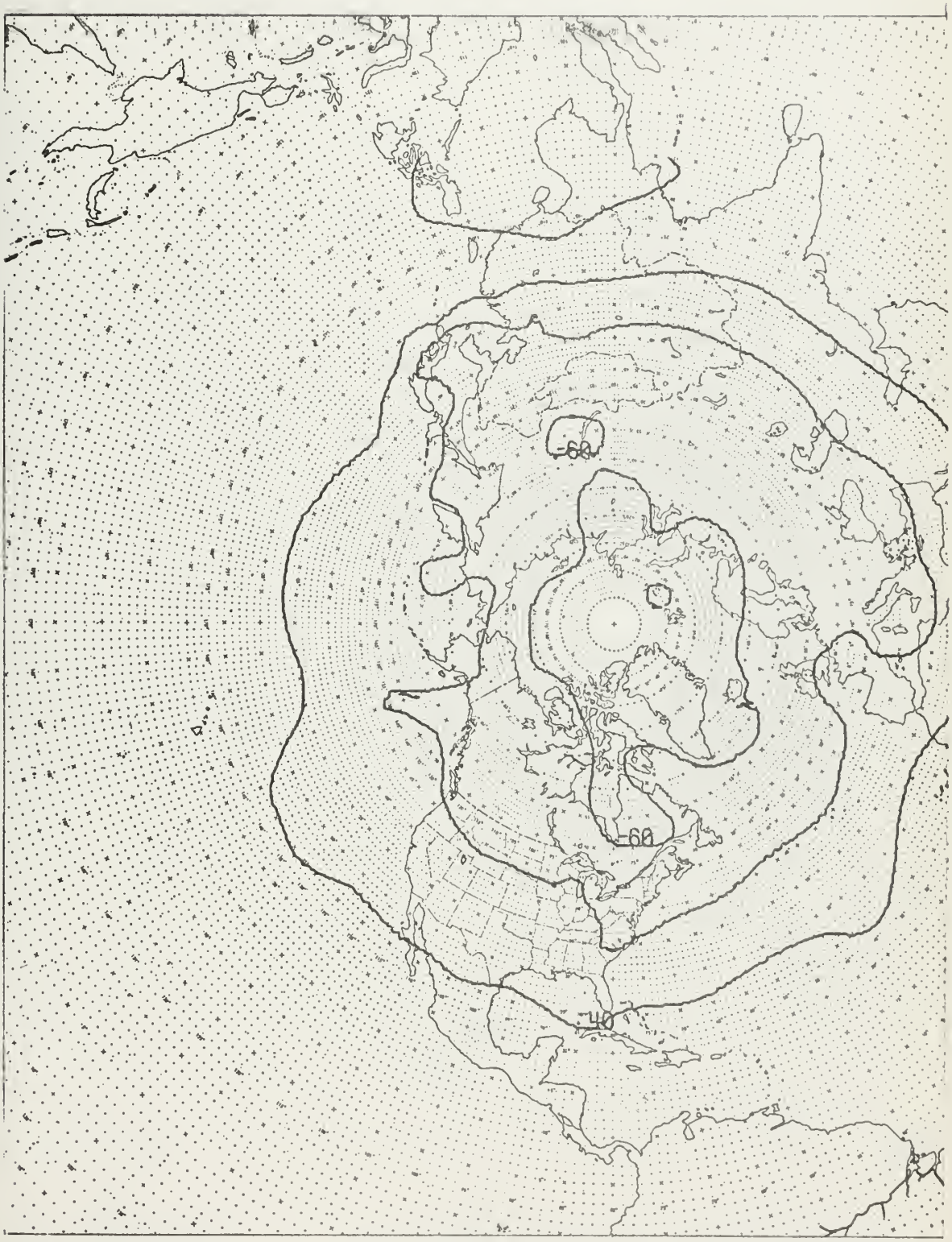

SCALE: 1:120,000,000

FLEET NUMERICAL WEATHER FACILITY, MONTEREY, CALIFORNIA

00Z 22 JAN 62 D 1000

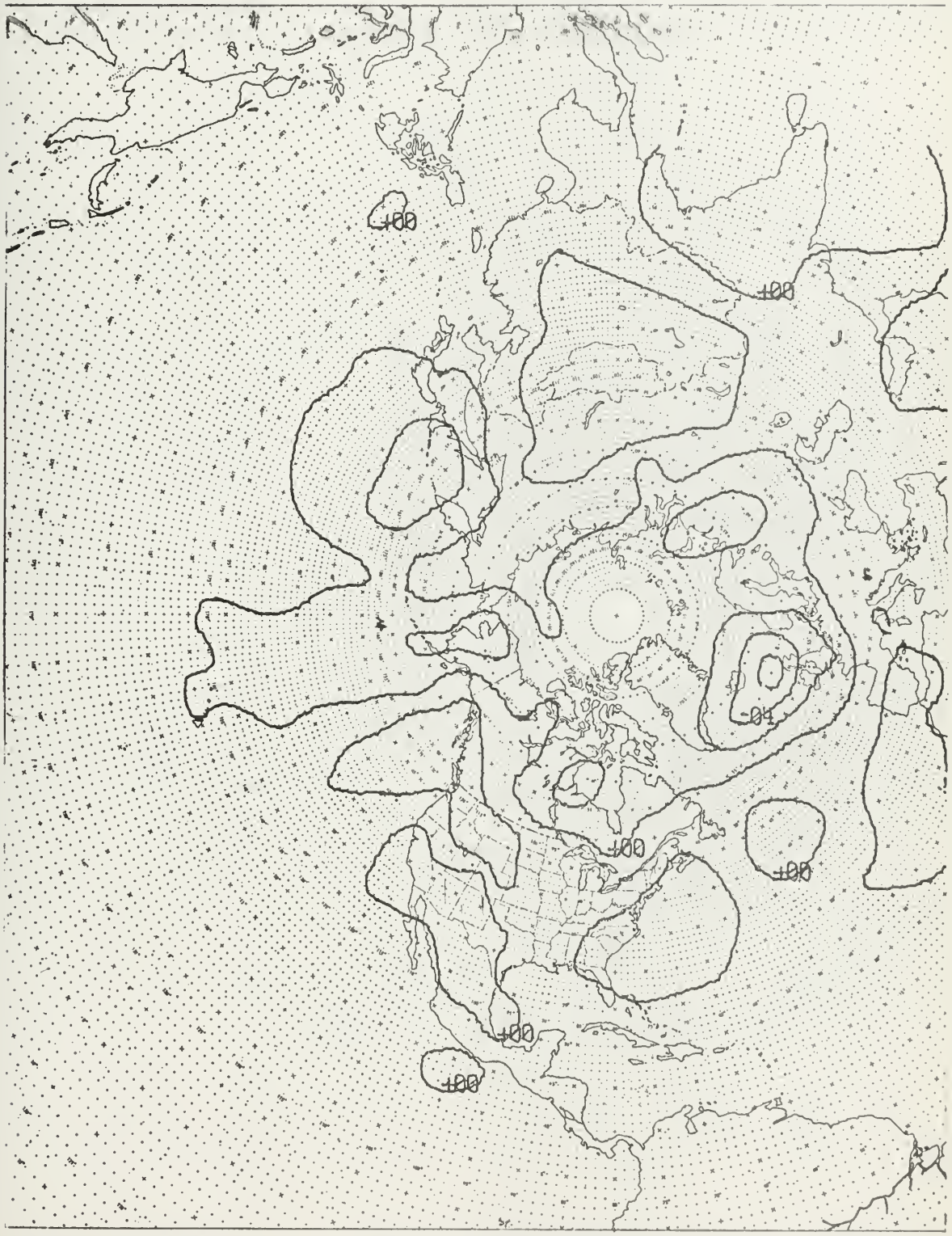

SCALE: 1:120,000,000

FLEET NUMERICAL WEATHER FACILITY, MONTEREY, CALIFORNIA

00Z 22 JAN 62 T 1000

SCALE: 1:120,000,000

FLEET NUMERICAL WEATHER FACILITY, MONTEREY, CALIFORNIA

00Z 22 JAN 62 D 850

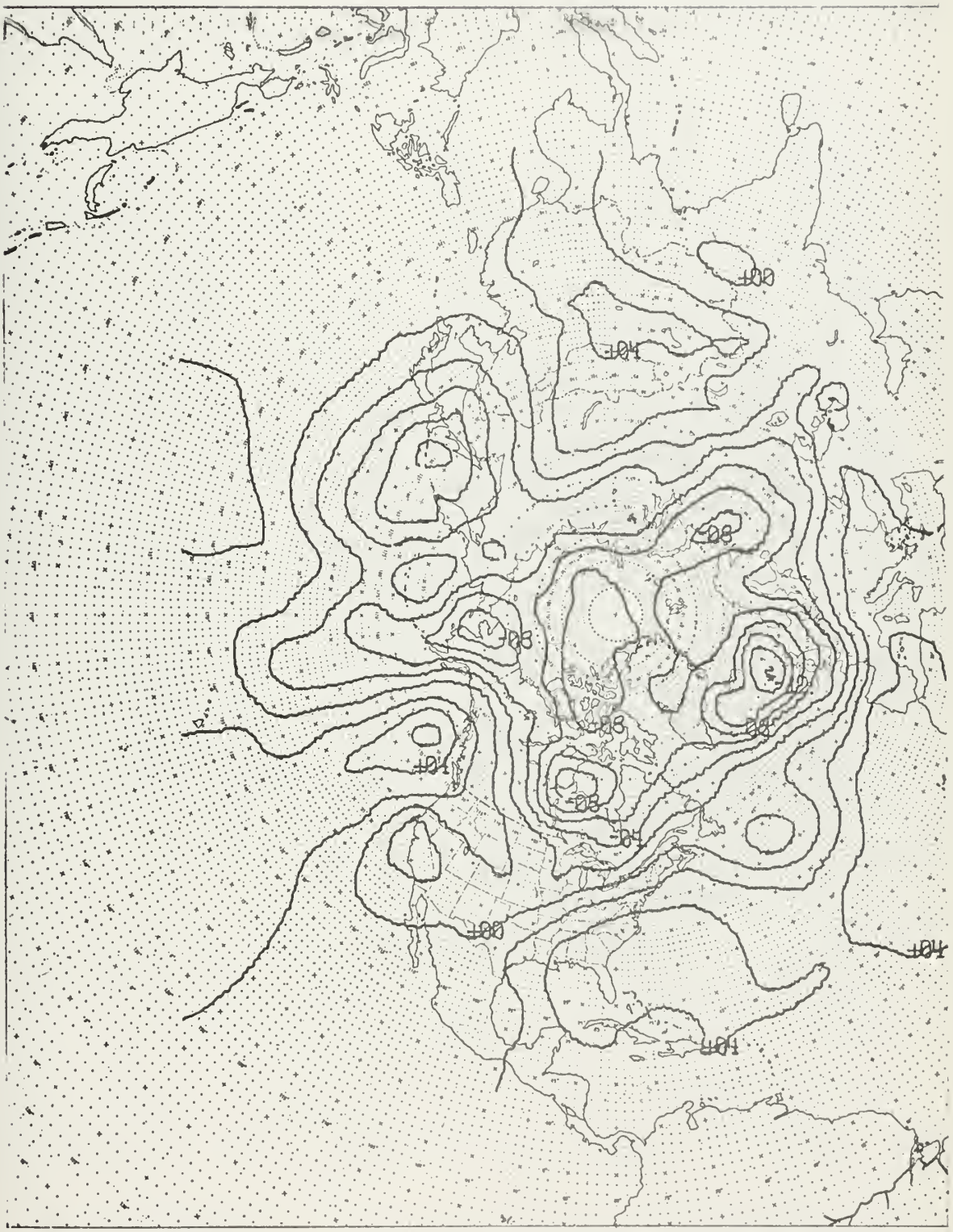

SCALE: 1:120,000,000

FLEET NUMERICAL WEATHER FACILITY, MONTEREY, CALIFORNIA

00Z 22 JAN 62 T 850

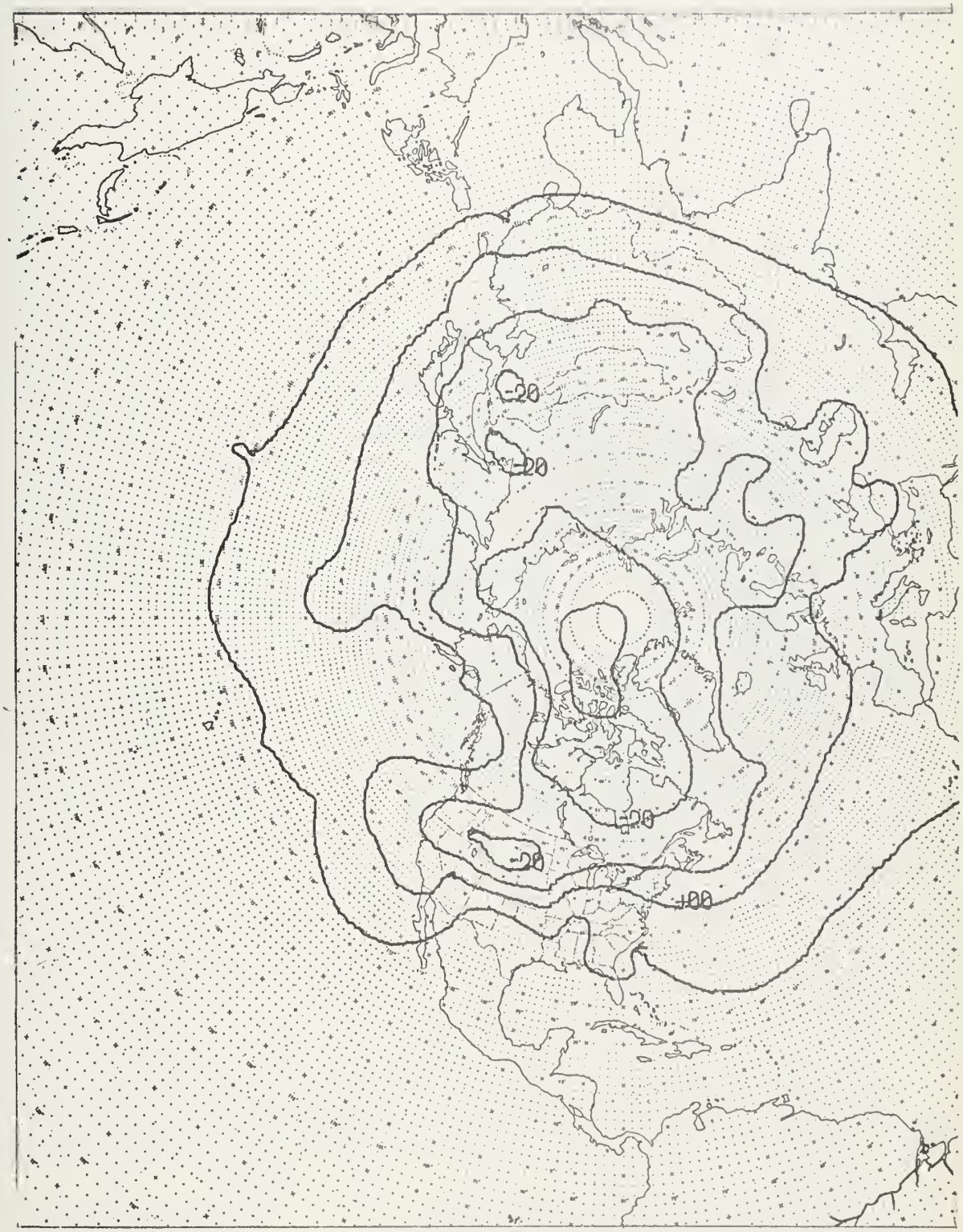

SCALE: 1:120,000,000

FLEET NUMERICAL WEATHER FACILITY, MONTEREY, CALIFORNIA

00Z 22 JAN 62 SIG 850

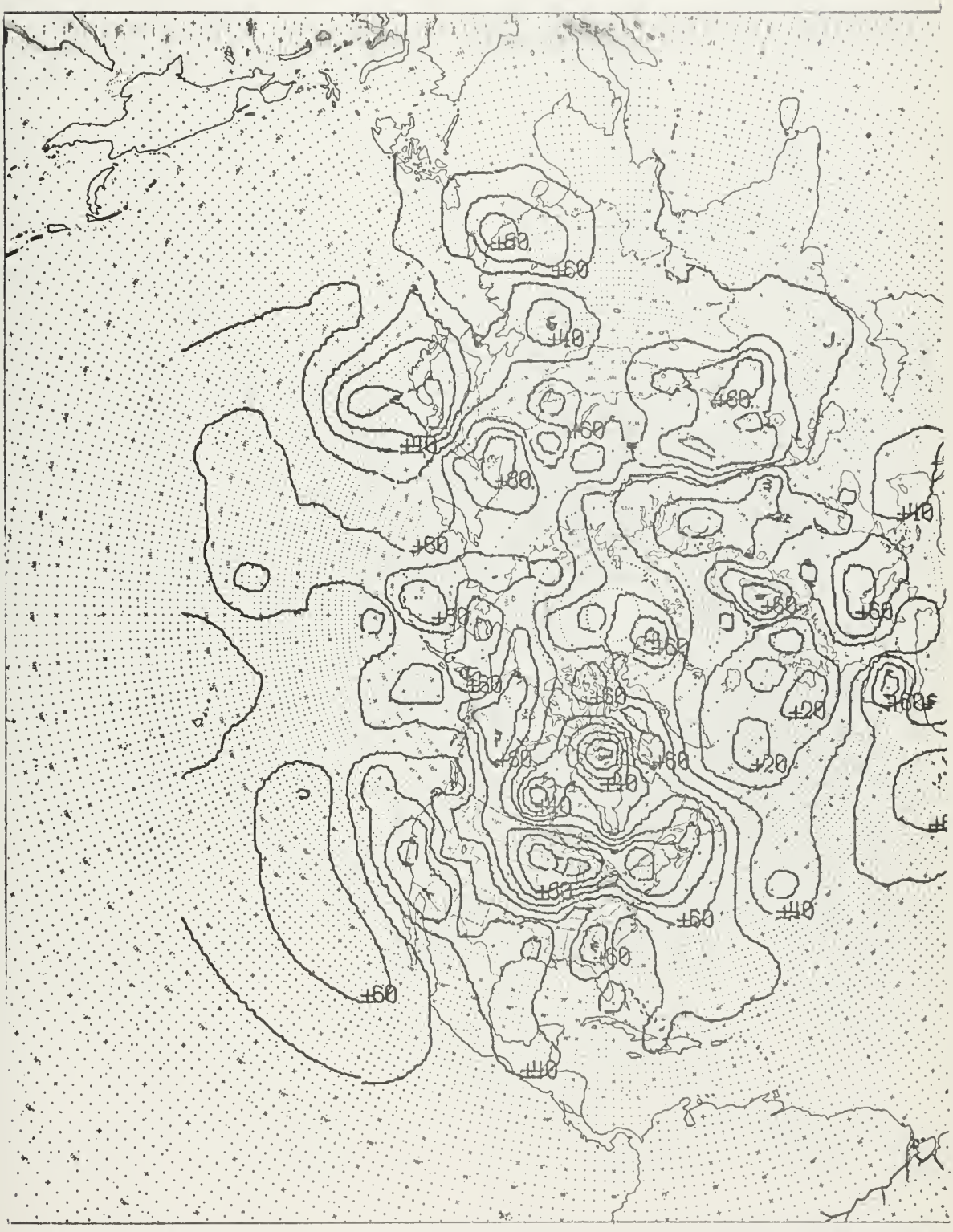

SCALE: 1:120,000,000

FLEET NUMERICAL WEATHER FACILITY, MONTEREY, CALIFORNIA

00Z 22 JAN 62 D 700

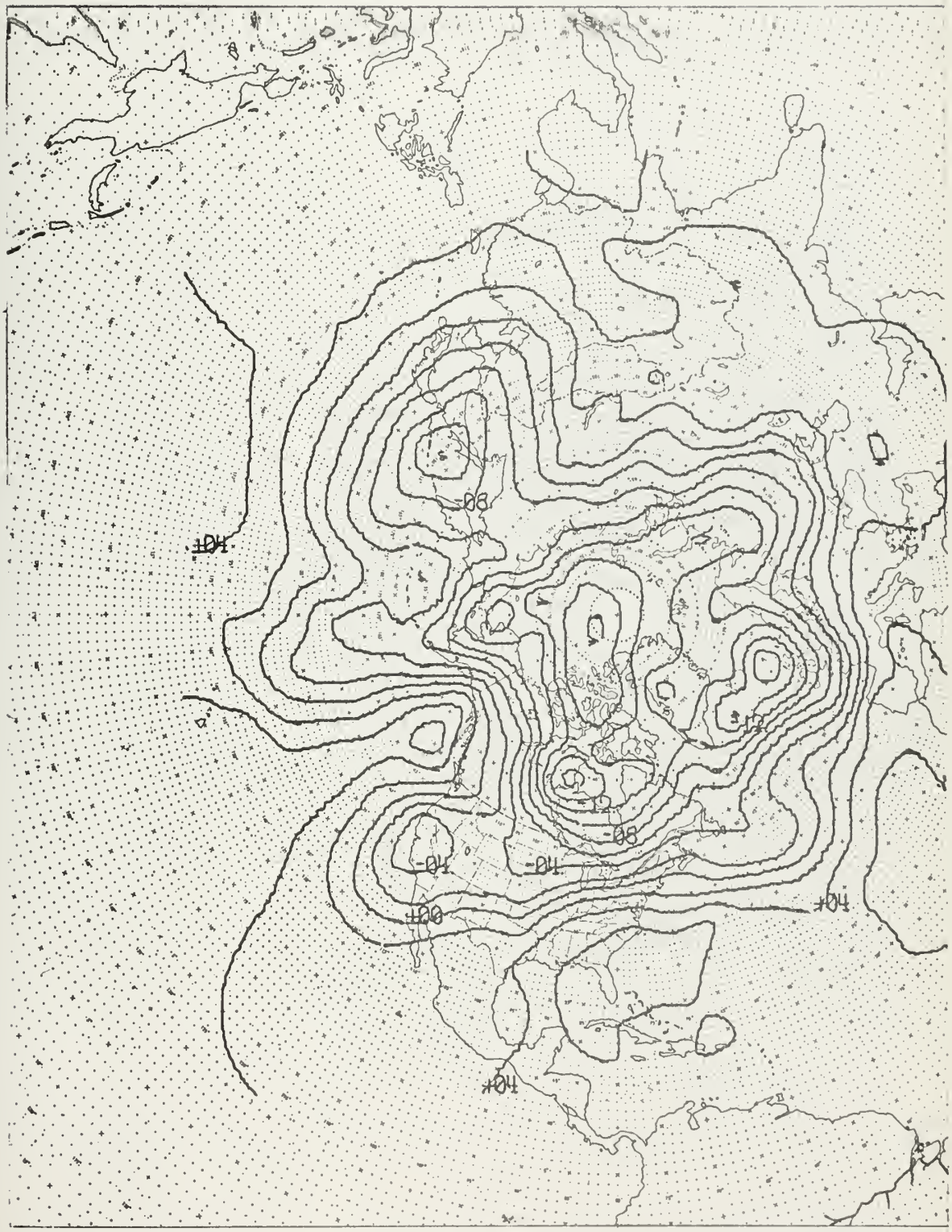

SCALE: 1:120,000,000

FLEET NUMERICAL WEATHER FACILITY, MONTEREY, CALIFORNIA

00Z 22 JAN 62 T 700

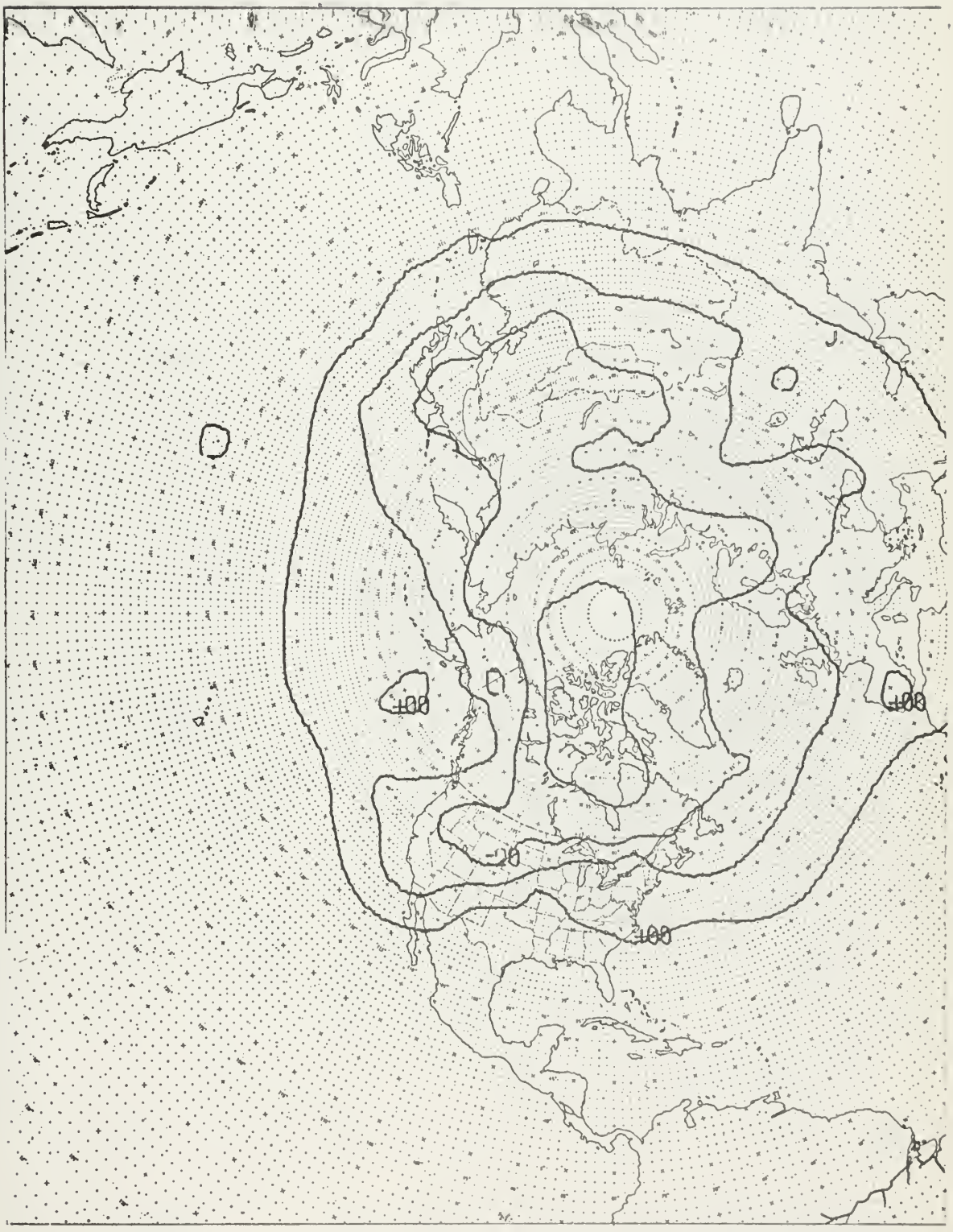

SCALE: 1:120,000,000

FLEET NUMERICAL WEATHER FACILITY, MONTEREY, CALIFORNIA

00Z 22 JAN 62 SIG 700

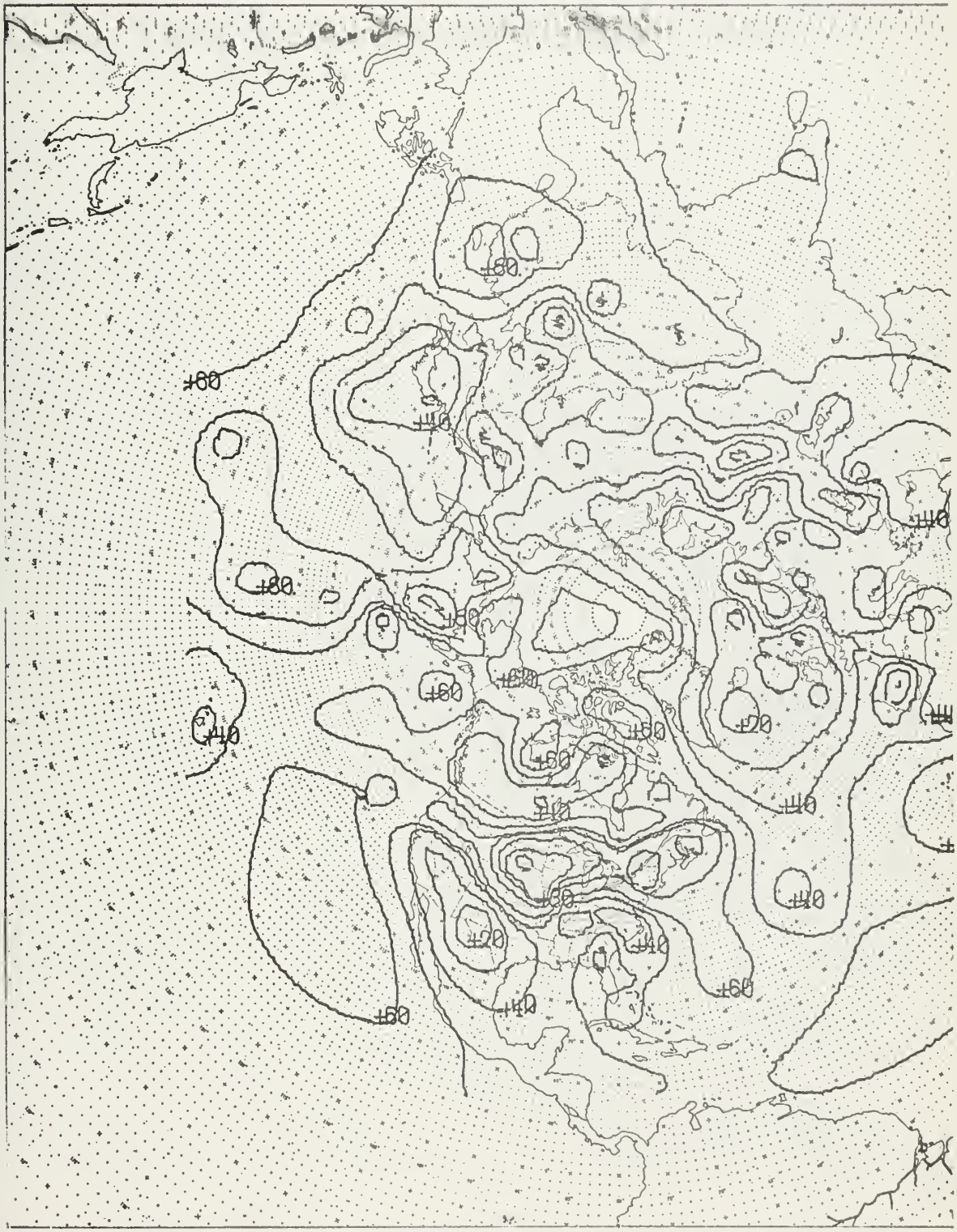

SCALE: 1:120,000,000

FLEET NUMERICAL WEATHER FACILITY, MONTEREY, CALIFORNIA

00Z 22 JAN 62 D 500

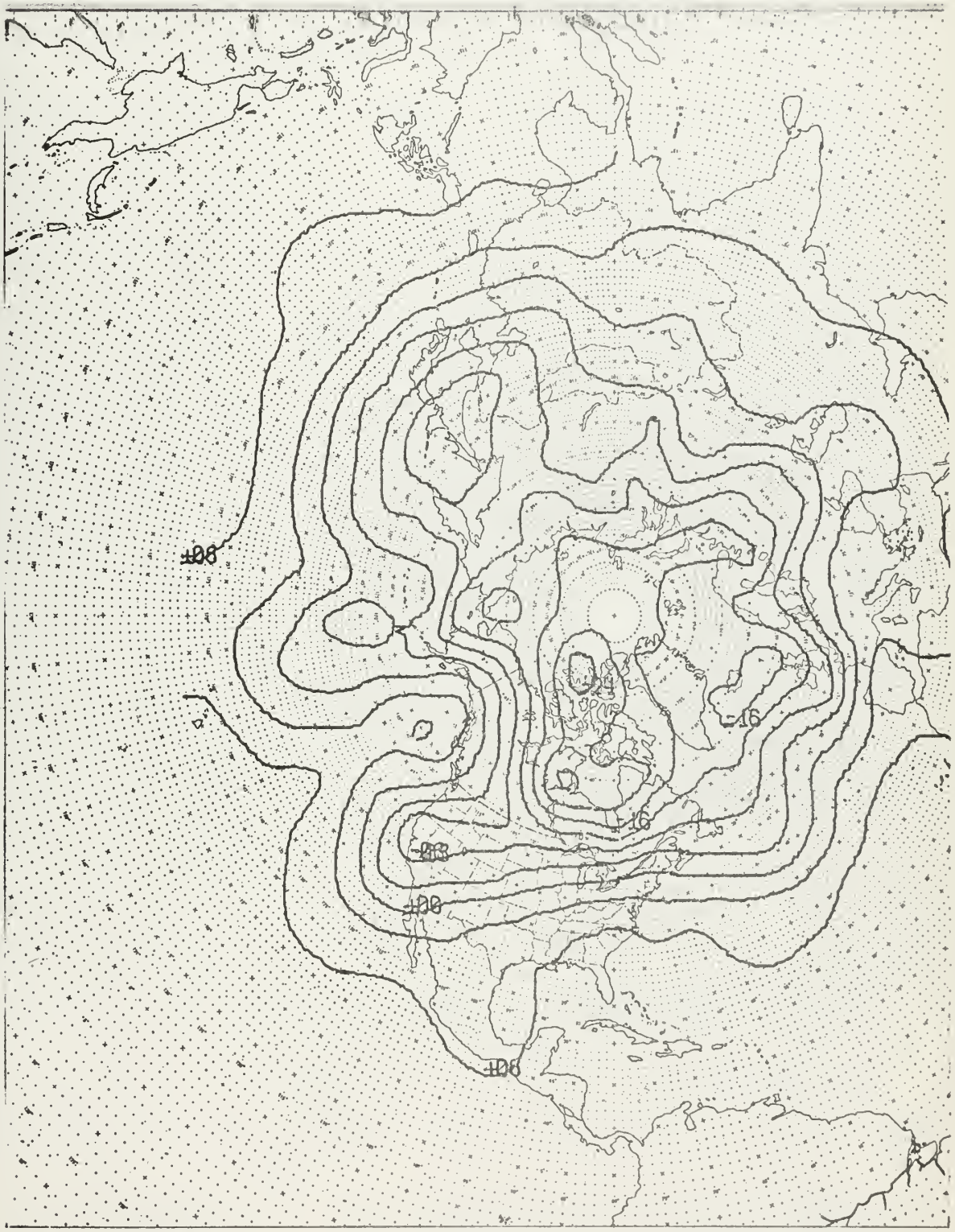

SCALE: 1:120,000,000

FLEET NUMERICAL WEATHER FACILITY, MONTEREY, CALIFORNIA

00Z 22 JAN 62 T 500

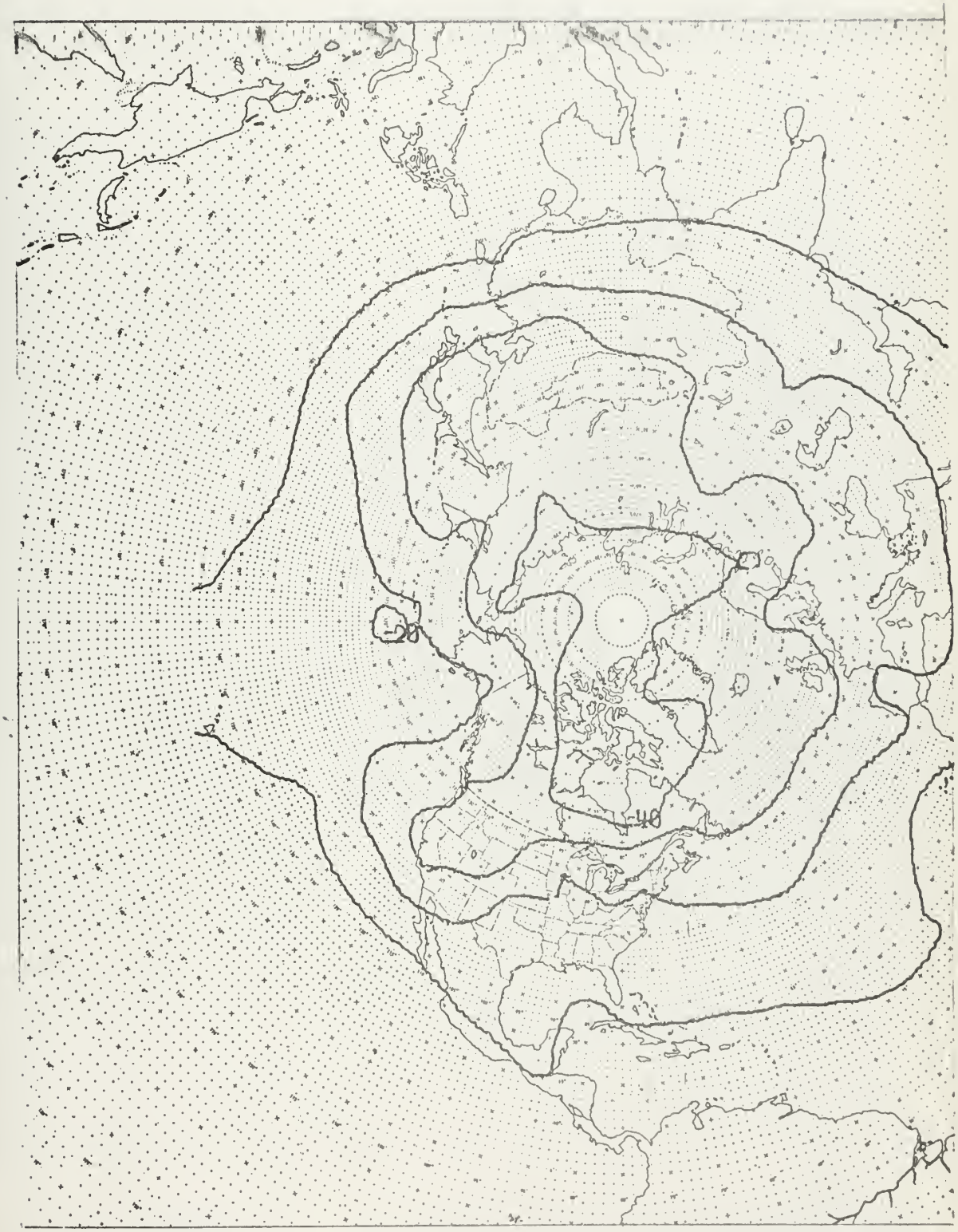

SCALE: 1:120,000,000

FLEET NUMERICAL WEATHER FACILITY, MONTEREY, CALIFORNIA

00Z 22 JAN 62 SIG 500

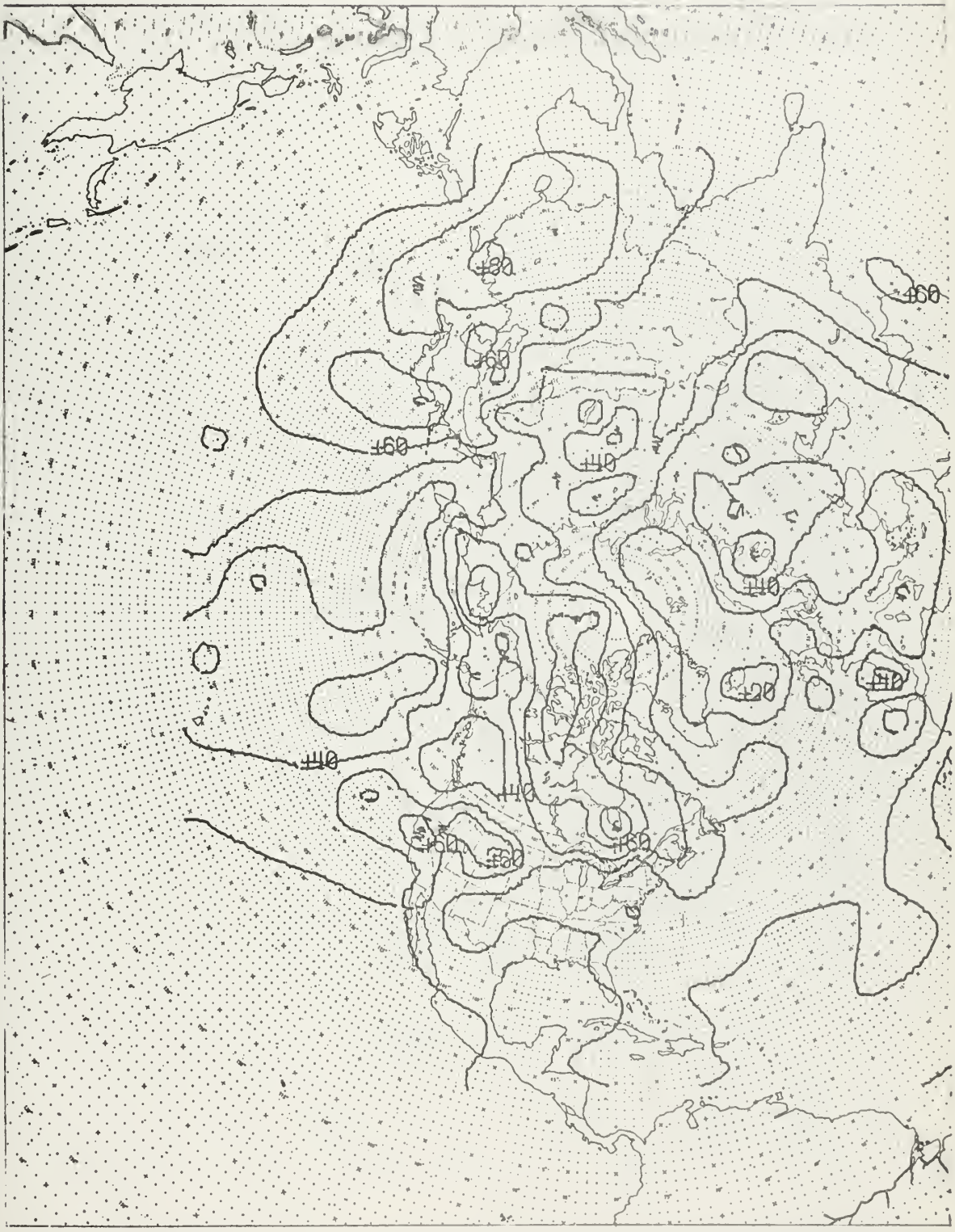

SCALE: 1:120,000,000

FLEET NUMERICAL WEATHER FACILITY, MONTEREY, CALIFORNIA

00Z 22 JAN 62 D 300

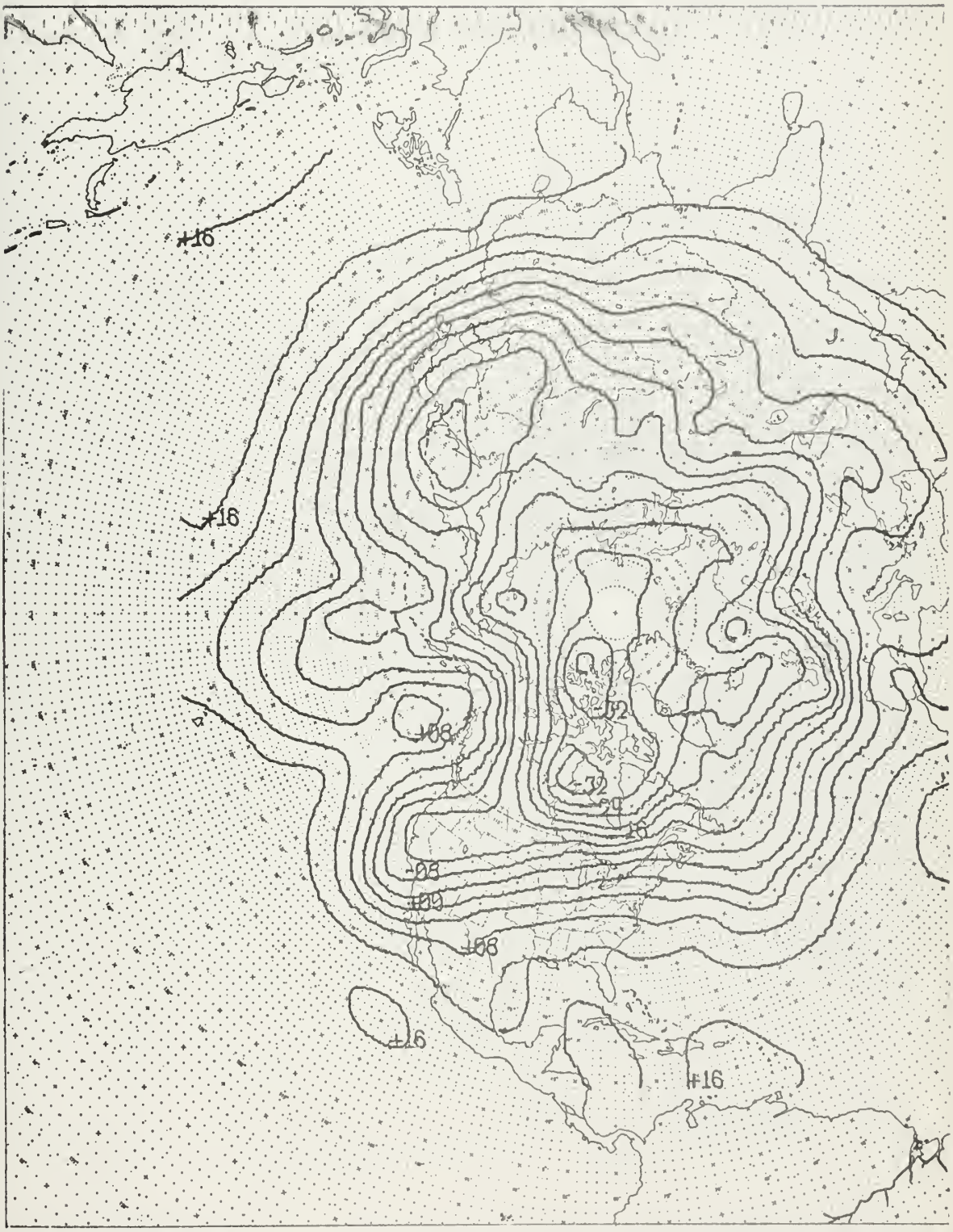

SCALE: 1:120,000,000

FLEET NUMERICAL WEATHER FACILITY, MONTEREY, CALIFORNIA

00Z 22 JAN 62 T 300

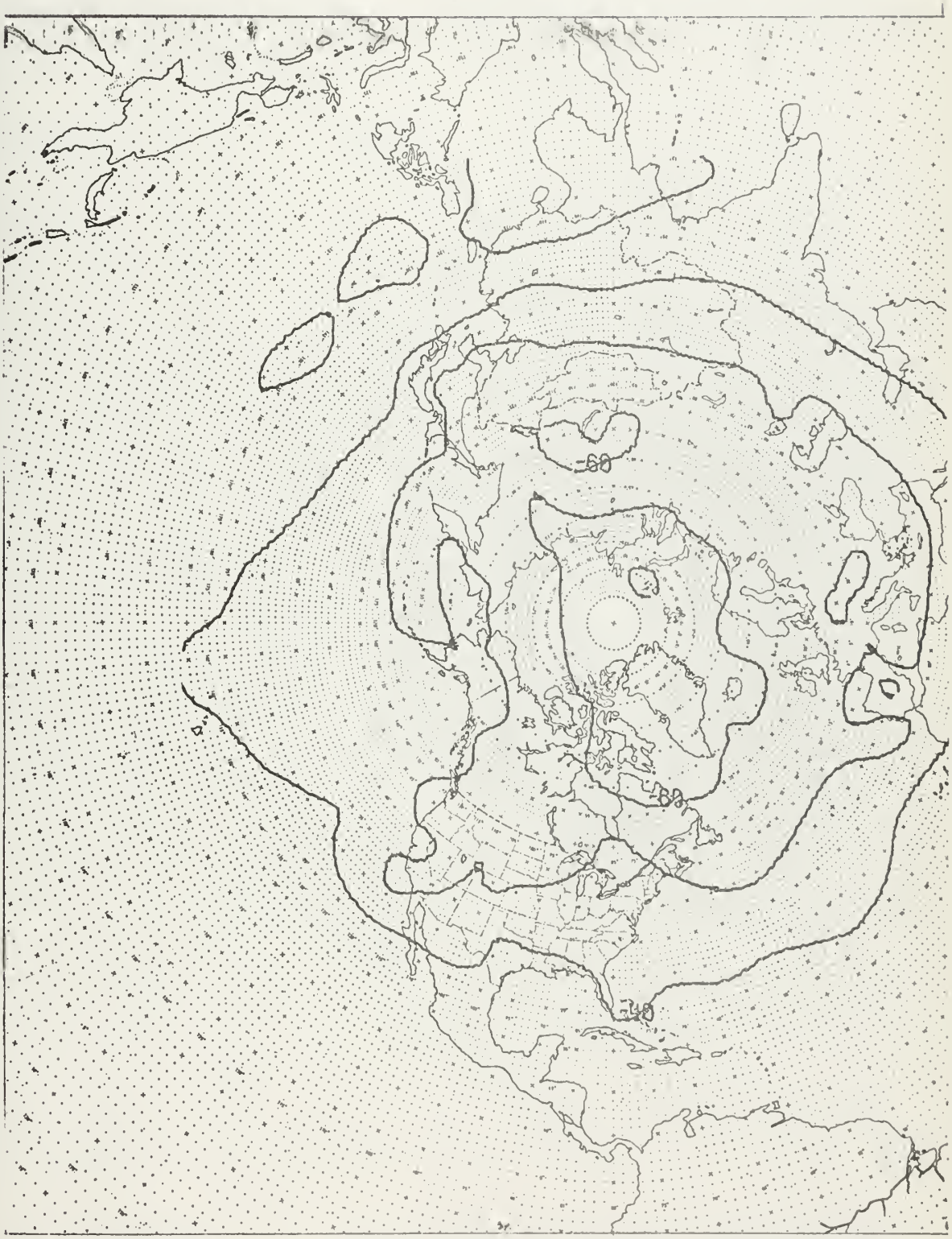

SCALE: 1:120,000,000

FLEET NUMERICAL WEATHER FACILITY, MONTEREY, CALIFORNIA

00Z 22 JAN 62 SIG 300

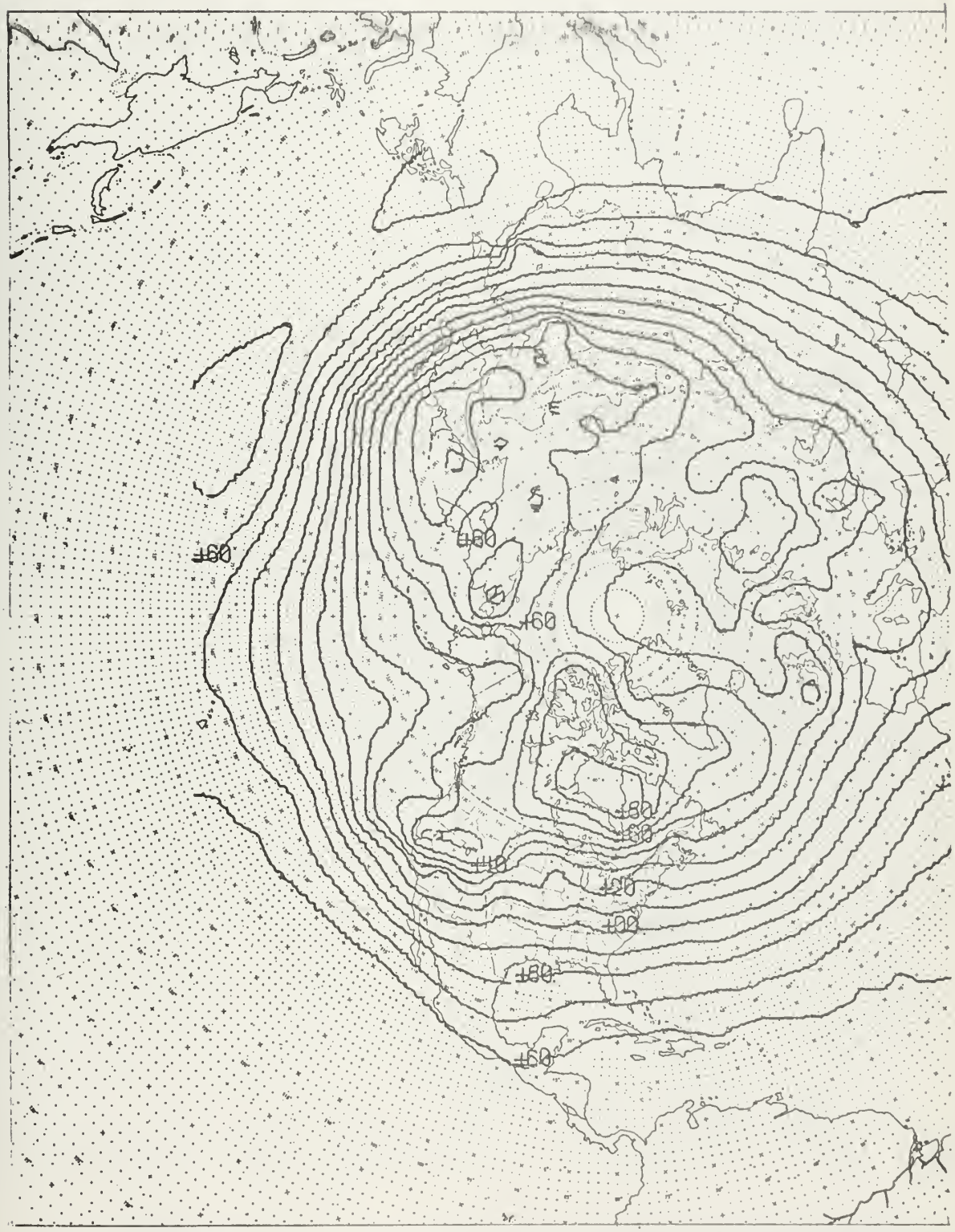

SCALE: 1:120,000,000

FLEET NUMERICAL WEATHER FACILITY, MONTEREY, CALIFORNIA

12Z 23 JAN 62 D 1000

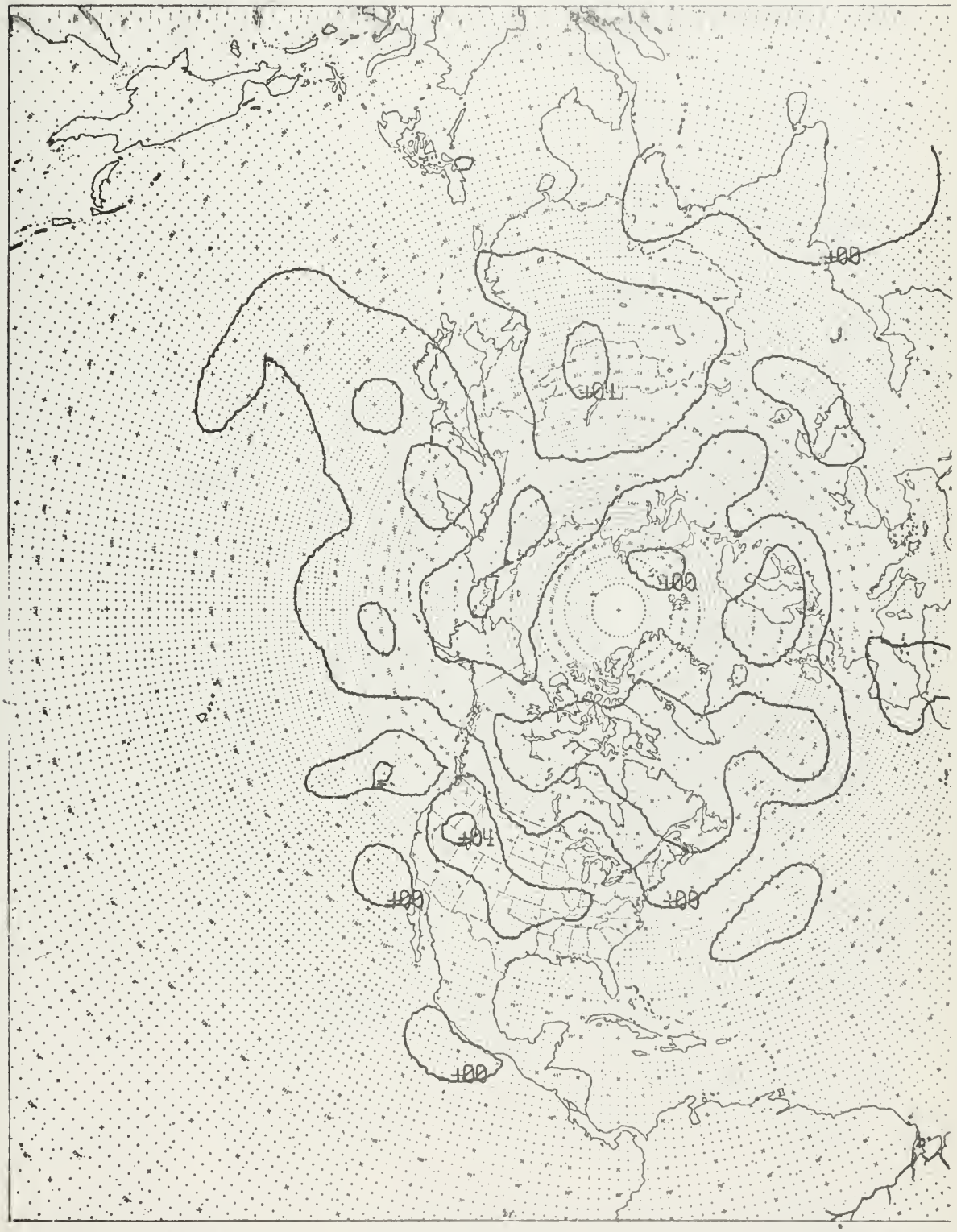

SCALE: 1:120,000,000

FLEET NUMERICAL WEATHER FACILITY, MONTEREY, CALIFORNIA

12Z 23 JAN 62 T 1000

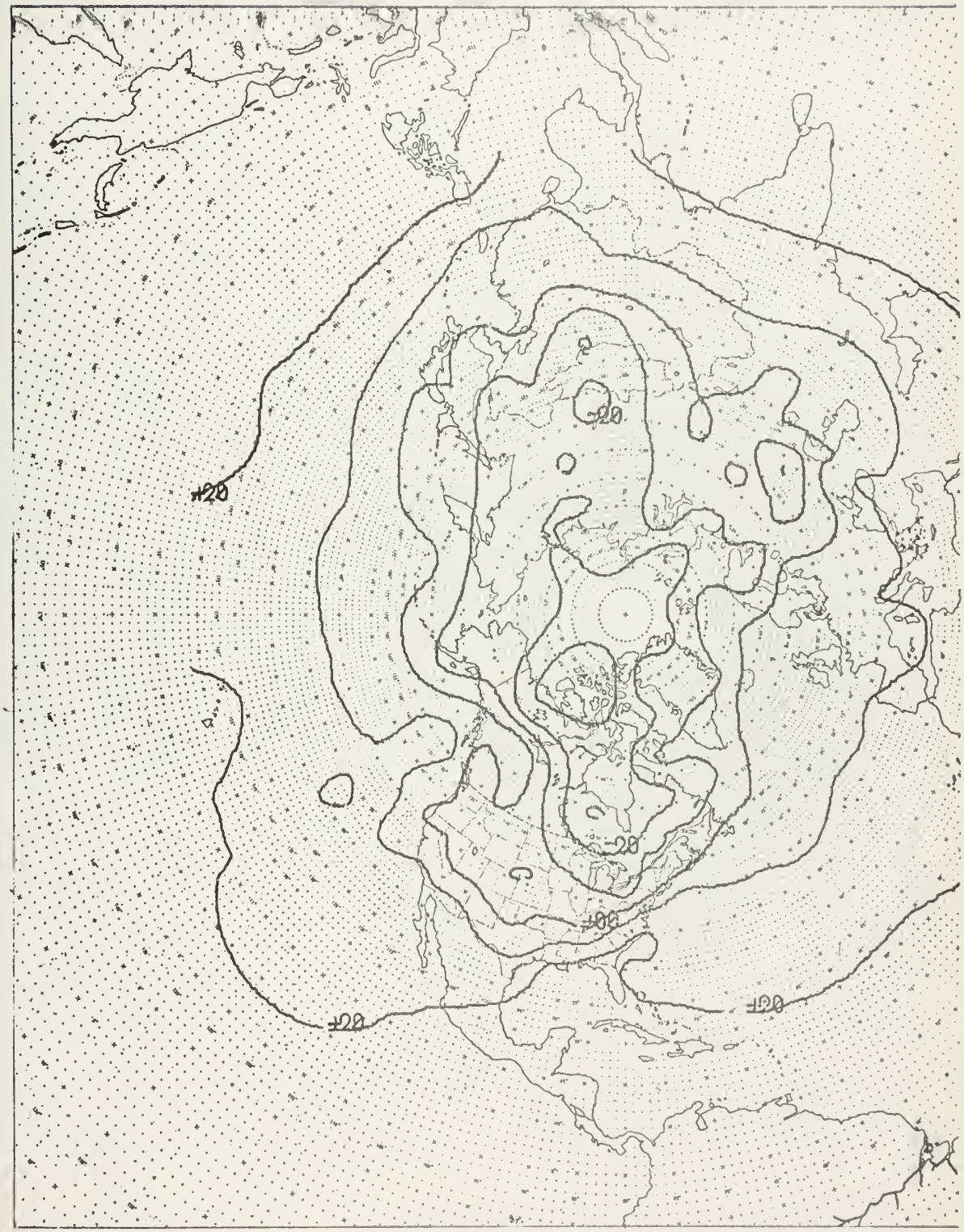

SCALE: 1:120,000,000

FLEET NUMERICAL WEATHER FACILITY, MONTEREY, CALIFORNIA

12Z 23 JAN 62 D 850

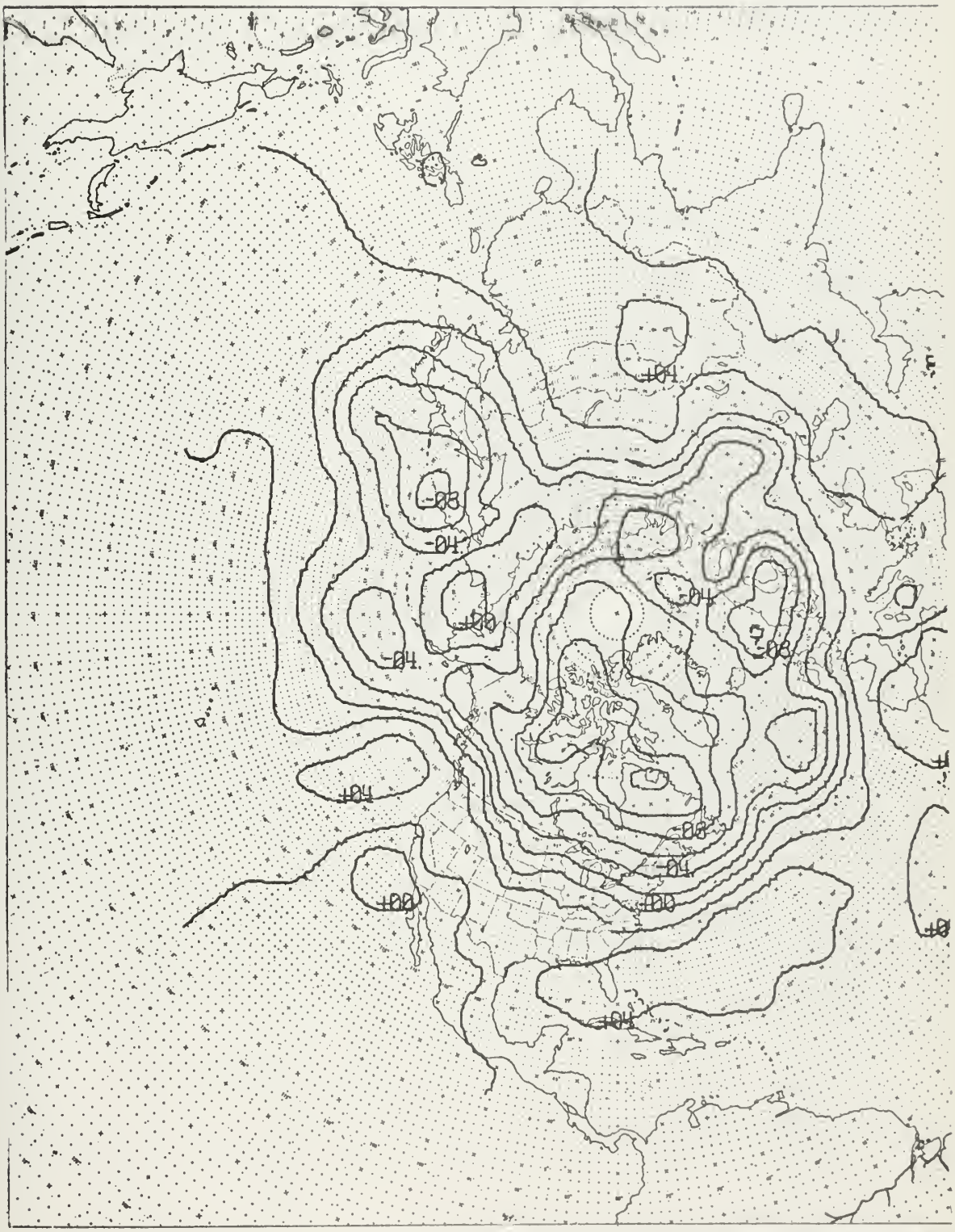

SCALE: 1:120,000,000

FLEET NUMERICAL WEATHER FACILITY, MONTEREY, CALIFORNIA

12Z 23 JAN 62 T 850

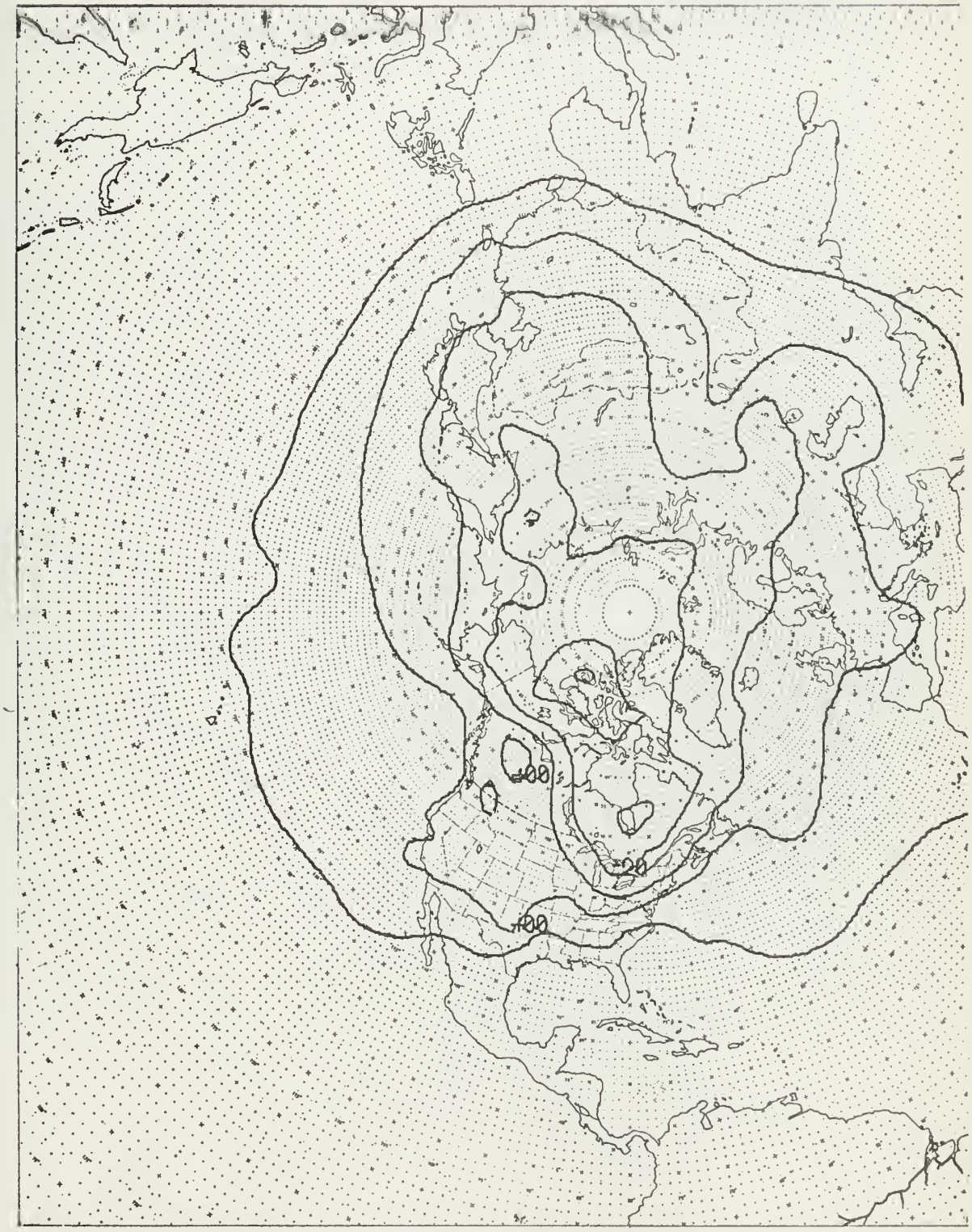

SCALE: 1:120,000,000 FLEET NUMERICAL WEATHER FACILITY, MONTEREY, CALIFORNIA

12Z 23 JAN 62 D 700

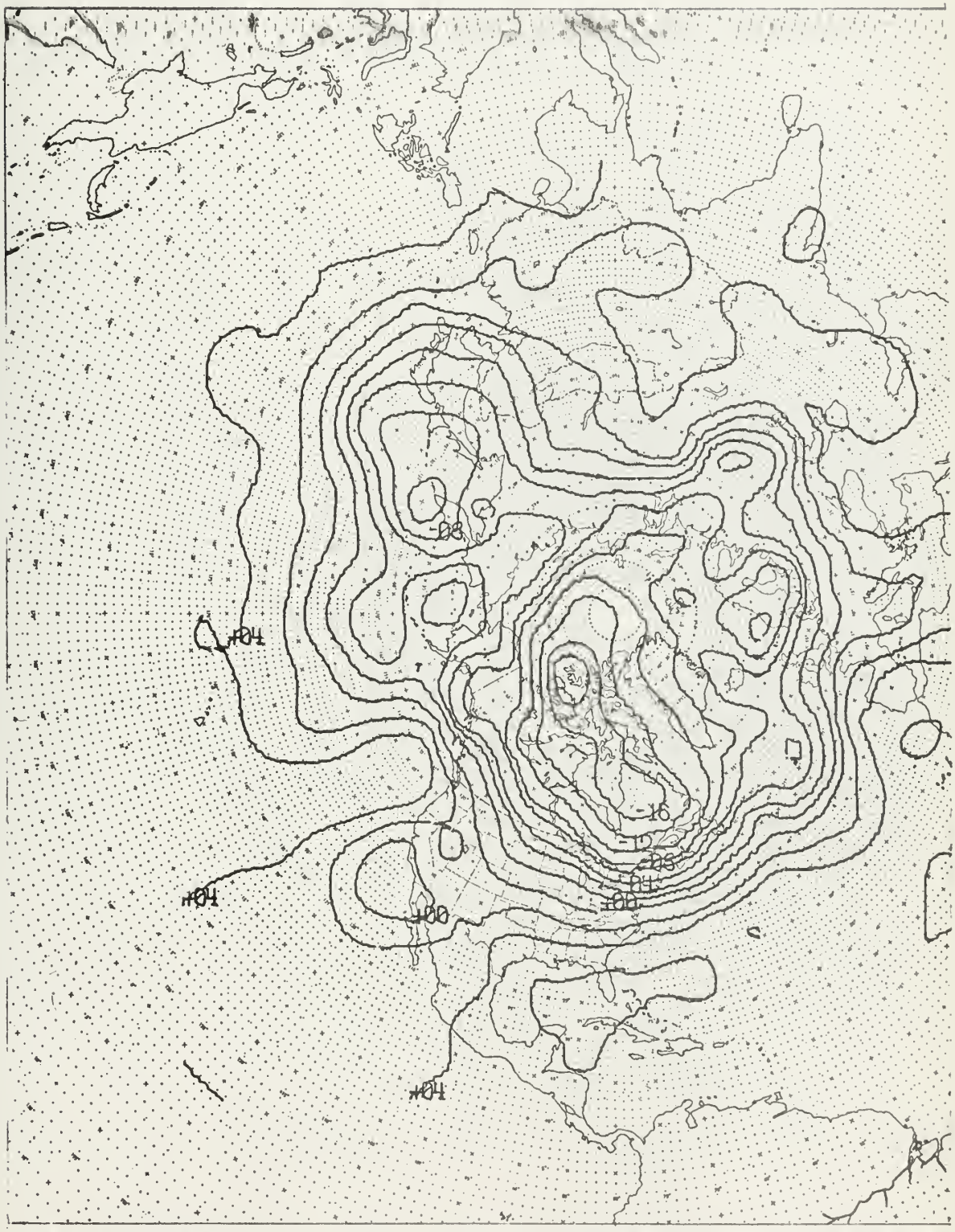

SCALE: 1:120,000,000

FLEET NUMERICAL WEATHER FACILITY, MONTEREY, CALIFORNIA

12Z 23 JAN 62 T 700

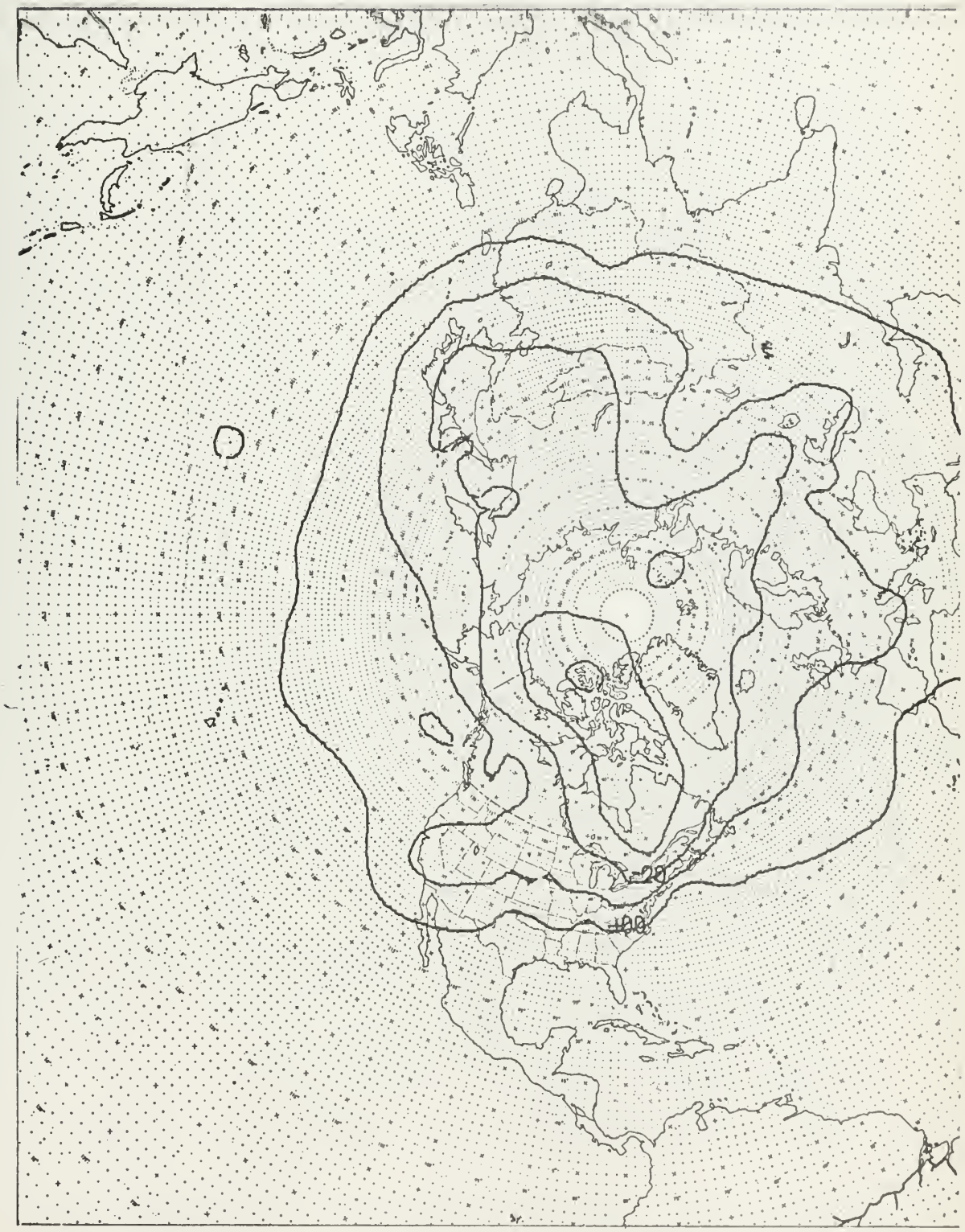

SCALE: 1:120,000,000

FLEET NUMERICAL WEATHER FACILITY, MONTEREY, CALIFORNIA

12Z 23 JAN 62 D 500

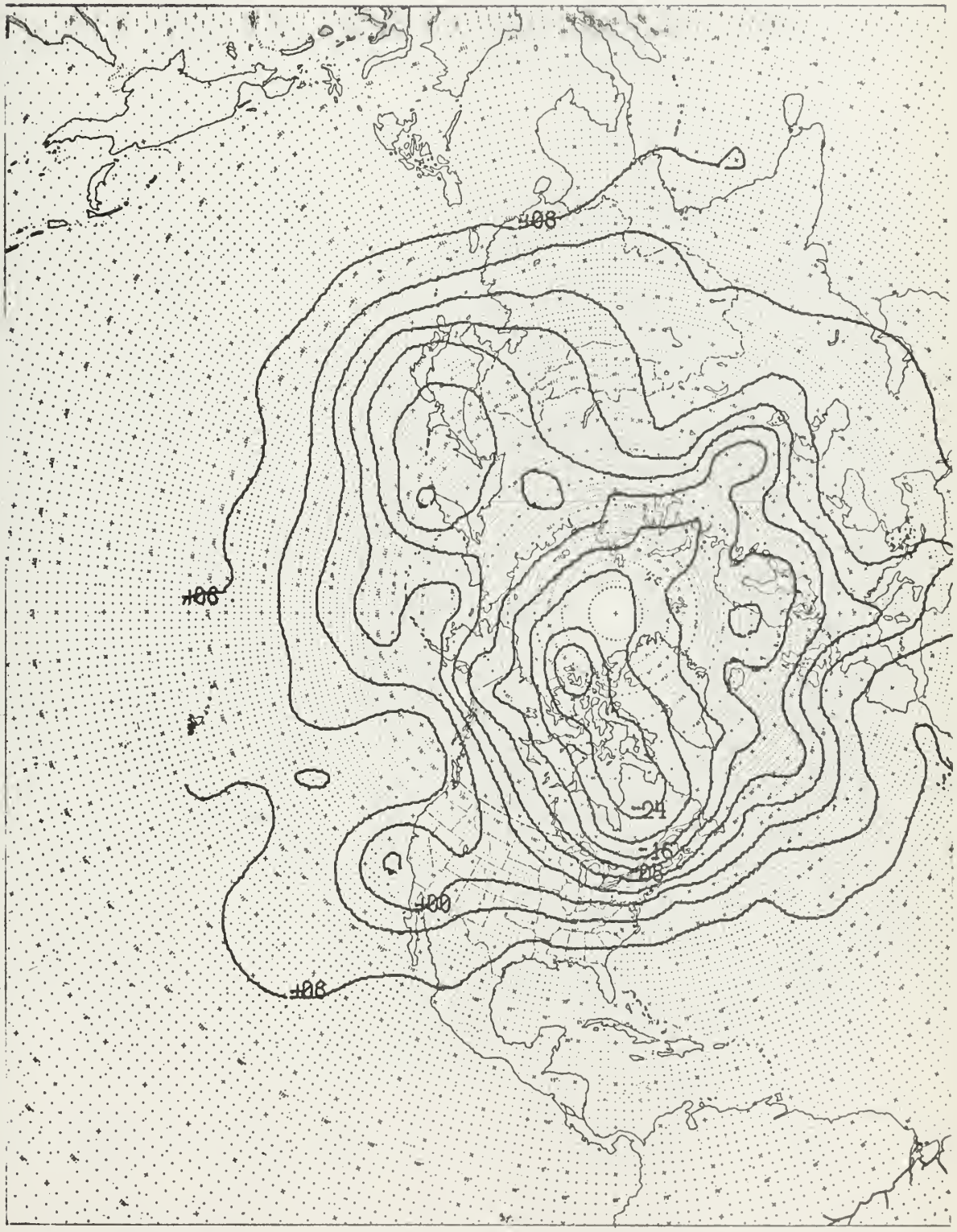

SCALE: 1:120,000,000

FLEET NUMERICAL WEATHER FACILITY, MONTEREY, CALIFORNIA

12Z 23 JAN 62 T 500

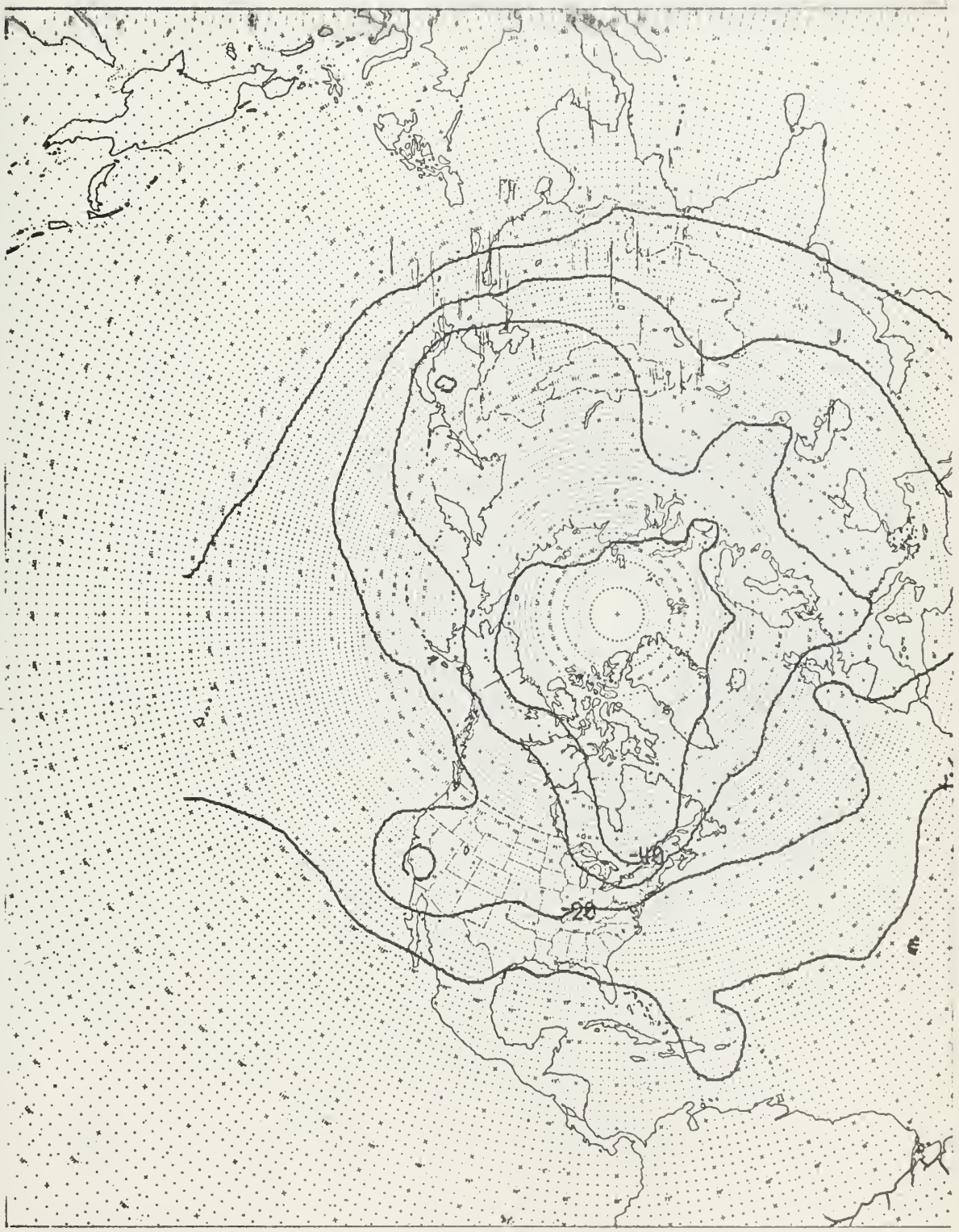

SCALE: 1:120,000,000

FLEET NUMERICAL WEATHER FACILITY, MONTEREY, CALIFORNIA

12Z 23 JAN 62 D 300

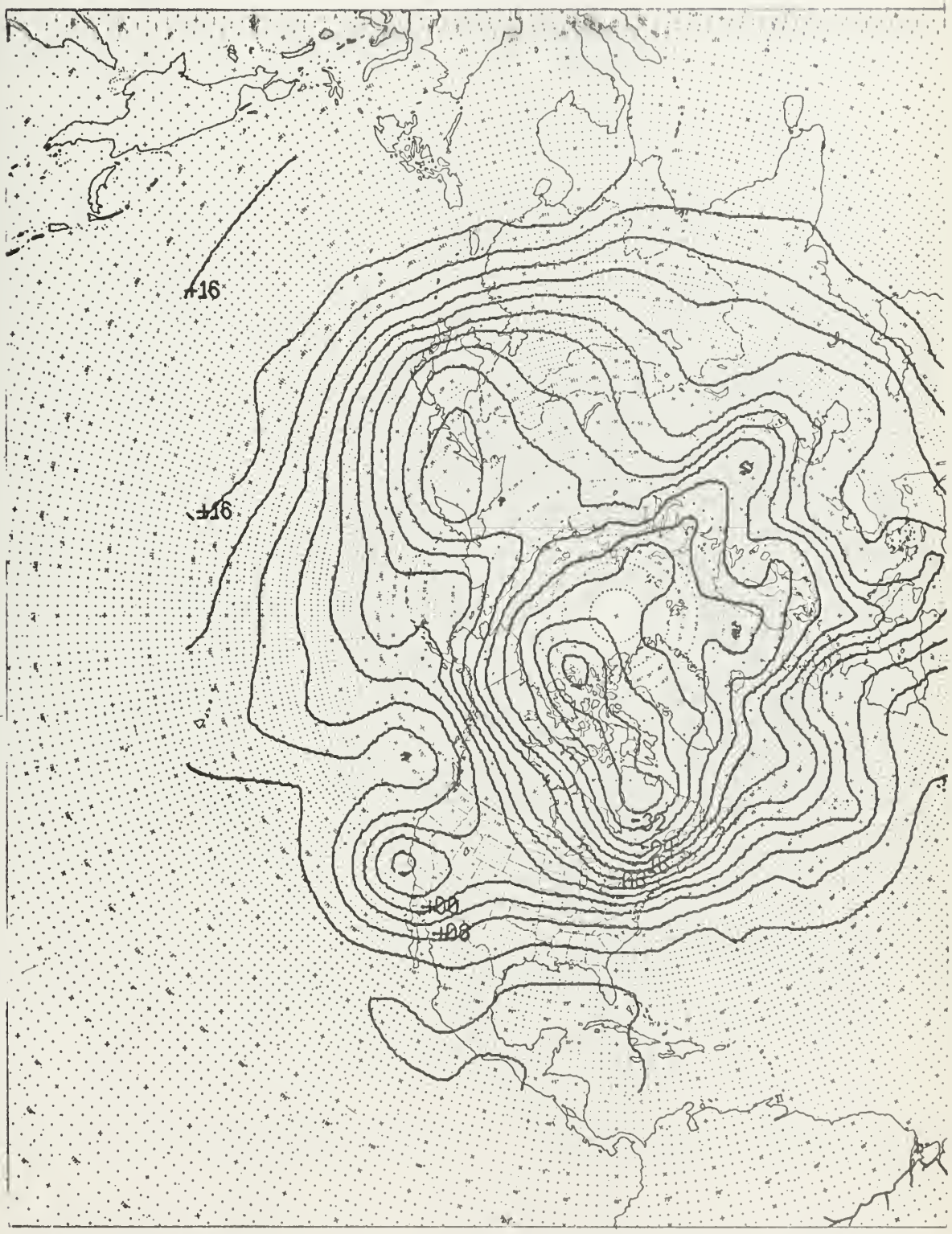

SCALE: 1:120,000,000

FLEET NUMERICAL WEATHER FACILITY, MONTEREY, CALIFORNIA

12Z 23 JAN 62 T 300

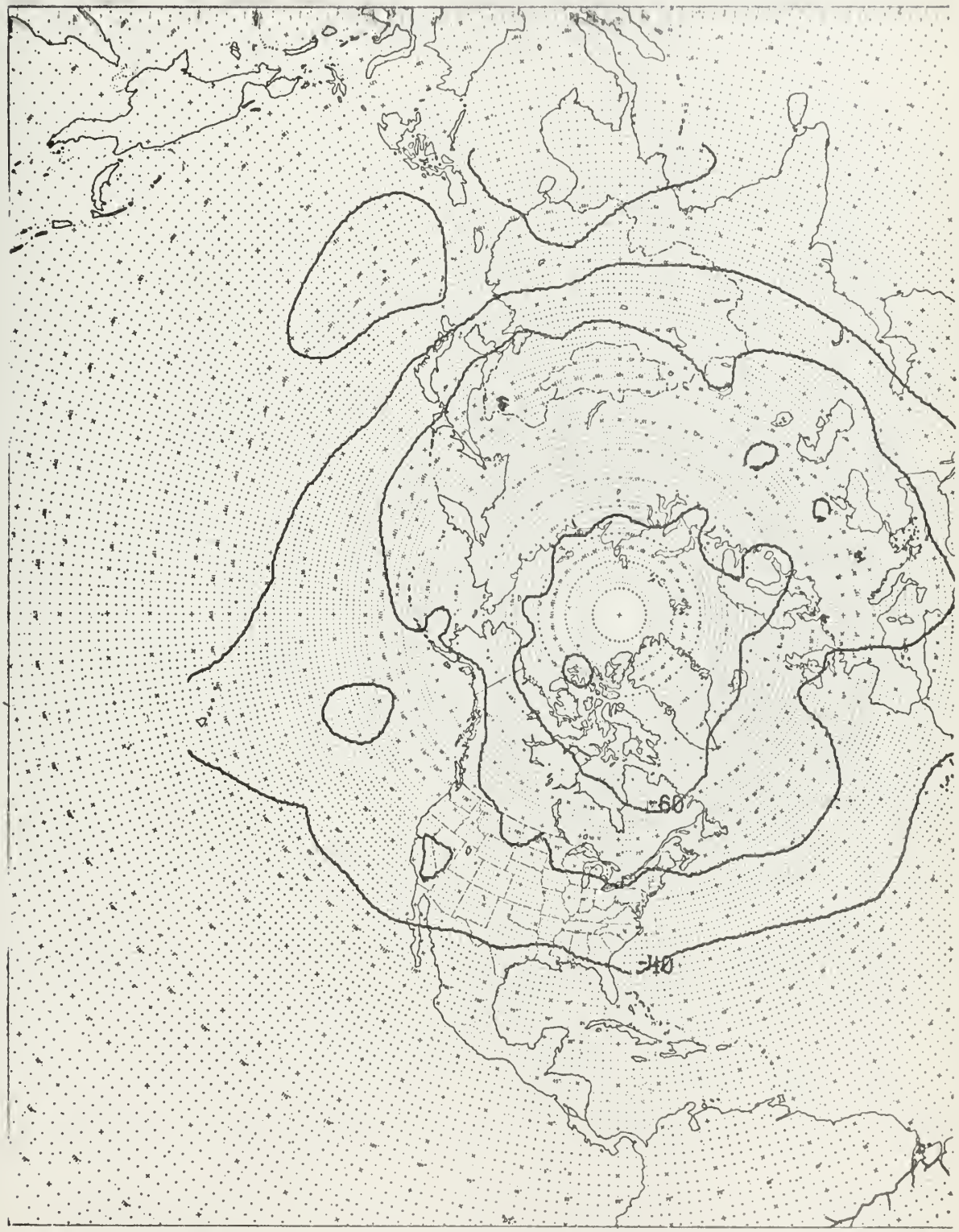

SCALE: 1:120,000,000

FLEET NUMERICAL WEATHER FACILITY, MONTEREY, CALIFORNIA

12Z 26 JAN 62 D 1000

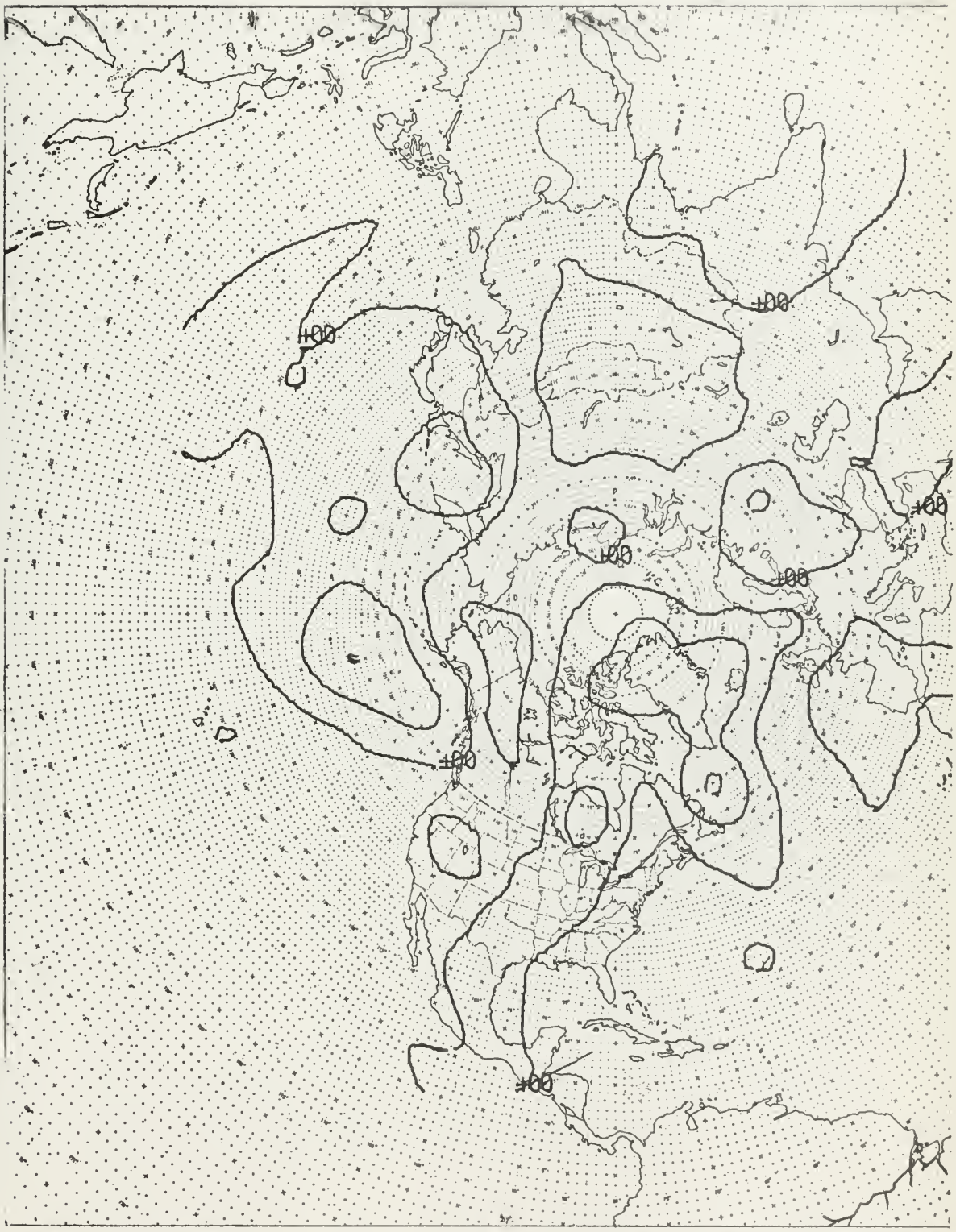

SCALE: 1:120,000,000 FLEET NUMERICAL WEATHER FACILITY, MONTEREY, CALIFORNIA

12Z 26 JAN 62 D 500

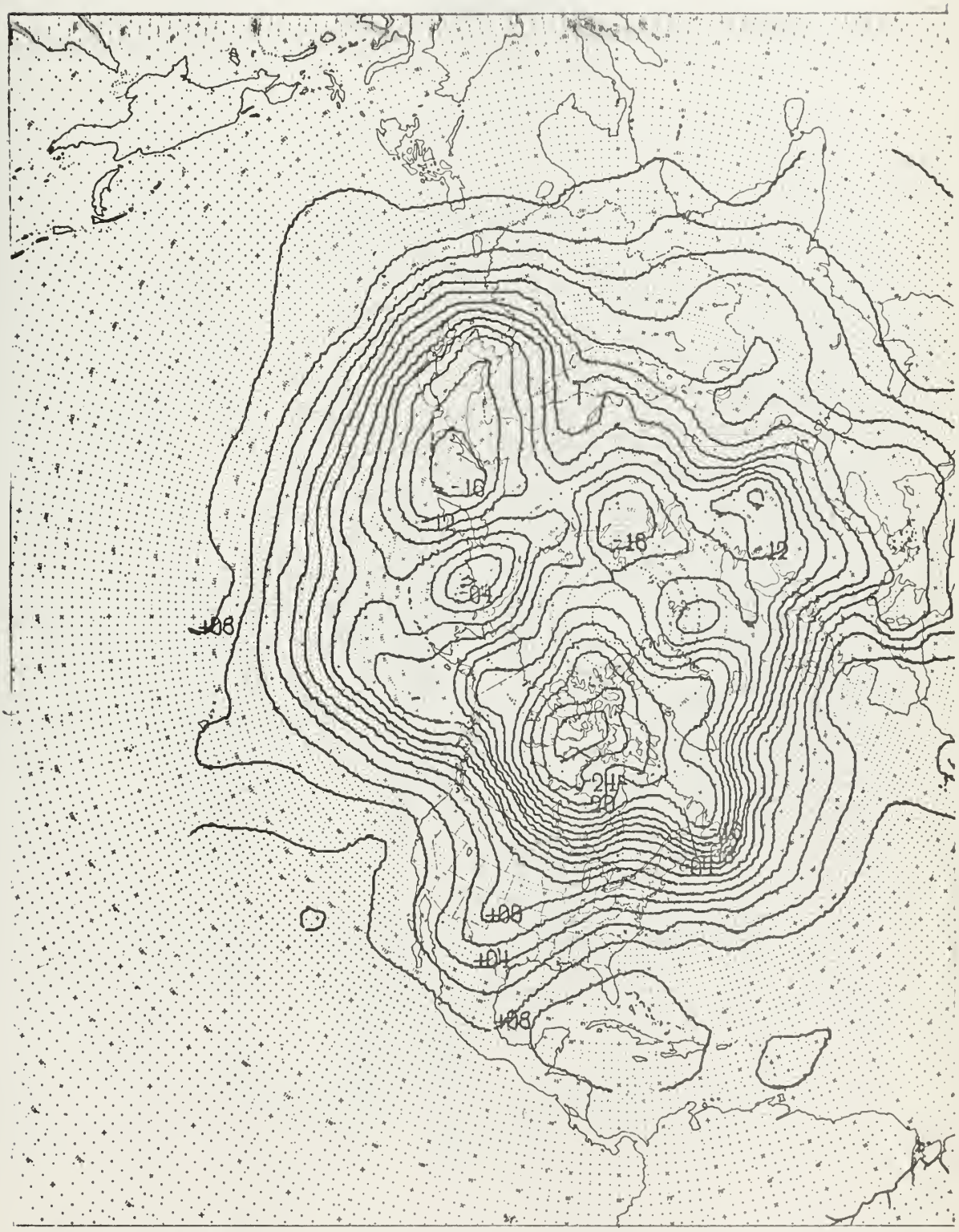

SCALE: 1:120,000,000

FLEET NUMERICAL WEATHER FACILITY, MONTEREY, CALIFORNIA

APPENDIX D

TIROS OBSERVATIONS AND

CORRESPONDING OMEGA FIELDS

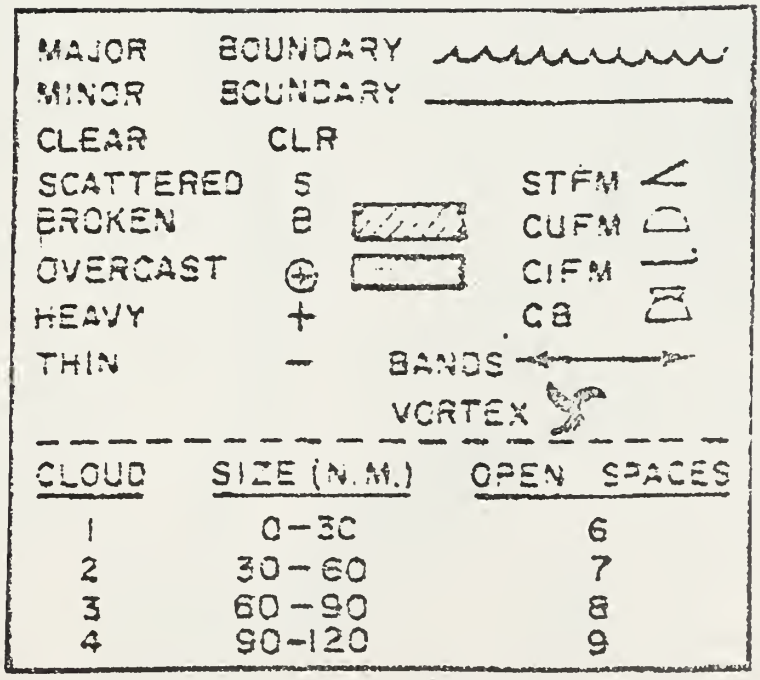

CLOUD	SIZE (N.M.)	OPEN SPACES
1	0-30	6
2	30-60	7
3	60-90	8
4	90-120	9

TIROS CODE

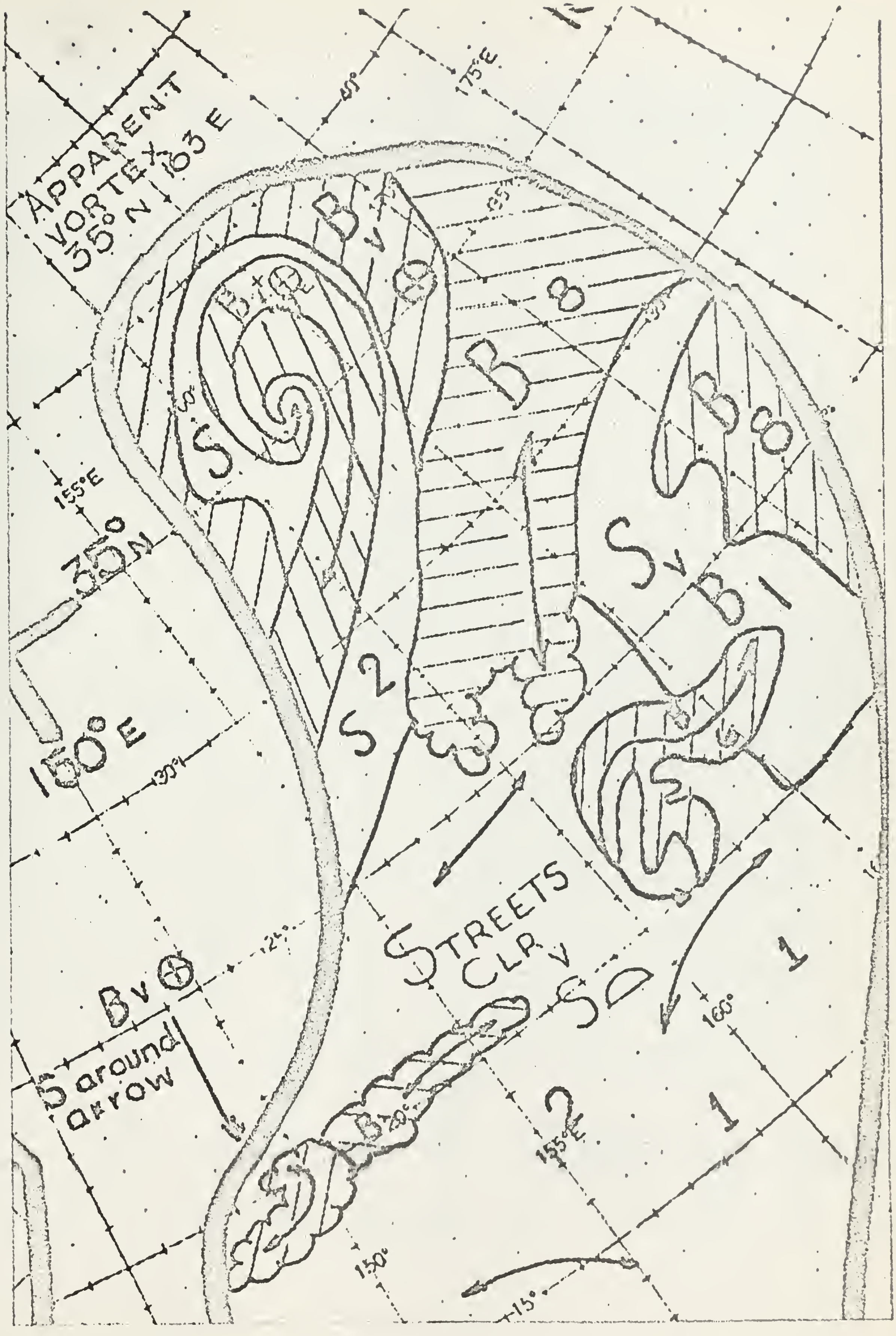
APPARENT VORTEX 35° N 163 E
175°E
35°N
155°E
150°E
30°
B
B 8
S
S2
S
B 8
S v B 1
STREETS CLR
S
B v ⊗
S around arrow
1
1
2
160°
155°E
150°
25°
20°
15°

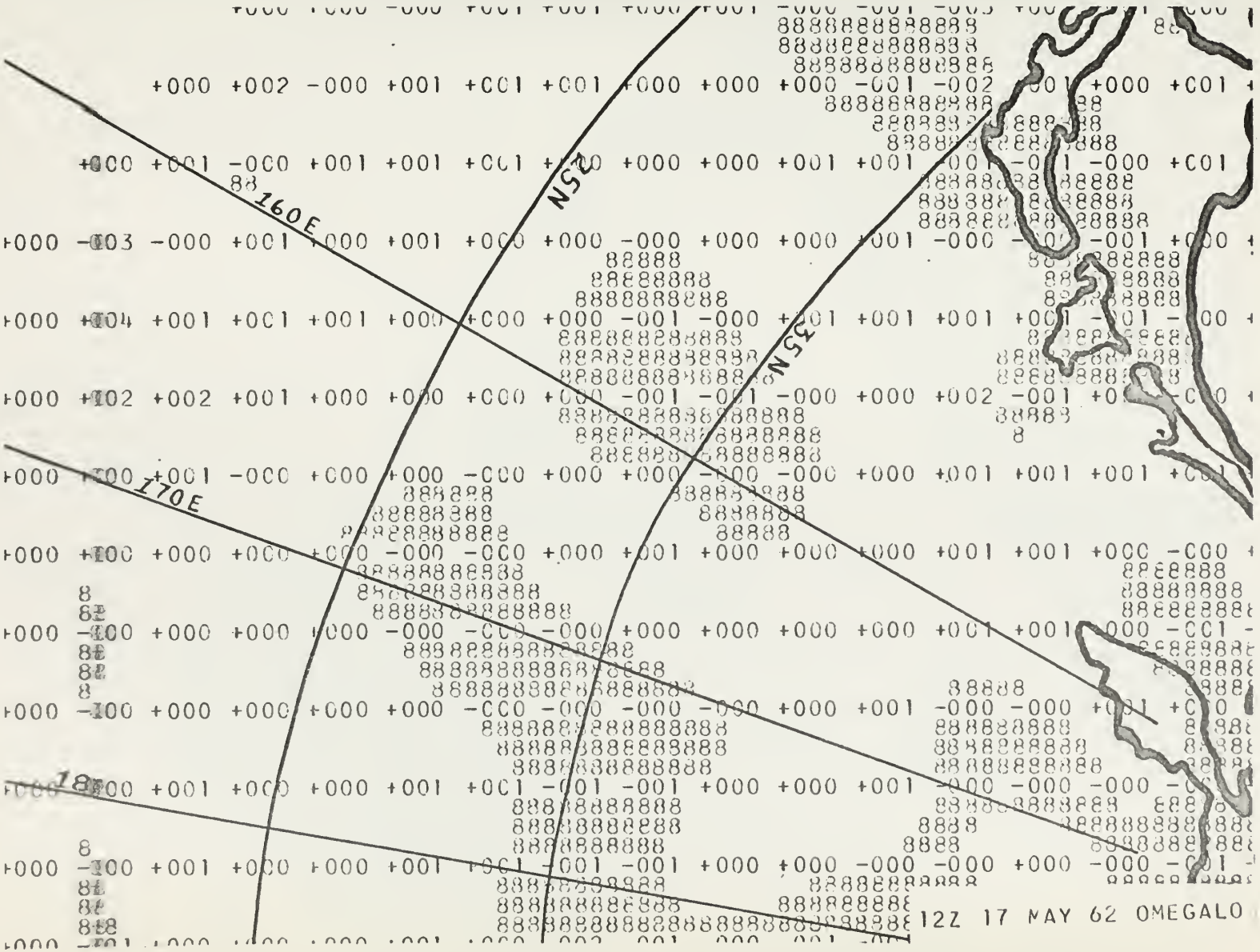
160E
25N
35N
170E
180
12Z 17 MAY 62 OMEGALO

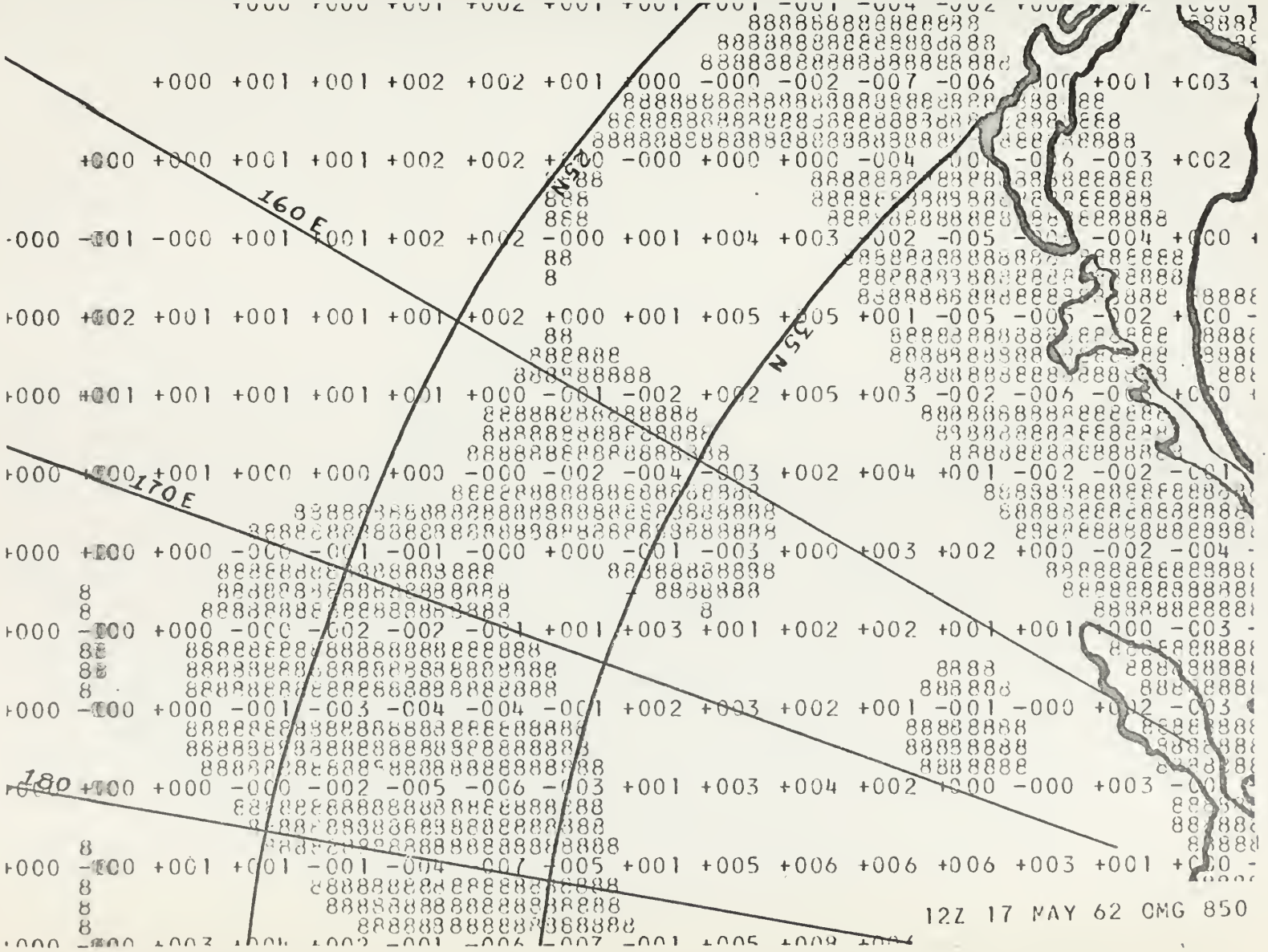
160 E
170 E
180
25N
35N
12Z 17 MAY 62 OMG 850

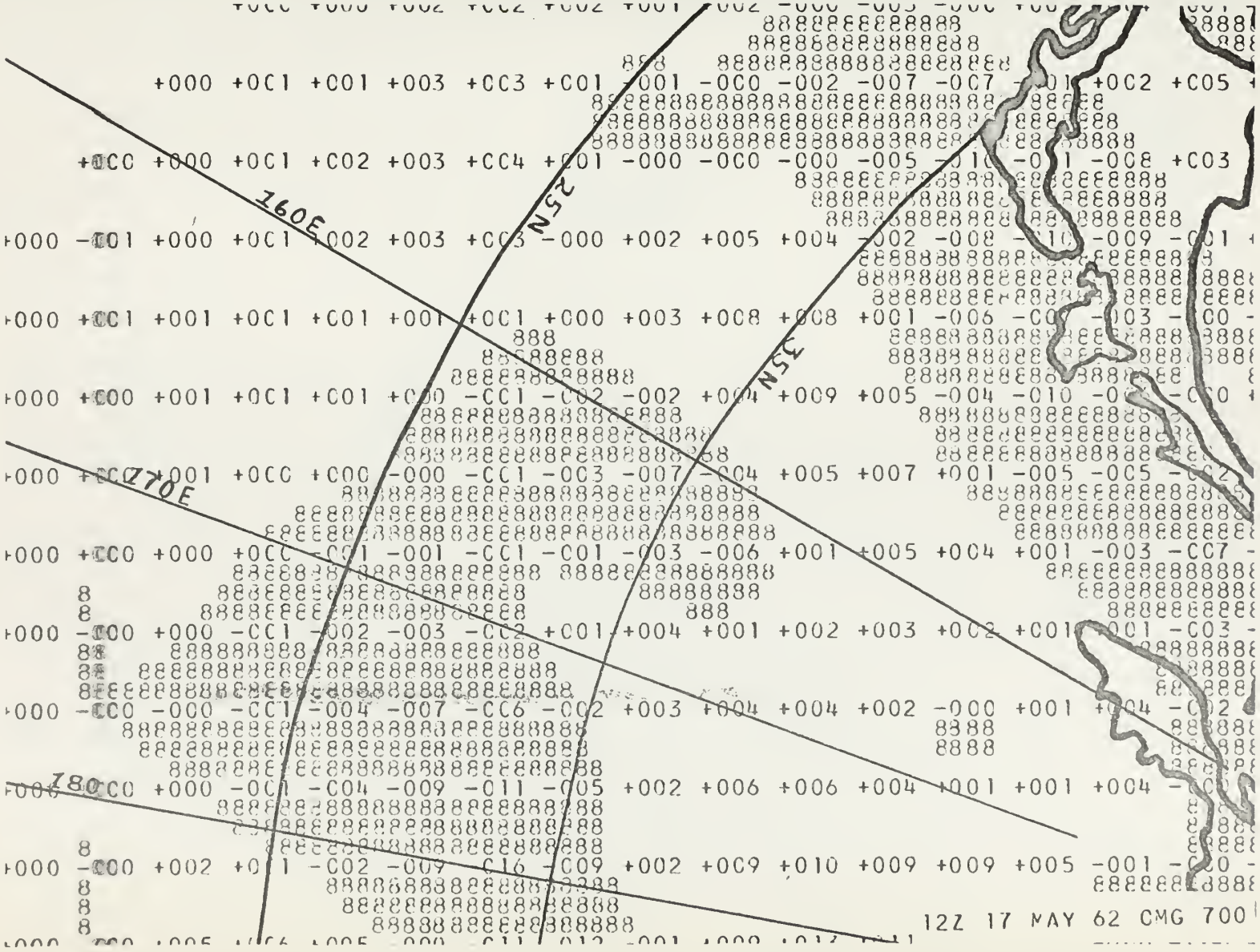
160E
25N
35N
170E
180
12Z 17 MAY 62 CMG 700

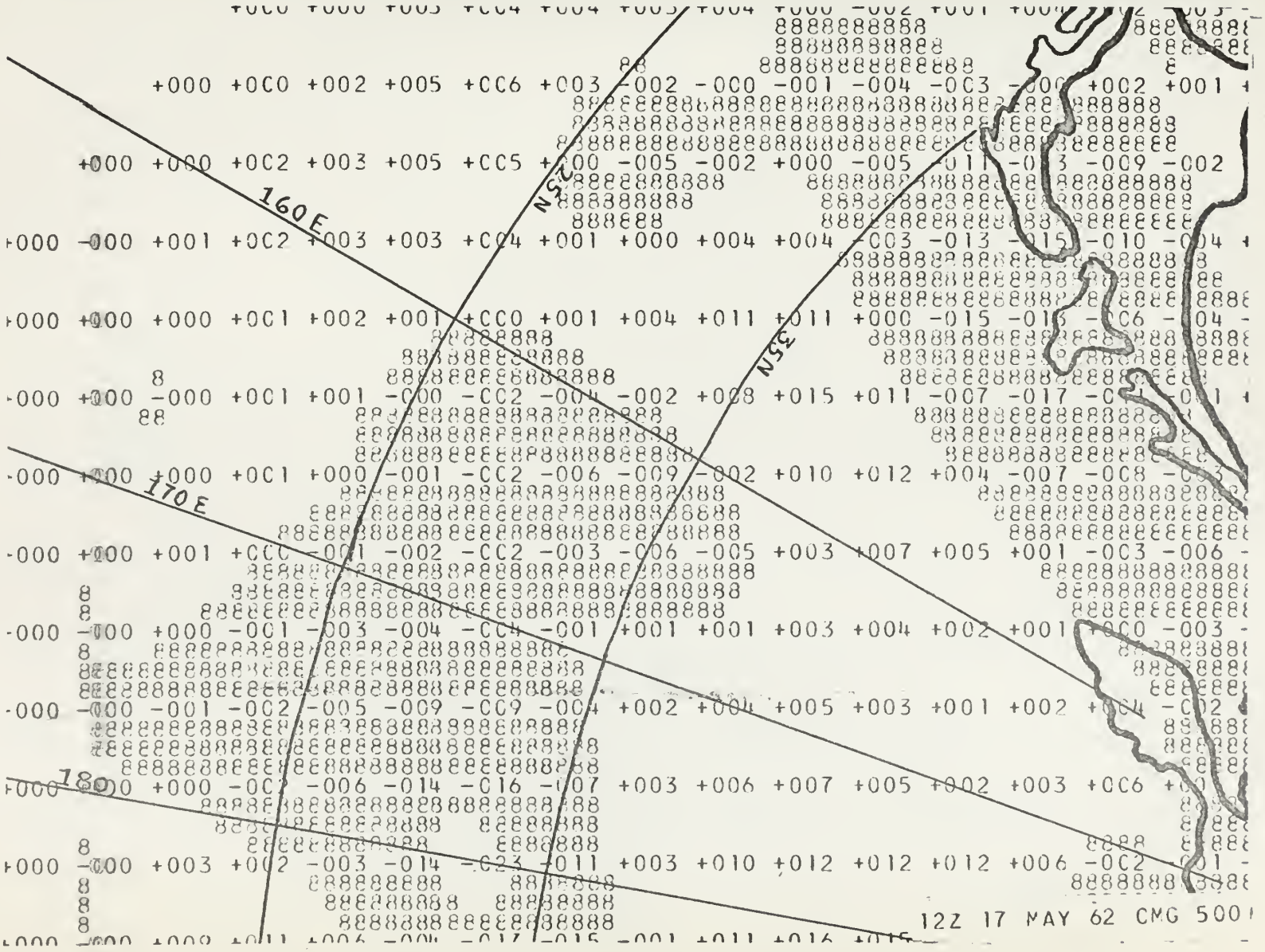
160 E
170 E
180
25N
35N
12Z 17 MAY 62 CMG 500

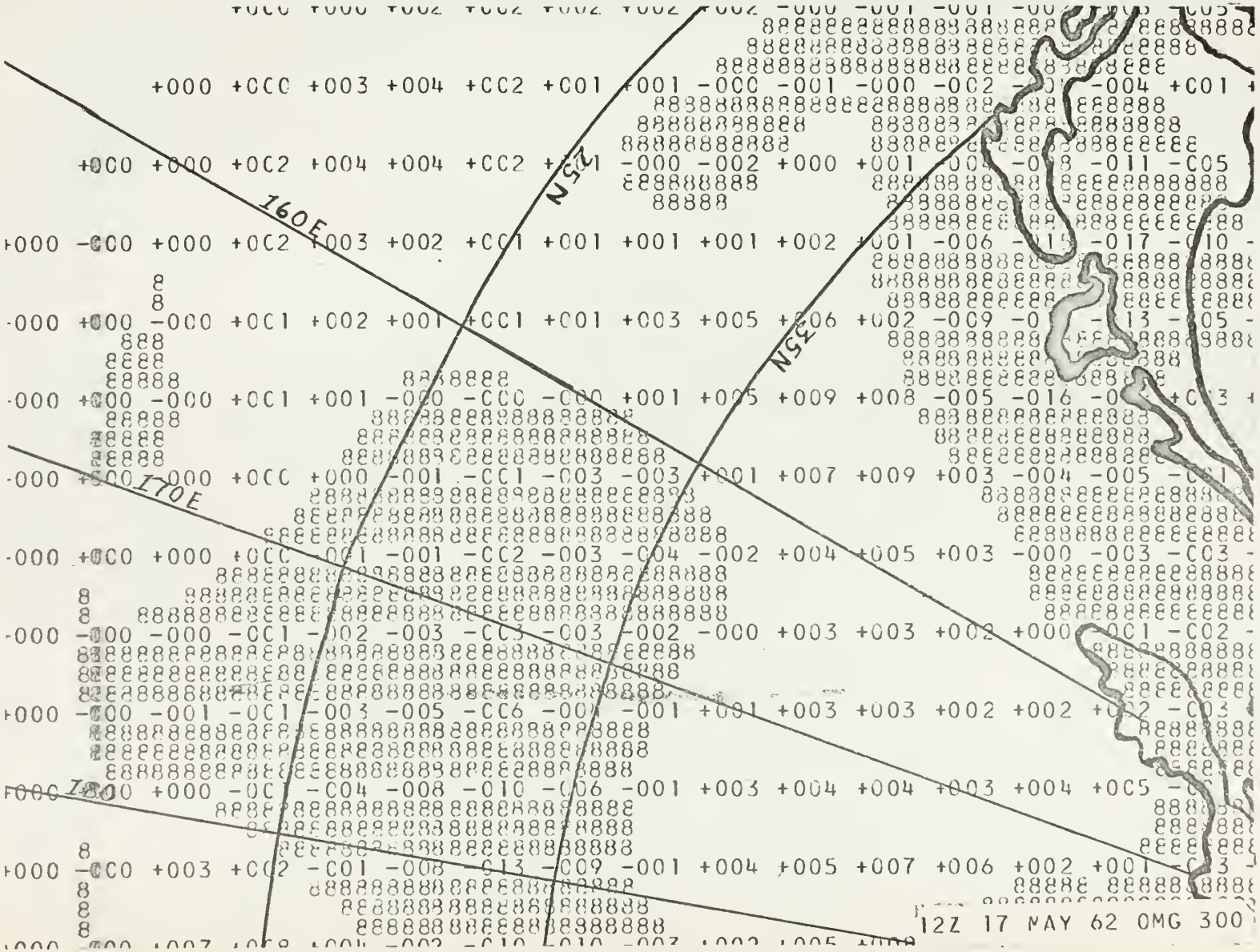
160E
25N
35N
170E
180
12Z 17 MAY 62 OMG 300

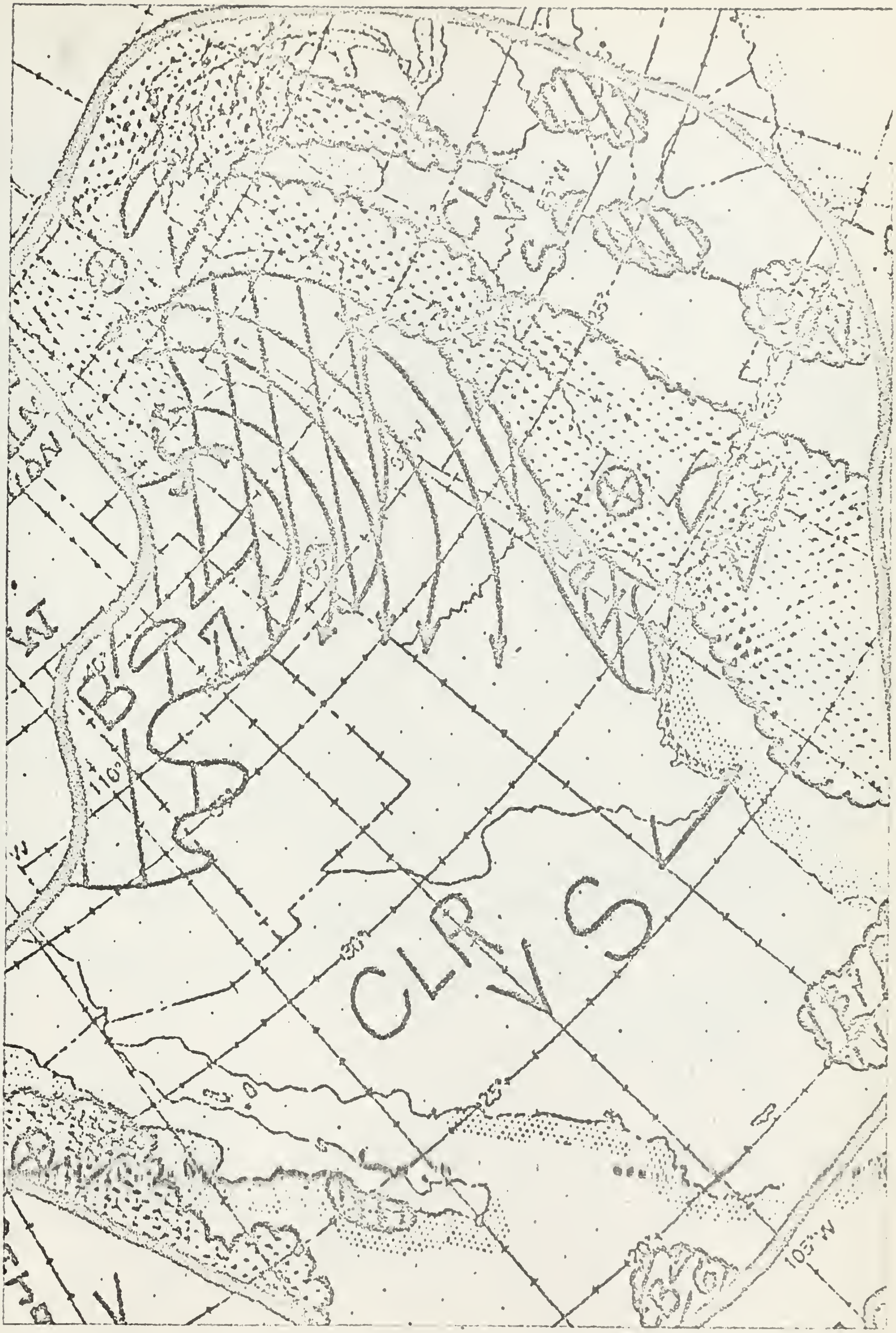
CLR
VS
105°W

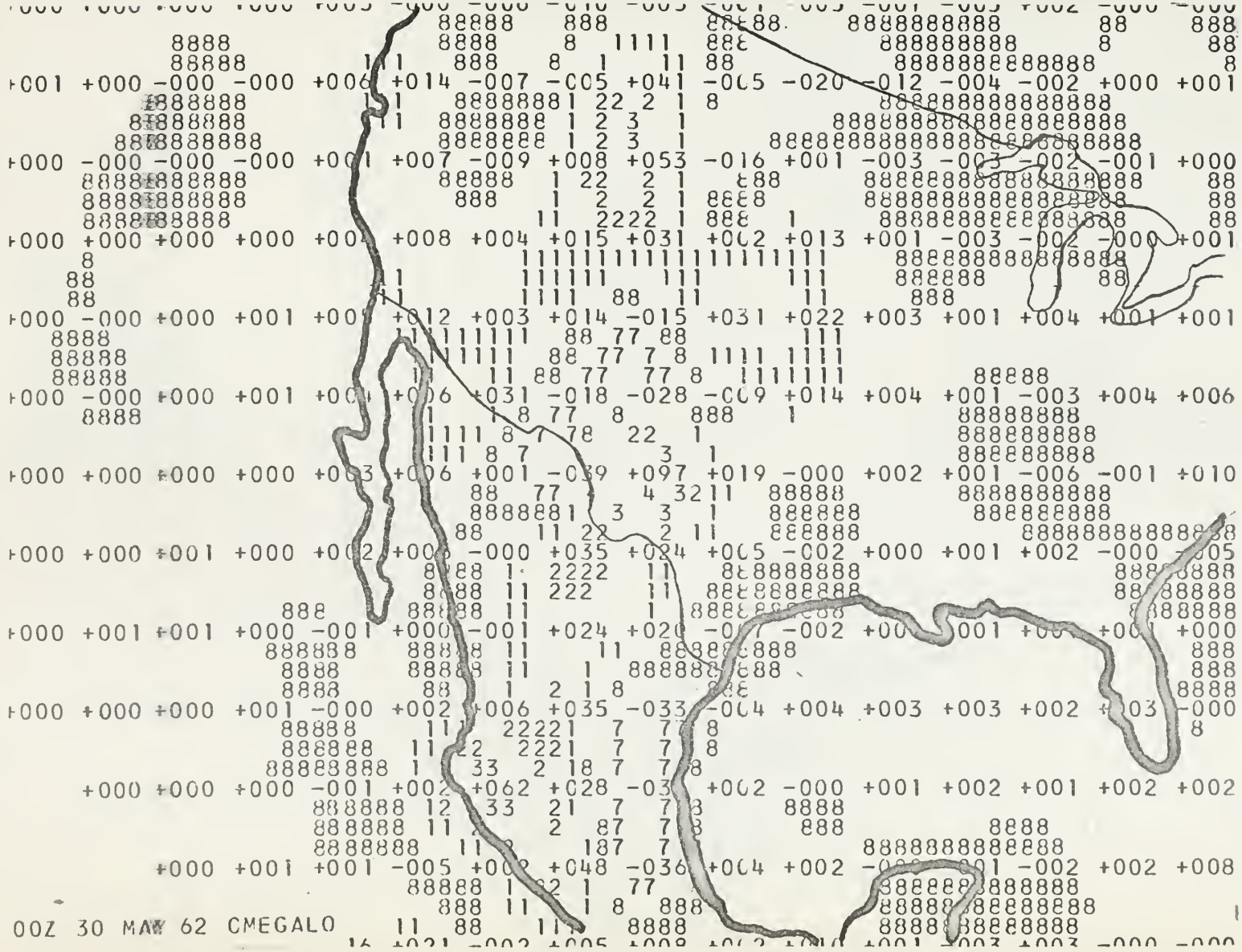
00Z 30 MAY 62 CMEGALO

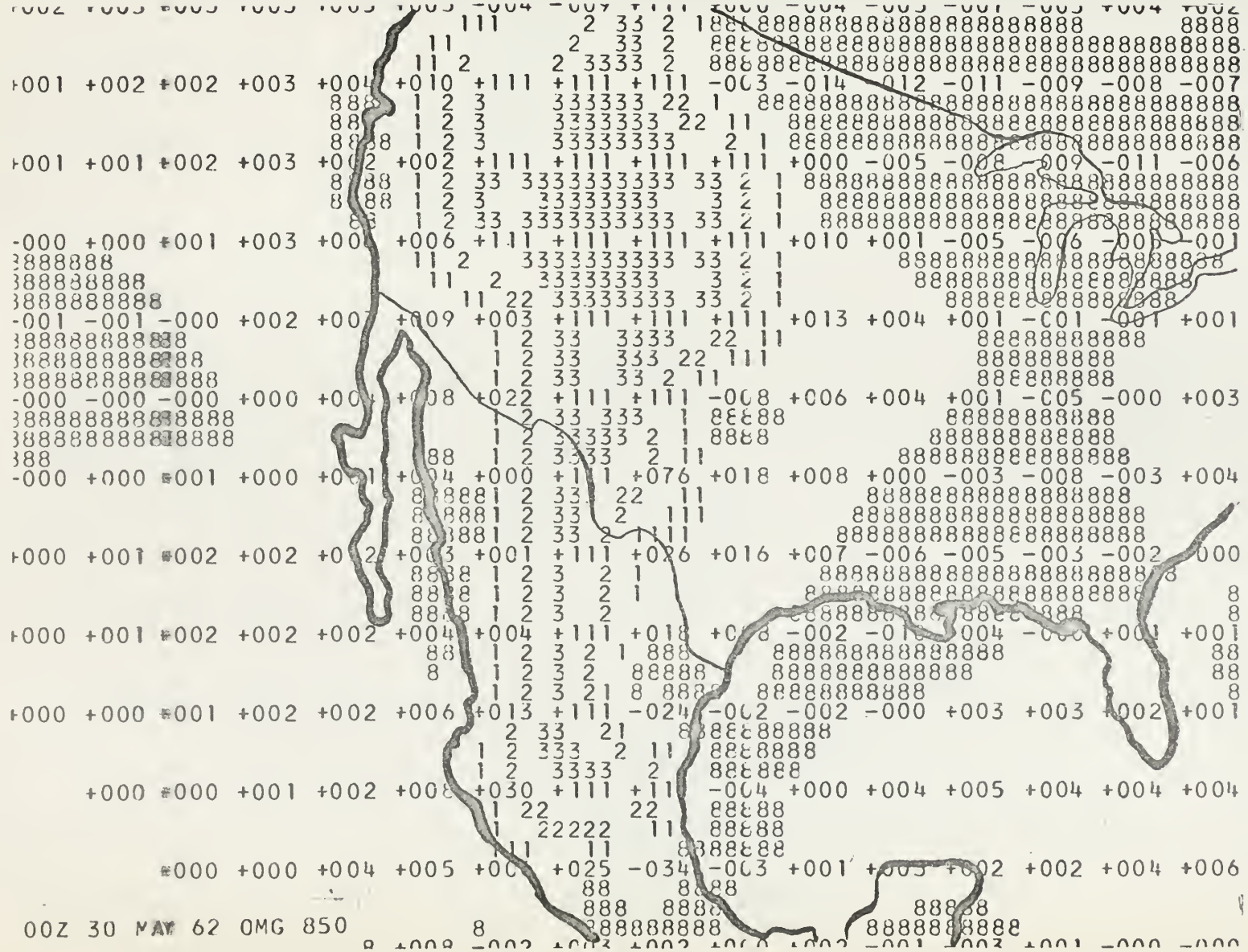
00Z 30 MAY 62 OMG 850

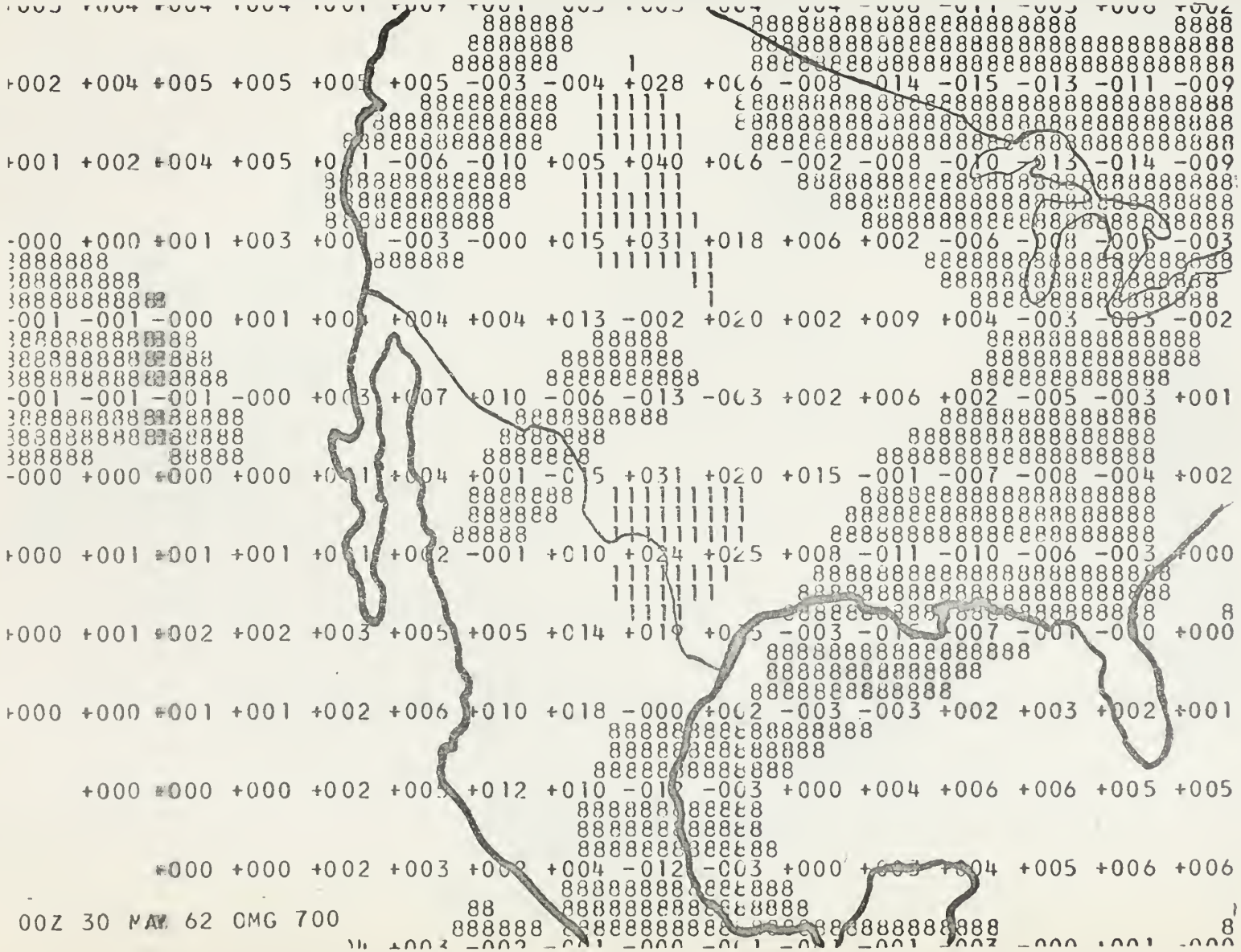
00Z 30 MAR 62 OMG 700

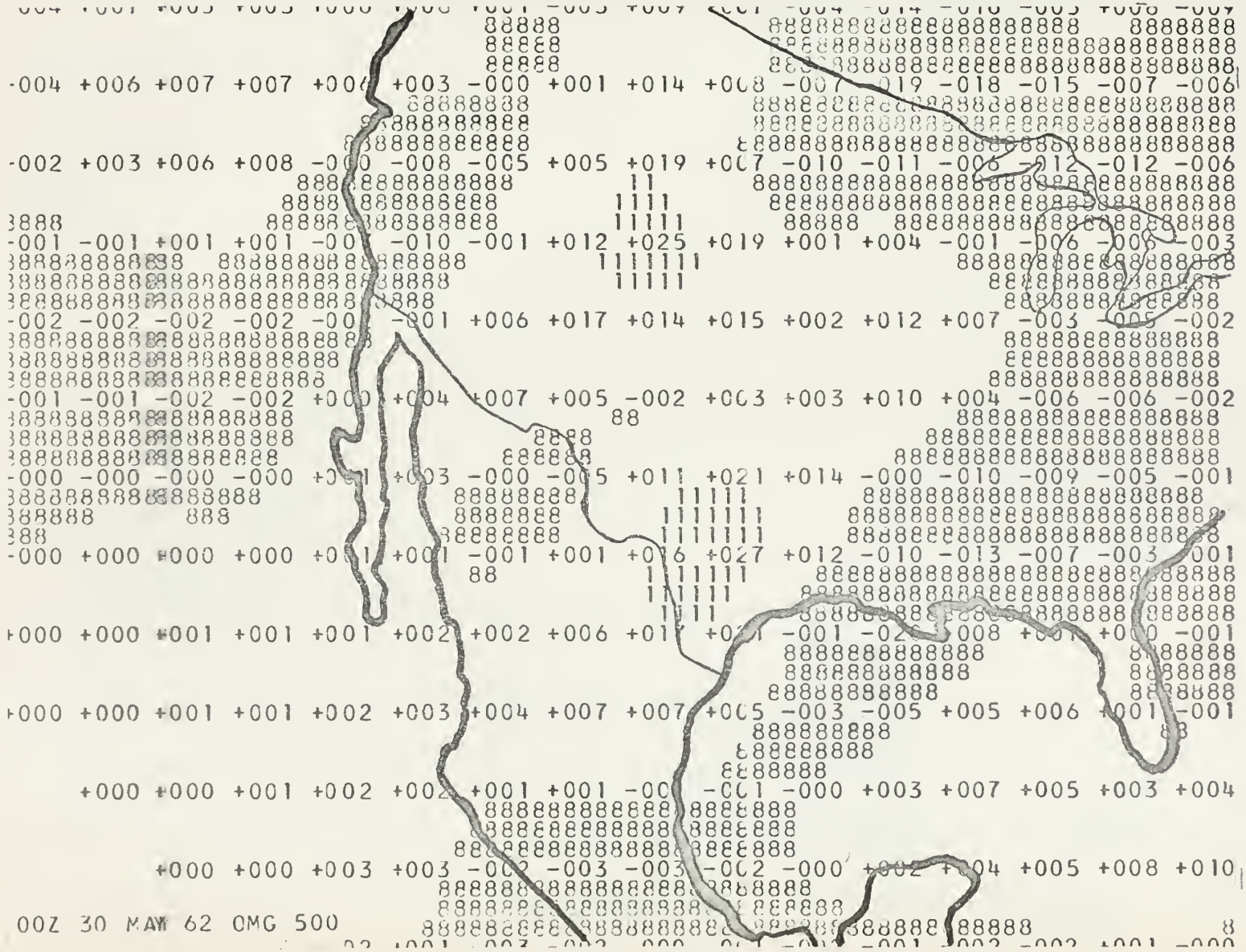
00Z 30 MAY 62 OMG 500

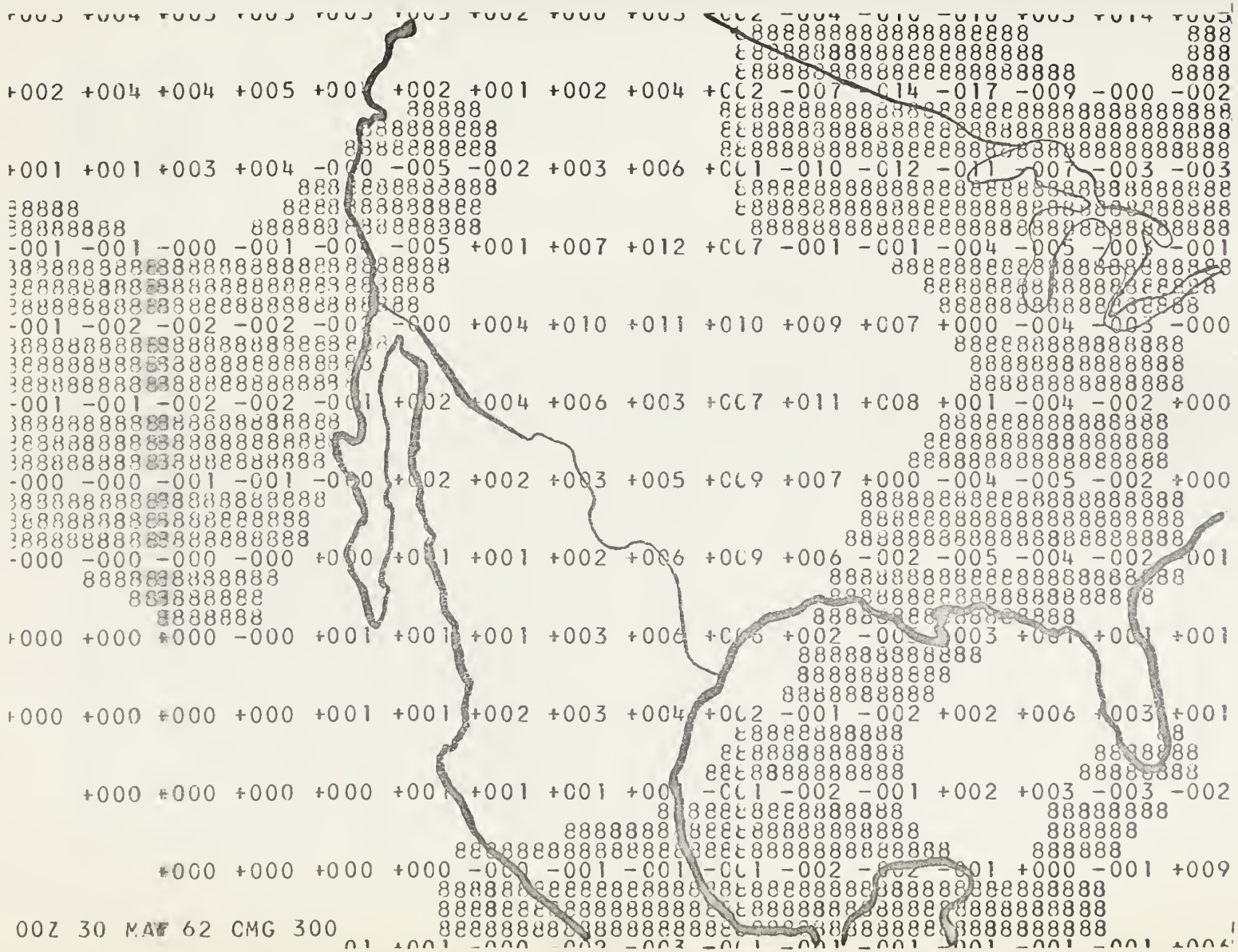
00Z 30 MAR 62 CMG 300

BIBLIOGRAPHY

1. Synoptic meteorology as practiced by the National Meteorological Center, Part II, U. S. Government Printing Office, Washington, D.C., November 1961.

2. Semi-annual progress report, Fleet Numerical Weather Facility, Monterey, Calif., April 1962.

3. Stuart, D.W., Vertical motion and the baroclinic mechanism of rapid upper level cyclogenesis, Dept. of Meteorology, University of California, Los Angeles, December 1961.

4. Wiin-Nielsen, A., On certain integral constraints for the time-integration of baroclinic models, Tellus, vol. 11, No. 1, 1959, p 45-59.

5. Gates, W.L., The stability properties and energy transformations of the two-layer model of variable static stability, Tellus, vol. 13, No. 4, 1961, p 460-471.

6. Wiin-Nielsen, A., On a graphical method for an approximate determination of the vertical velocity in the mid-troposphere, Tellus, vol. 11, No. 4, 1959, p 432-440.

7. Gates, W.L., Static stability measures in the atmosphere, Scientific Report No. 3, Dynamical Weather Prediction Project, Dept. of Meteorology, University of California, Los Angeles, October 1960.

8. Salvadori and Baron, Numerical methods in engineering, Prentice Hall, New York, 1952, p 47-49.

9. 'Arnason, G., Convergence rates of Liebmann's and Richardson's iterative methods when applied to the solution of a system of Helmholtz-type equations, Tech. Memo No. 10, Joint Numerical Weather Prediction Unit, U. S. Weather Bureau, July 1956.

10. Sawyer, J.S., The introduction of the effects of topography into methods of numerical forecasting, Quarterly Journal of the Royal Meteorological Society, vol. 85, No. 363, 1959, p 31-43.

11. Bellamy, J.C., The use of pressure altitude and altimeter corrections in meteorology, Journal of Meteorology, vol. 2, No. 1, 1945.

12. Lettau, H.H., Studies of the three-dimensional structure of the planetary boundary layer, Annual Report, Dept. of Meteorology, University of Wisconsin, August 1961, p 143-170.

13. Cressman, G.P., Improved terrain effects in barotropic forecasts, Monthly Weather Review, vol. 88, Nos. 9-12, 1960, p 327-342.

14. Berkofsky, L., and E. A. Bertoni, Topographic charts at one-degree intersections for the entire earth, GRD Research Notes No. 42, Geophysics Research Directorate, U. S. Air Force, Bedford, Mass., September 1960.

15. Ikegami-Hirofumi, A synoptic study of the January 1962 Monterey snow, M.S. thesis, U. S. Naval Postgraduate School, Monterey, Calif., 1962.

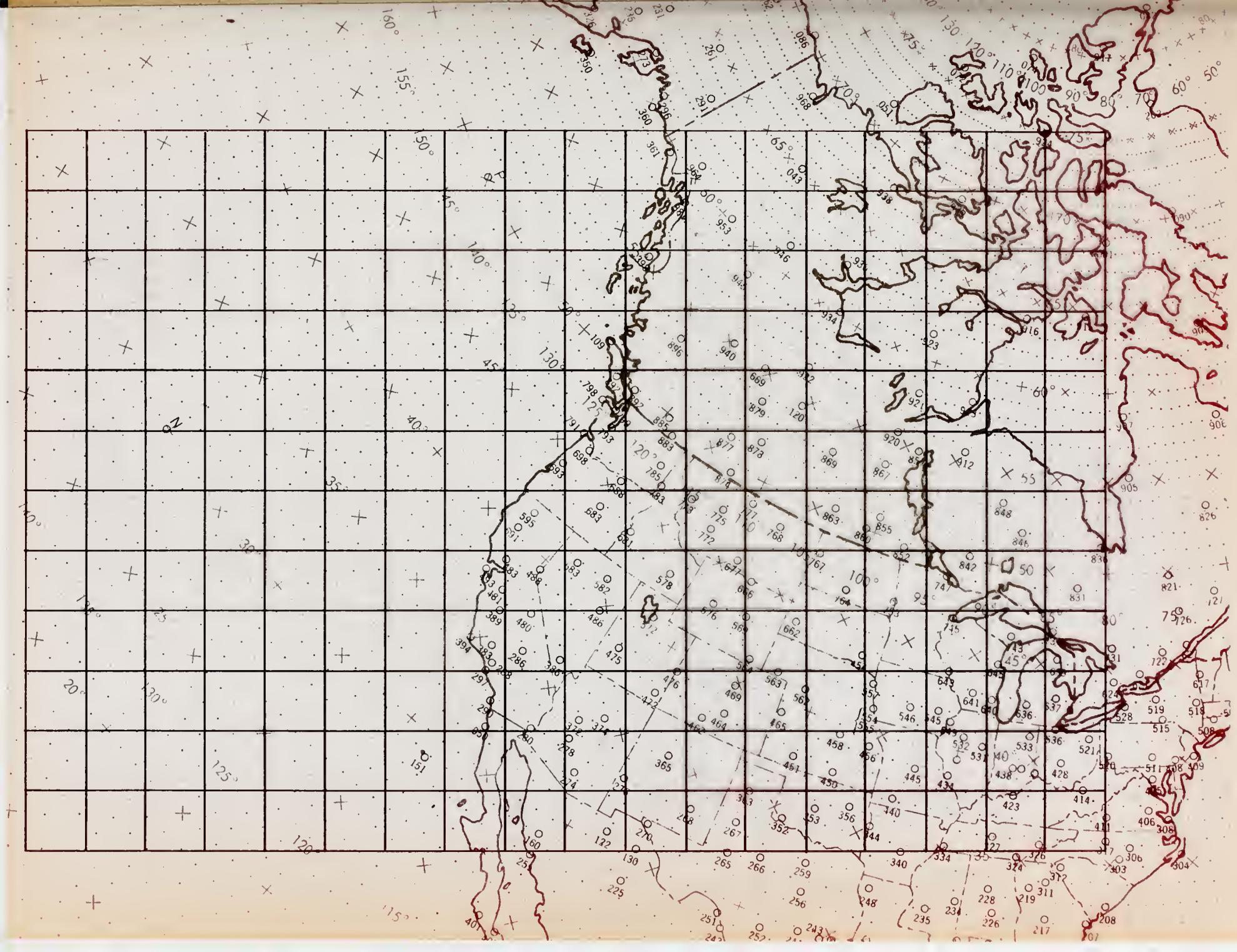

thesC496
Hemispheric solution of the Omega equati
3 2768 002 10283 2
DUDLEY KNOX LIBRARY